Charge and Spin Transport in Nanoscale Devices

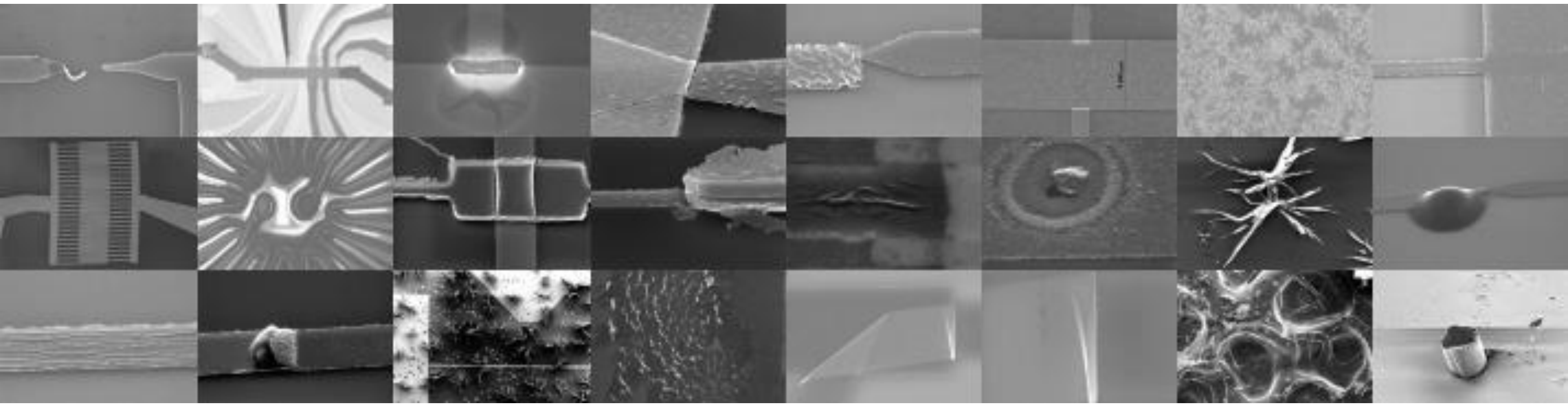

Emmanouil Masourakis
2015

eman ta zabal zazu
Universidad del País Vasco
Euskal Herriko Unibertsitatea

NAZIOARTEKO
BIKAINTASUN
CAMPUSA
CAMPUS DE
EXCELENCIA
INTERNACIONAL

CIC nanoGUNE
nanoscience cooperative research center

CIC
nanoGUNE
nanoscience cooperative research center

Thesis Supervisor: Prof. Luis E. Hueso

Resumen:

La miniaturización en el tamaño de los transistores ha sido seguida por numerosos otros componentes electrónicos y, como resultado, los dispositivos modernos consumen menos energía, la información es procesada más rápidamente y es posible almacenar la de forma más compacta. Sin embargo, la miniaturización continua de los componentes electrónicos podría estar acercándose rápidamente a un límite. En el momento en que los componentes individuales de los dispositivos se acercan a las escalas moleculares e incluso atómicas [1-5], los beneficios típicos del escalado en tamaño se pierden y conceptualmente se deberían necesitar nuevos dispositivos [6-8].

En 2011, el transistor planar tradicional fue totalmente re-diseñado con el dispositivo Intel FinFET en el nodo de 22 nm. Desde entonces, la tecnología ha avanzado al nodo de 14nm en el 2014 y la industria tiene como objetivo producir un transistor de 10 nm en 2016. En tales dimensiones, la funcionalidad del dispositivo depende fuertemente de la física mesoscópica. La creación de las generaciones futuras de dispositivos electrónicos requiere tanto de la exploración de métodos de fabricación como del diseño de estructuras capaces de superar las limitaciones actuales.

Diversas perspectivas inspiradoras se encuentran en el uso de conjuntos de moléculas como componentes de dispositivos electrónicos y en el aprovechamiento del espín de los portadores de carga para mejorar la funcionalidad [9]. En esta tesis, se explora la fabricación y el funcionamiento de dispositivos en la nano escala en un intento de arrojar luz sobre algunas cuestiones clave relativas a las próximas generaciónes de dispositivos electrónicos. En particular, nos centramos en el transporte de carga y espín en metales espacialmente confinados, en uniones túnel laterales y en conjuntos de moléculas.

El transporte de carga eléctrica en dimensiones reducidas es abordado a través de la creación y caracterización de uniones túnel laterales. Con estos dispositivos se exploran los límites de la fabricación en nuestro instituto y durante las medidas de transporte nos acercamos al límite cuántico. Al acercar las dimensiones del dispositivo al camino libre medio del electrón, el efecto túnel se hace esencialmente omnipresente. Aparte de comprender y controlar los efectos de la corriente de fuga, las uniones túnel se pueden usar en dispositivos con funcionalidades únicas (por ejemplo, diodos Esaki, uniones túnel magnéticas, transistores de electrones individuales).

Con estos mismos dispositivos podemos estudiar el transporte de carga a través de moléculas y nanopartículas conductoras, entidades que pueden dar lugar a dispositivos con funcionalidad única. Por último, prestaremos atención al transporte de espín utilizando válvulas de espín laterales (VEL). En estos dispositivos la funcionalidad extra viene dada por la introducción del espín, y la importancia de la dimensionalidad se ilustra claramente mediante la manipulación de la corriente de espín a través de la modulación de la anchura del canal de transporte.

En el Capítulo 1, se presentan los conceptos teóricos fundamentales de interés para nuestro trabajo. Empezamos explicando el impacto de las dimensiones en el

transporte electrónico e introducimos el concepto de túnel cuántico. Seguidamente, discutimos el transporte a través de grupos de moléculas y nanopartículas conductoras así como la importancia tanto del canal de transporte de cargas como de los electrodos del dispositivo. Finalmente, se presentan los conceptos básicos de la espintrónica e introducimos la válvula de espín lateral.

En el Capítulo 2 nos centramos en la nanofabricación. Comenzamos introduciendo el concepto de litografía, que es la técnica principal aplicada durante este trabajo. Con ello examinamos cada paso de la fabricación en detalle y el efecto individual de cada etapa en la resolución final del proceso. Finalmente discutimos la fabricación de uniones túnel laterales. La fabricación de estos dispositivos se realiza mediante litografía por haz de electrones (EBL), Electromigración (EM) y un método al que nos referiremos como el Método de Proyección.

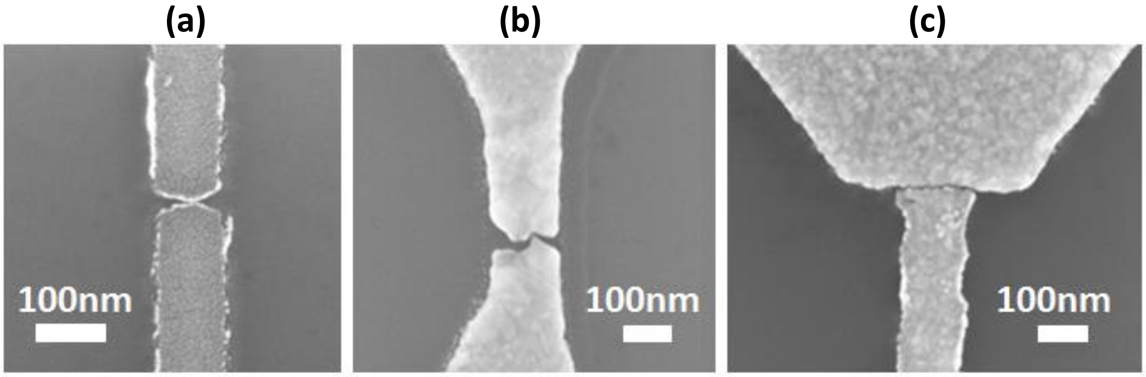

Figura 1. Uniones túnel realizadas por métodos de (a)EBL, (b)EM and (c) Proyección

Aunque para crear uniones túnel estos métodos se pueden utilizar indistintamente, la capacidad de obtener un dispositivo más pequeño depende en gran medida de los materiales utilizados y la geometría del mismo. En cualquier caso, la capacidad de controlar el tamaño de los dispositivos certeramente por debajo de 10nm sigue siendo una tarea compleja.

En el Capítulo 3, nos centramos en la caracterización eléctrica de nuestros dispositivos. Comenzamos presentando tanto la instrumentación como la configuración de medida utilizada, así como los métodos empleados para aumentar la relación señal-ruido. Pasamos a continuación a la caracterización de las uniones túnel laterales, que se realiza mediante el ajuste de nuestras mediciones de transporte al modelo de Simmons [10] que se refleja en la siguiente fórmula:

$$I(V) = A * \frac{6.17 * 10^{-6}}{s^2}\left[\left(V_b - \frac{V_{ds}}{2}\right)e^{-10s\sqrt{\left(V_b - \frac{V_{ds}}{2}\right)}} - \left(V_b + \frac{V_{ds}}{2}\right)e^{-10s\sqrt{\left(V_b + \frac{V_{ds}}{2}\right)}}\right]$$

donde A es el área de la unión túnel, s es la separación de los electrodos, V_b es la altura en energía de la barrera y V_{ds} es la tensión aplicada al canal. Los parámetros V_b y V_{ds} se expresan en voltios, mientras que A y s se expresan en nm^2 y nm respectivamente.

Con este método podemos extraer tanto la separación de los electrodos, el área de la barrera túnel y su altura en energía. Con un estudio detallado podemos resaltar la importancia de la rugosidad de los electrodos en el transporte túnel y ponemos de manifiesto que la precisión de este método es inherentemente limitada. El examen de la dependencia de la temperatura del transporte túnel nos permite a obtener parámetros con significado físico y a completar nuestro conocimiento de los dispositivos.

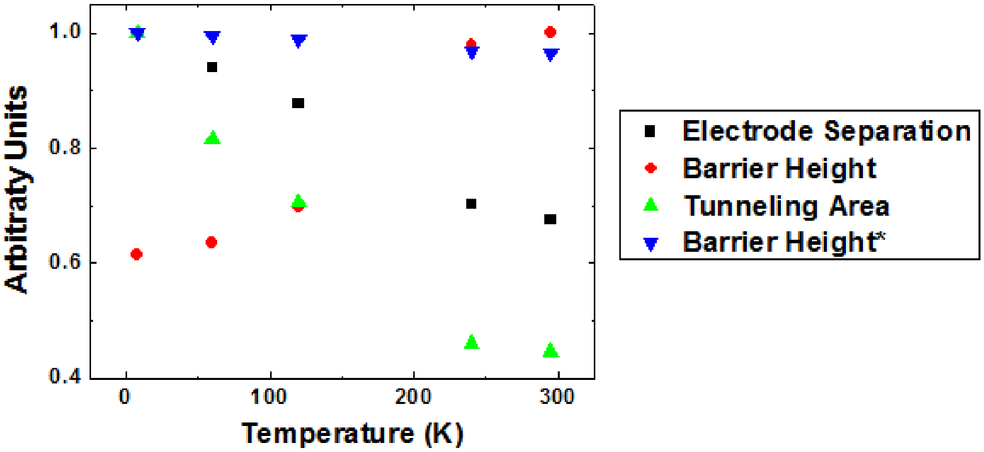

Figura 2. Parámetros obtenidos de los ajustes del transporte a través de barreras túnel y para diferentes temperaturas.

En la parte final del capítulo 3 se analiza la creación de nanopartículas conductoras residuales entre los electrodos de uniones túnel. Tales nanopartículas pueden surgir de forma natural como resultado del proceso de fabricación y se han observado usando los tres métodos de fabricación aplicados. Observamos cómo el acoplamiento de nanopartículas eléctricamente aisladas puede dar lugar a los transistores de electrones individuales.

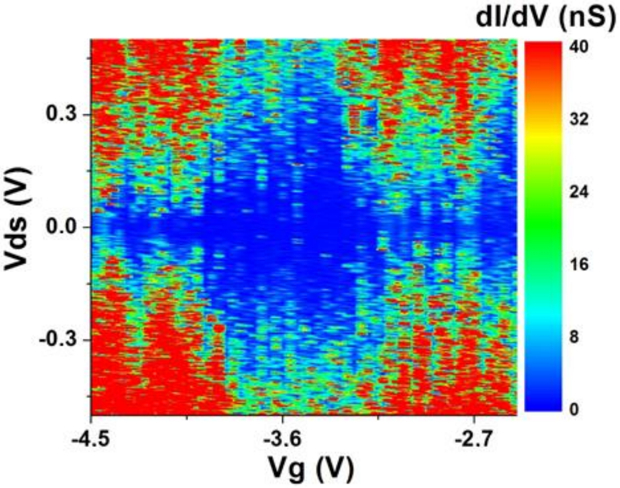

Figura 3. Diagrama de estabilidad de un transistor de un solo electrón a temperatura ambiente; creado por electromigración de un hilo de $Ni_{80}Fe_{20}$.

El uso de un electrodo de puerta nos permite identificar la presencia de tales nanopartículas y mediante la medición y el análisis de los diagramas de estabilidad obtenemos información tanto de múltiples partículas como de partículas individuales lo suficientemente pequeñas como para permitir la operación del dispositivo a temperatura ambiente.

En el Capítulo 4 se estudia la posibilidad de la creación de dispositivos mediante la sustitución de la parte aislante de la unión túnel por moléculas. La adición de las moléculas se acompaña de etapas de fabricación adicionales que son necesarias para aislar adecuadamente el canal de transporte. Estudiamos el transporte de carga a través de semiconductores moleculares como fullereno (C_{60}, C60) y pentaceno ($C_{22}H_{14}$, Pc). Estas moléculas se ensamblan en capas desordenadas y exhiben propiedades semiconductoras.

La aplicación de una tensión de puerta nos permite observar la naturaleza semiconductora de tales moléculas que se reflejan en un comportamiento de tipo-n en el caso del C60 y un comportamiento de tipo-p de Pc. Este comportamiento se mantiene incluso cuando la alineación de la función de trabajo de los electrodos ocurre con los orbitales moleculares de transporte opuestos al tipo de conducción esperado, lo que indica que los esquemas de alineación de niveles rígidos son en gran medida inexactos y sugieren dipolos interfaciales considerables. Al igual que en los trabajos de Beebee et al [11] and Worne et al [12] vemos que el transporte en este tipo de dispositivos se puede producir a través de varios mecanismos y las transiciones entre ellos se pueden obtener por variaciones de temperatura o por el voltaje aplicado.

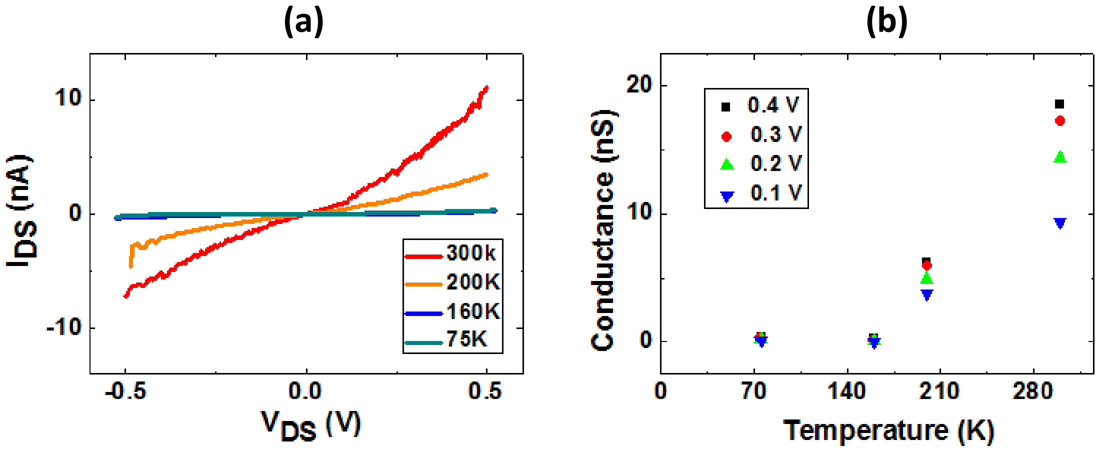

Figura 4. (a) Corriente del canal y (b) conductancia. Por debajo de 200K, el mecanismo de transporte sufre una transición de transporte asistido térmicamente a túnel independiente de la temperatura.

En la última parte del Capítulo 4 presentamos cómo los dispositivos moleculares son susceptibles a cambios parcialmente reversibles que pueden alterar sus características de transporte. Estas transformaciones pueden surgir a partir de simples mediciones de transporte eléctrico y están asociadas a cambios en la conductividad, la simetría de polaridad y la reacción del dispositivo a la tensión de puerta. Presentamos igualmente la observación inesperada de la modulación no monótona de la conductancia en un dispositivo de C60 con una gran separación entre los electrodos. Este efecto nos inspiró para medir el transporte a bajas temperaturas lo que ha revelado características que recuerdan Bloqueo de Coulomb. Para explicar esta observación se propone la hipótesis de la formación de estructuras conductoras, cuasi-unidimensionales a base de carbono dentro de la capa C60.

Finalmente, en el capítulo 5 se analiza el transporte de espín en dispositivos de válvulas de espín laterales (LSV). Estos dispositivos abordan algunas cuestiones clave en la miniaturización mediante la introducción de una funcionalidad adicional (a través del espín) y podrían llevar a disminuciones en el consumo de energía y en la disipación de calor [13]. Utilizamos dispositivos laterales de NiFe/Cu/NiFe y presentamos los efectos de la temperatura y de la distinta resistencia de espín sobre la acumulación de espín detectada. Con el uso de técnicas de electromigración podemos constreñir progresivamente el canal de transporte de espín y provocar una modulación de la señal. Ajustando nuestros resultados a un modelo de difusión de espín unidimensional confirmamos que la constricción del canal provoca un bloqueo de la difusión. La señal de espín no-local se puede expresar como [14, 15]:

$$\Delta R_{NL} = \frac{4\,\alpha_F{}^2\,\lambda_{Cu}\frac{Rcu}{L}}{\left(2+\lambda_{Cu}\,R_{Cu}\,\frac{w_{Py}\,w_{Cu}(1-\alpha_F{}^2)}{\lambda_{Py}\,L\,\rho_{Py}}\right)^2 e^{\frac{L}{\lambda_{Cu}}} - \left(\lambda_{Cu}\,R_{Cu}\,\frac{w_{Py}w_{Cu}\,(1-\alpha_F{}^2)}{\lambda_{Py}\,L\,\rho_{Py}}\right)^2 e^{-\frac{L}{\lambda_{Cu}}}}$$

donde L es la distancia de borde a borde entre los electrodos ferromagnéticos (FM) , α_F es la polarización de espín del material magnético, $R_{SN} = \lambda_N\rho_N/t_Nw_N$ y $R_{SF} = \lambda_F\rho_F/w_Nw_F(1-\alpha_F^2)$ son las resistencias de spin, t_N es el espesor del metal normal (NM), y $\lambda_{N,F}$, $w_{N,F}$ y $\rho_{N,F}$ son las longitudes de difusión de espín, las anchuras y las resistividades del NM y de los FM, respectivamente. R_{Cu} representa la resistencia a 4 puntos del canal de Cu.

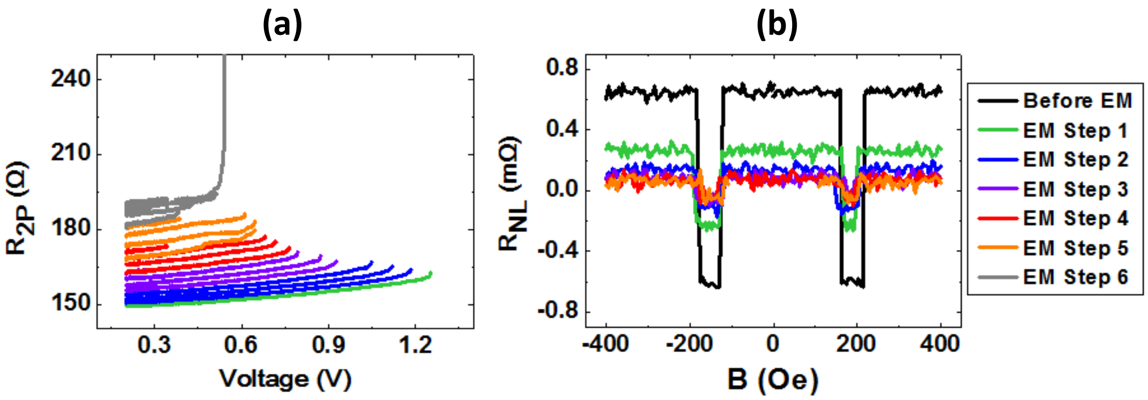

Figura 5. (a) Electromigración de una válvula de espín con un canal de Cobre en pequeños pasos. (b) Señal de espín en las varias etapas del proceso de electromigración.

Mientras que la mayoría de trabajos en válvulas de espín se han realizado usando una variedad de canales de diferentes longitudes [16-20], en el experimento que presentamos se puede modular progresivamente la resistencia del canal de cobre. De esta manera se presenta un método de caracterización por medio del cual el análisis del transporte de espín se puede llevar a cabo utilizando un único dispositivo y se puede obtener información adicional relacionada con la relajación del momento de espín. Una parametrización cuidadosa de nuestro dispositivo nos permite extraer el tamaño exacto de la constricción creada por cada paso de electromigración y a su vez, usando esta información podemos simular la acumulación de espín en nuestros dispositivos. Las simulaciones están perfectamente de acuerdo con nuestras mediciones y confirman que el constreñimiento del canal provoca un bloqueo de la difusión de espín en lugar de un aumento de los eventos de dispersión.

Table of Contents

Preface:

“With unit cost falling as the number of components per circuit rises, by 1975 economics might dictate squeezing as many as 65000 components on a single silicon chip.”

-G. Moore, 1965

Shrinking Technology:

Undoubtedly one of the greatest inventions of the last century has been that of the transistor. In 1956, this invention granted William Shockley, John Bardeen and Walter Brattain the noble prize in Physics "for their researches on semiconductors and their discovery of the transistor effect" [21]. Since then, the technology has advanced dramatically, with major milestones such as the Silicon transistor and the Integrated Circuit propelling the transistor into the forefront of technological interest.

In the 1960s, Gordon Moore produced an article which gave birth to the now-famous Moore's Law [22], whic predicted that the number of transistors per chip will roughly double every two years. By 1974, another seminal article was published by Dennard et al. describing how to scale down the physical dimensions of a MOSFET (metal-oxide-semiconductor field-effect transistor) so as to achieve simultaneous improvement in transistor density, power dissipation and switching speed [23]. Since their invention in 1947 transistors have been scaled down from bulky hand-filling chunks of metal and semiconductor to precisely defined nanoscale components (as predicted by Moore).

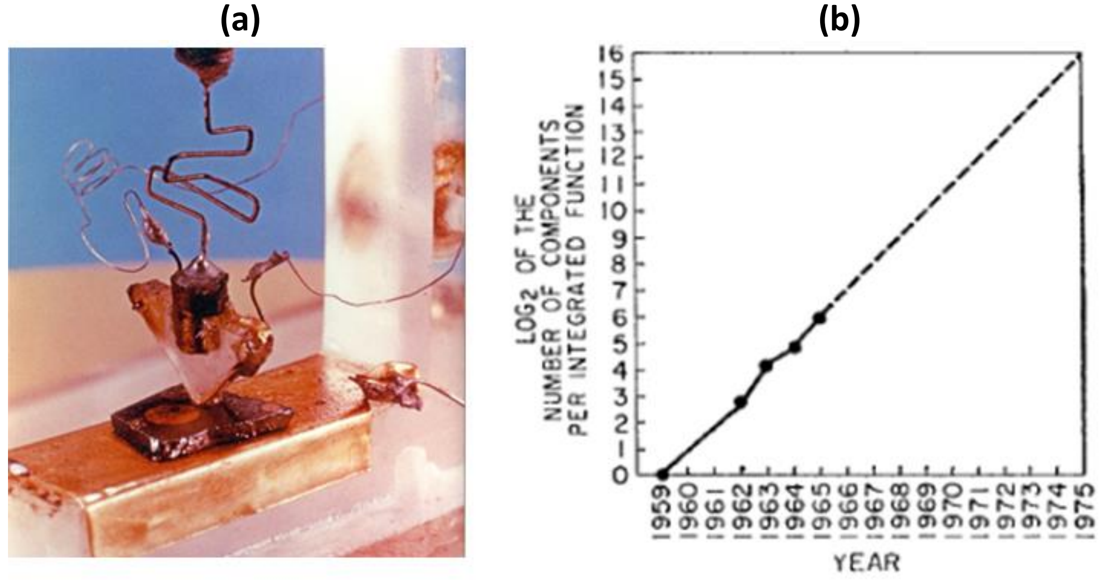

Figure 1. (a) Bardeen and Brattain's first point-contact transistor from 1947 [24]*. (b) Plot from Gordon Moore's paper* [22] *indicating his prediction for the increase in number of electronic components per silicon chip.*

The shrinking of transistors has been followed by numerous electronic components and, as a result, modern devices consume less energy, process information faster and store information more compactly. However, the continuous shrinking of technology is quickly approaching a limit. As individual components of devices approach the molecular and even atomic scales [1-5], the typical scaling benefits are lost and conceptually new devices are needed [6-8].

In 2011, the traditional planar transistor was re-designed and Intel released the 22nm node FinFET transistor (see Fig.2). Since then, the technology has advanced to the 14nm node transistor in 2014 and the industry aims to reach the 10nm node by 2016.

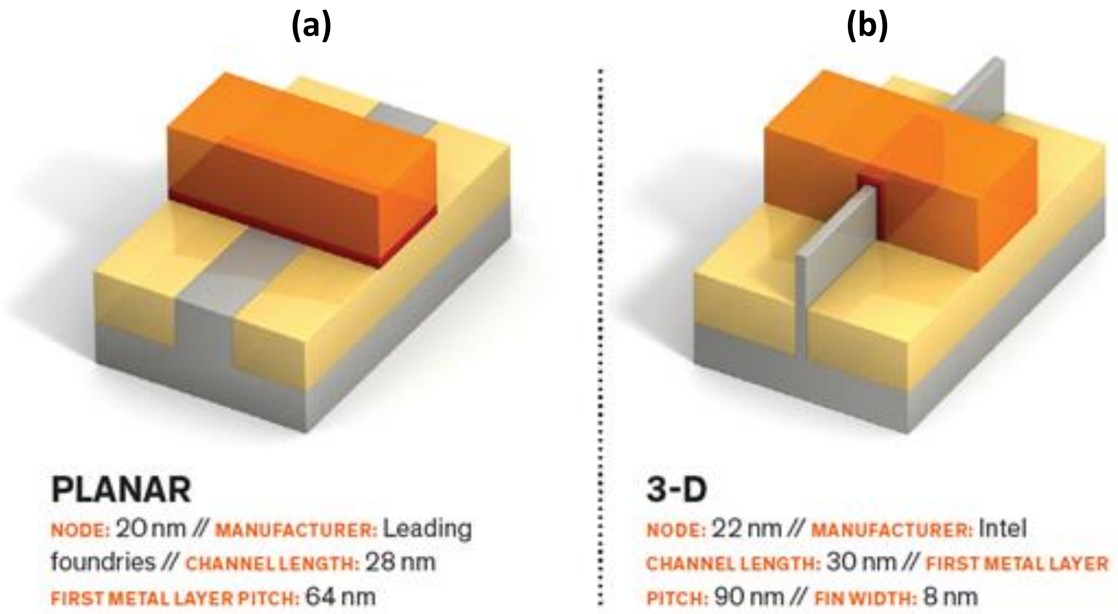

Figure 2. Manufacturers moved from the (a) planar transistor geometry to the (b) 3D transistors. Image taken from [25].

At such dimensions, the functionality of devices strongly depends on mesoscopic physics and in order to be sustained traditional devices must be re-designed. The creation of next-generation devices, requires the exploration of fabrication methods and device structures which can accommodate the new specifications and overcome the current limitations. To this end, inspiring prospects are found in using assemblies of molecules as device components and harnessing the spin of carriers to enhance functionality [9]. In this thesis, we explore the fabrication and operation of lateral nanoscale devices in an attempt to shed light onto some key issues of charge and spin transport required for the next generation of devices.

Thesis Summary:

Charge and spin transport are studied in spatially confined metals, lateral tunnel junctions and assemblies of molecules. Charge transport in reduced dimensions is approached by creating and characterizing lateral tunnel junctions. While making the devices, we explore the limits of fabrication and while measuring them we look at electron transport by quantum tunneling. As device dimensions approach those of the electron mean free path, tunneling has become essentially omnipresent and increasingly important. Aside from understanding and controlling the effects of unwanted leakage current, tunneling can be used as the principal transport mechanism of a device and add unique functionality (eg. Esaki diodes, magnetic tunnel junctions, single electron transistors).

In chapter 2, we first present an overview of nanofabrication and then focus on the fabrication of lateral tunnel junctions. This was approached using Electron Beam Lithography (EBL), Electromigration (EM) and a method we refer to as the Overhang Method. Although these methods are fundamentally different, we find that for each method, the smallest device features that can be achieved are largely dependent on the materials used and the device geometry.

In chapter 3, we focus on the characterization of devices. Characterization of lateral tunnel junctions is done by fitting the transport measurements to the Simmons model. In this way, we can extract the electrode separation, the tunneling area and the height of the energetic barrier. By examining the temperature dependence of tunneling transport, we point out that its accuracy is inherently limited and that the parametrization applied can change our understanding of the junctions' behavior. Further into this chapter, we examine the trapping of residue conductive nanoparticles between the electrodes of tunnel junctions. We see that, the coupling of electrically isolated nanoparticles, can give rise to single electron transistors (SETs). By measuring and analyzing stability diagrams, we observe the trapping of single particles, multiple particles and particles which are small enough to allow for room temperature operation.

In chapter 4, we look at the possibility of creating devices by replacing the insulating part of the tunnel junction with molecules. Given the attractive electrical properties of carbon-based moleules we study charge transport through the molecular semiconductors C60 fullerene (C_{60}, C60) and Pentacene ($C_{22}H_{14}$, Pc). Similar to the works of Beebee et al [11] and Worne et al [12], we see that the transport in such devices can occur via several mechanisms and transitions between these mechanisms can be brought on by varying the device temperature and the bias applied to the channel. Furthermore, we see that such devices are susceptible to partially reversible changes in their transport characteristics. These changes are presented using a C60 device, which after multiple measurements exhibits behavior reminiscent of Coulomb Blockade.

Finally in chapter 5, we examine spin transport in metallic lateral spin valve (LSV) devices. LSVs allow the use of the spin degree of freedom to process information and alleviate electronics from the heat dissipation and power consumption associated with charge transport [13]. Hence spintronic devices address some key issues of miniaturization. Using EM, we are able to progressively constrict the spin transport channel and cause a modulation of the non-local signal. By fitting our results to the one-dimensional spin diffusion model, we analyze the spin transport properties of our devices. Simulations of spin accumulation confirm that the constriction of the channel causes a blocking of spin diffusion rather than an increase of scattering events.

Chapter 1:

Theoretical Background

1.1 Introduction:

As we venture into the nanoscale, devices can no longer be viewed in a classical way as quantum effects come into play. Such effects start bearing significance when we approach the regime of mesoscopic physics. To look at nanoscale devices, we must hence consider the physical effects which arise in this regime. In this chapter we introduce the necessary theoretical background relevant to the devices made and measured during this work. Here we give a basic review of the theory involved, which in following chapters is supplemented when necessary.

Macroscopic Regime		Mesoscopic Regime	
$L >> l_e$	Diffusive Transport	**$L \leq l_e$**	Ballistic Transport
$L >> \lambda_F$	No Size Quantization	**$L \leq \lambda_F$**	Size Quantization
$L >> \lambda_s$	No Spin Memory	**$L \leq \lambda_s$**	Spin Memory

Table 1. Some limits of the macroscopic regime and their resulting effects. l_e is the mean free path, λ_F is the de Broglie wavelength of electrons at the Fermi level and λ_s is the spin diffusion length

The chapter will start by exploring the dependence of conductivity on dimensionality. Going into quantum mechanical tunneling will then allow the understanding of the principal transport mechanism in the metal-insulator-metal (M/I/M) tunnel junctions presented in chapter 3. Quantum tunneling and quantum confinement effects, as well as the Coulomb Blockage effect will allow the discussion of single electron transistors. For chapter 4, we discuss the transport of delocalized charge carriers in disordered assemblies of molecules. Finally, in the last part of this chapter, we will review the basics of spin transport, which will be needed to discuss the lateral spin valves of chapter 5.

1.2 Density of States:

The density of states (DOS) gives the number of allowed electron (or hole) states per volume at a given energy. The allowed states are determined by the Schrödinger equation whose solution determines that particles can assume discrete energy values of E_n. These energies are given by:

$$E_n = \frac{n^2\hbar^2\pi^2}{2ma^2} = \frac{k^2\hbar^2}{2m}, k = \frac{n\pi}{a} \quad (1)$$

where n is the level number (n=1, 2, 3…), ħ (=h/2π) is the reduced Plank's constant, m is the electron mass and a is the dimension of the material (eg. length). In Equation 1, the dimensionality of the system is reflected by k which is comprised of individual k_i

components corresponding to each dimension of the system. In bulk material, where there are three dimensions, k is expressed as:

$$\mathrm{k} = \mathrm{k}_x^2 + \mathrm{k}_y^2 + \mathrm{k}_z^2 = \left(\frac{n_x \pi}{a}\right)^2 + \left(\frac{n_y \pi}{a}\right)^2 + \left(\frac{n_z \pi}{a}\right)^2 \tag{2}$$

Removing one dimension from the system requires the corresponding k_i component to be set to zero changing the solutions to Equation 1. Consequently, the states available will depend on the dimensionality of the material.

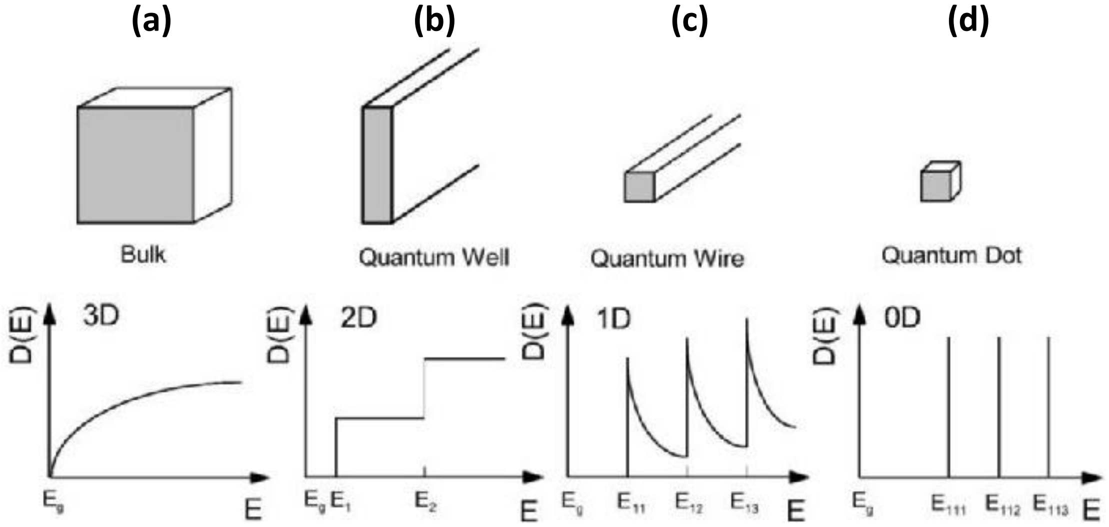

Figure 1. Schematic diagram illustrating the representation of the electronic density of states depending on dimensionality [7].

The DOS, N(E), is the number of states available in a given energy interval and in a given space. Hence if we define an energy density g(E) = dn/dE, the density of states N(E) can be calculated as:

$$N(E)_{0D} = \delta E \tag{3}$$

$$N(E)_{1D} = \frac{g(E)_{1D}}{a_x} = \frac{1}{\pi}\sqrt{\frac{2m}{E\hbar^2}} \tag{4}$$

$$N(E)_{2D} = \frac{g(E)_{2D}}{a_x a_y} = \frac{m}{\pi\hbar^2} \tag{5}$$

$$N(E)_{3D} = \frac{g(E)_{3D}}{a_x a_y a_z} = \frac{1}{2\pi^2}\left(\frac{2m}{\hbar^2}\right)^{3/2}\sqrt{E} \tag{6}$$

The units of N(E) are number of states per unit energy per unit space (either volume, area, or length). Note how for 2D there is no dependence on energy and how for 0D the concept of energy density no longer holds and the density of states takes the form of a series of delta functions. To account for spin degeneracy the above expressions are often found multiplied by a factor of 2. The DOS functions are illustrated in Fig. 1.

The concept of DOS is used in a multitude of calculations, from simple electron occupancy to ballistic transport (see section 1.3). The number of electrons occupying a material, is given simply by the product of the DOS, and the state occupancy probability (for electrons the Fermi-Dirac distribution). As we will see, this fundamental concept of solid state physics is crucial to understanding charge transport in nanoscale devices.

1.3 Transport in Reduced Dimensions:

In the macroscopic world, charge transport occurs in a diffusive manner. As charge carriers drift through a conductor, they undergo a series of collisions referred to as scattering events. Each of these collisions can change the direction of the travelling carriers and influence how quickly carriers will transverse the material. The average distance travelled between scattering events is called the mean free path (l_e), which is featured in Table 1 and is a crucial parameter of carrier transport. While several types of carrier scattering exist (impurities, grain boundaries, sidewalls, other carriers), the most significant scattering events are those related to defects and impurities in the conductor.

As we decrease the dimensions of a conductor, the relevant scattering mechanisms start to change which in turn affects the conductivity. The size dependence of conductivity has been investigated for over a century [26] and has been studied extensively [27-33]. As we progressively decrease the device dimensions, the description of conduction as a diffusive process starts to falter. When the dimensions become comparable to the mean free path, the number of scattering events decreases and charge carriers transverse the medium while scattering only against the conductor's walls.

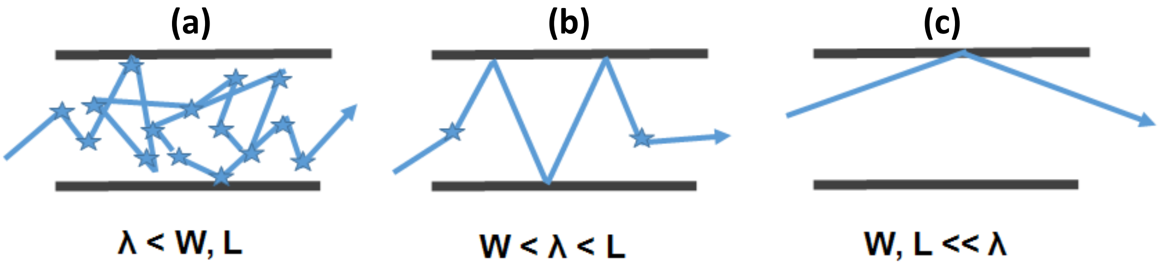

Figure 2. Entering the Ballistic Regime. (a) Diffusive transport (b) Quasi-ballistic transport (c) Ballistic Transport

As this happens, we move from the diffusive (Fig. 2(a)) into the quasi-ballistic (Fig. 2(b)) and finally the ballistic (Fig. 2(c)) regimes of charge transport. At this limit the resistance of the conductor becomes independent of its length and the well-known Ohm's Law becomes obsolete. As scattering decreases, the concept of conductivity, $\sigma = j/E = nq^2\tau/m$ (j is current density, E is applied electric field, n is number of free electrons, q is electron charge, τ is time between scattering events and m is electron mass) becomes irrelevant. However as current still flows through the system we can instead talk about the system's conductance (G = I / V). Although the collapse of Ohm's Law negates the relationship G = σW/L, the conductance will always be defined as the ratio of the current over the voltage.

$$G \equiv \frac{I}{V} \neq \sigma \frac{W}{L} \tag{7}$$

Conductance of ballistic systems can be derived for a quantum wire, i.e. a one-dimensional (1D) conductor, adiabatically (without heat loss) connected to two charge reservoirs. The 1D nature of the material gives rise to a density of states of:

$$g_{1D}(E) = \frac{2}{h}\sqrt{\frac{2m}{E}} = \frac{2}{hv(E)} \tag{8}$$

where $g_{1D}(E)$ is the density of states, E is energy, h is Plank's constant, m is the electron mass and v(E) is the electron velocity. The factor of 2, is introduced to account for spin degeneracy. Then, if an electrochemical potential difference arises between the two reservoirs, (μ_2-μ_1) it will give rise to a current I, which can be expressed as:

$$I = \int_{\mu 1}^{\mu 2} qv\,(E) g_{1D} dE \tag{9}$$

Substituting Equation (8) into Equation (9) we obtain:

$$I = \int_{\mu 1}^{\mu 2} qv\,(E)\frac{2}{hv(E)} dE = \frac{2q}{h}\int_{\mu 1}^{\mu 2} dE = \frac{2q}{h}\,(\mu_2 - \mu_1) \tag{10}$$

Replacing (μ_2-μ_1) with qV, where V is the potential difference across the channel, we get:

$$I = \frac{2q}{h}\,(qV) \tag{11}$$

Now, we can easily derive the conductance (G) of the channel by dividing both sides by V to obtain:

$$G = \frac{I}{V} = \frac{2q^2}{h} \tag{12}$$

The above value represents the conductance of a single ballistically conducting channel and is called the quantum of conductance, G_0 = 77.5µS. Note that it is made up of fundamental constants and is independent of material properties.

Quantized conductance in ballistic conductors was first observed experimentally in 1988 [34]. In this experiment, a point contact was defined in a two-dimensional electron gas (2DEG) and its width was varied smoothly by applying a gate voltage. The experiment was carried out at low temperature where atomic vibrations and the probability of scattering are reduced. As the width of the point contact increased, it was observed that the conductance did not increase smoothly, but instead in steps of G_0. The resulting measurements indicate a size-dependent conductance showing a step like increase with steps of G_0. A slightly modified version [35] of the original measurement is seen in Fig. 3.

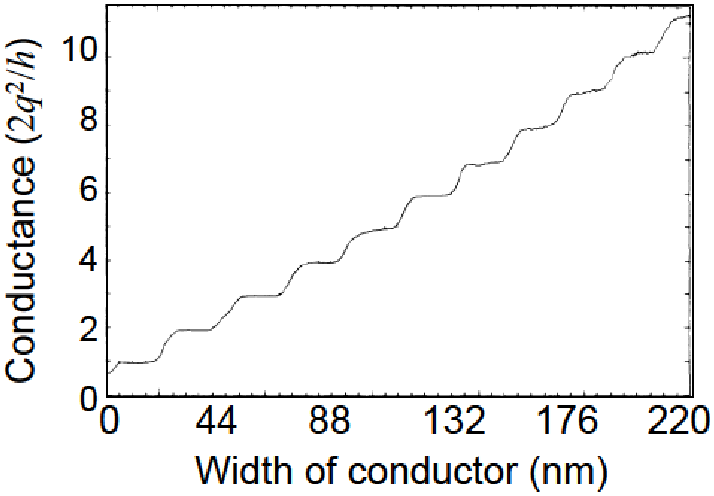

Figure 3. Experimental observation of the quantum of conductance as observed by [34]. Image taken from [35]

.

As we increase the width of a wire carrying a single conductance channel, we see that it behaves as if more conduction channels are gradually added to it one by one. In fact, this is exactly what happens and in the absence of scattering, the conductance of a wire including N parallel conduction channels can be expressed as $G = NG_0$.

The theory can also be extended for the quasi-ballistic case by incorporating a scattering site into our perfect 1D conductor. The scattering site, introduces a transmission probability into the single channel conduction which results in the well-known Landauer formula [36-38]:

$$G = \frac{2q^2}{h} NT = \sum_{n=1}^{N} \frac{2q^2}{h} T_n \tag{13}$$

Here N is the number of conducting channels and T_n is the transmission coefficient of each conduction channel. Fully scatter-less channels are called open channels and are represented by T = 1. Similarly channels which are unavailable for transport are called closed channels and are represented by T = 0. T will always be between 0 and 1. If the transmission coefficient of all channels are equal, Equation 12 can simply be written as $G = G_0NT$. Note that, Equation 11 which was derived above is simply an instance of the Landauer formula in which we have a single conduction channel N = 1, and the conduction is purely ballistic, i.e. T = 1.

Hence, here we have described the conduction of charge carriers in low dimensionality, where the density of states and the scattering processes are different to those of bulk. If we keep decreasing the width of the conductor we will eventually cause the wire to disappear leaving us with the two charge reservoirs separated by a gap. The gap, will have no density of states and will be an insulating layer which creates a potential barrier between the reservoirs, blocking carrier transport. As we see in the next section, even in this case, charge carriers have means of crossing the insulating barrier. By making use of their wave-like nature, carriers can not only go over the barrier but even directly through it. This process is referred to as quantum mechanical tunneling and is explained in the following section.

1.4 Quantum Tunneling:

The tunnel effect explains how a charge carrier can move through an insulating medium; or in general, a potential barrier. The effect was observed over a century ago and since then has largely expanded our understanding of the physical world [39]. Given that quantum tunneling is the conduction mechanism of the M/I/M devices of chapter 3, this section is dedicated to introducing the effect as is relevant for M/I/M tunnel junctions.

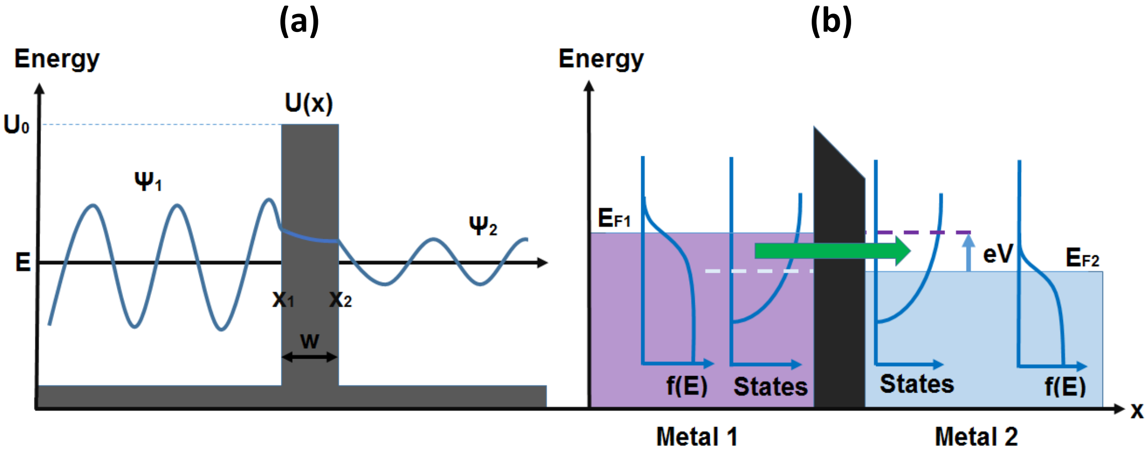

Figure 4. (a) Electron wavefunction decays through a potential barrier and comes out on the other side. (b) Electrodes separated by and insulating barrier.

As the name suggests, quantum tunneling is a quantum mechanical effect and in fact, is forbidden in classical physics. In classical physics when a moving particle encounters a potential step is will be completely reflected. In quantum mechanics the wave-like nature of particles allows a different treatment. When an electron wave is faced with a potential barrier, most of it will be reflected but a small portion of it will penetrate the barrier. Within the barrier, the wave function will decay rapidly (exponentially [39]), but if the barrier is thin enough, the electron wave might be able to appear on the other side of it. Hence, the probability of an electron penetrating the potential barrier and appearing on the other side of it, i.e. tunneling through the barrier, is non-zero.

When a voltage is applied across the junction, an electrochemical potential difference of qV will arise between the electrodes (Metal 1 and Metal 2). The number of electrons tunneling from one side of the barrier to the other will then be the number of conduction electrons with increased energy ($g_1(E)f_1(E)$) (on one side) times the number of free available states on the other side ($g_2(E)(1-f_2(E))$), times the tunneling probability P. The tunneling current from Metal 1 to Metal 2 can be written as:

$$I_{1\to2} = \int_{-\infty}^{\infty} P\, g_1(\mathrm{E})\, \mathrm{f}_1(\mathrm{E})\, g_2(\mathrm{E})\big(1-\mathrm{f}_2(\mathrm{E})\big)\, dE \qquad (14)$$

The total current flowing through a tunnel junction will be the difference between the currents flowing in each direction $I_{tot} = I_{1\to2} - I_{2\to1}$. The tunneling probability P, is given by the squared wavefunction after the barrier divided by the squared wavefunction before the barrier ($P=|\psi_2|^2/|\psi_1|^2$). Hence, to determine the tunneling probability we must solve the Schrödinger equation:

$$-\frac{\hbar}{2m}\frac{d^2\psi(x)}{dx^2} + U(x)\psi(x) = E\psi(\chi) \qquad (15)$$

where ψ is the electron wavefunction, m is the electron mass, ħ is the reduced Plank's constant, E is the electron energy and U(x) is the height of the potential barrier. For an abrupt rectangular barrier, the wavefunctions take the form of $\psi(x) = A(x)e^{\pm ikx}$ (where A is the amplitude of the wavefunction, $i=\sqrt{-1}$ and $k=\sqrt{2m(E-U_0)/\hbar}$).

Unsurprisingly, in real devices, barriers tend to have more complicated shapes and additional treatment is required. For more complicated barrier shapes we apply the WKB (Wentzel-Kramers-Brillouin) approximation. To do so, we must assume that the potential varies very slowly, on a scale comparable to the electron (de Broglie) wavelength λ_e. In this way, the solution of Equation 15 gives wavefunctions of the form $\psi(x) = e^{\pm i\int k(x)dx}$. Using these wavefunctions the tunneling probability can be found to be:

$$P = \frac{|\psi_2|^2}{|\psi_1|^2} = e^{-2\int_{x_1}^{x_2}\sqrt{\frac{2m(E-U_0)}{\hbar}}\,dx} \qquad (16)$$

The most commonly used equation for tunneling current is the one derived by Simmons [10]. Using Equation 14 and Equation 16 and applying step-wise Fermi distributions (T=0K), Simmons derived an expression for the total tunneling current through an arbitrarily shaped barrier of potential $\bar{\varphi}$.

$$J = \frac{J_0}{d^2}\left(\bar{\varphi} - \frac{qV}{2}\right)e^{-Ad\sqrt{\bar{\varphi}-\frac{qV}{2}}} - \frac{J_0}{d^2}\left(\bar{\varphi} + \frac{qV}{2}\right)e^{-Ad\sqrt{\bar{\varphi}+\frac{qV}{2}}} \qquad (17)$$

where $J_0 = \frac{q}{2\pi h}$, d is the electrode separation, $\bar{\varphi}$ is the average barrier height, V is the applied voltage and $A = 4\pi\frac{\sqrt{2m}}{h}$.

The Simmons model, is often used to fit measurements of current as a function of applied voltage (I-V measurements) in M/I/M tunnel junctions. From such fittings one can extract the values of the electrode separation, average barrier height and tunneling area (I=JA).

For low applied voltages (qV$<\bar{\varphi}$), the exponential term of Equation 17, remains relatively constant and hence the dependence of the tunneling current on the applied voltage appears linear. At larger applied biases (qV $>\bar{\varphi}$) the relationship quickly becomes non-linear. Finally, when the applied voltage is much larger than the barrier height (qV $\gg \bar{\varphi}$), the barrier shape is distorted so much that it effectively becomes triangular and the carriers tunnel through only a partial width of the barrier [40, 10]. Here, we find ourselves in the field emission or Fowler-Nordheim (FN) regime, where the theoretical treatment is slightly altered and although the mechanism is still tunneling, the effective barrier width is reduced as carriers tunnel through only part of the barrier [41, 42, 11].

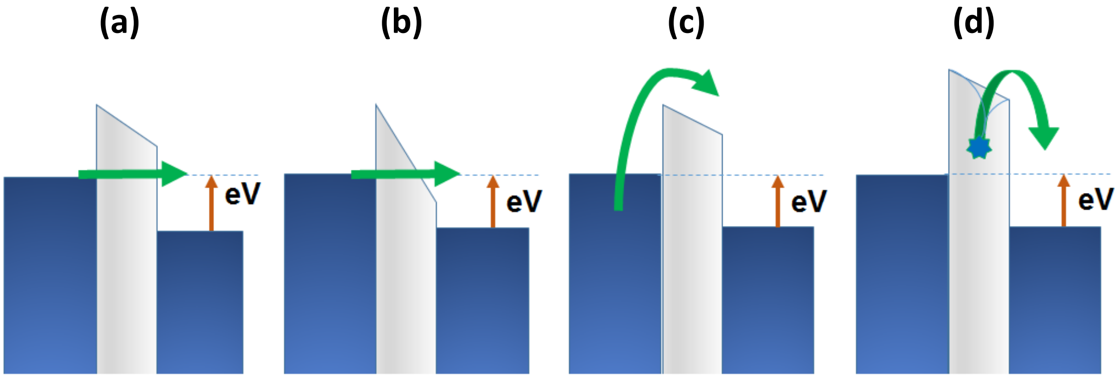

Figure 5. (a)Direct Tunneling (b)Field Emission or FN tunneling (c)Thermionic Emission (d) Poole-Frenkel emission. Image adapted from [40].

In addition to directly going through the barrier, carriers can also cross the barrier in other ways. Contrary to tunneling, these mechanisms have a notable temperature dependence of the current. One instance of this is when carriers acquire sufficient energy to pass over the barrier. This mechanism is often found in heated devices and is known as Thermionic Emission. Another way for carriers to cross the barrier is with the assistance of defects within the insulating layer. Such defects are known as charge traps and are essentially localized potential wells capable of retaining carriers within them. Charge traps provide available energy states within the barrier which can significantly distort the barrier and can also be used by electrons to move through the insulator in a step-like fashion. Examples of trap-assisted transport are the Poole-Frenkel (PF) emission and variable range hopping.

In table 2, we present a comparison of various methods used by carriers to transverse potential barriers.

Mechanism	Characteristic Behavior	Temperature Dependence	Voltage Dependence
Direct Tunneling	$\mathrm{J} \propto Ve^{\left(-\frac{2d}{h}\sqrt{2mq\varphi}\right)}$	none	$\mathrm{J} \propto V$
Field Emission	$\mathrm{J} \propto V^2e^{\left(-\frac{4d\sqrt{2m}}{3hqV}(q\varphi)^{3/2}\right)}$	none	$\ln\left(\frac{J}{V^2}\right) \propto \frac{1}{V}$
Thermionic Emission	$\mathrm{J} \propto T^2e^{\left(-\frac{q\varphi-q\sqrt{qV/4\pi\varepsilon d}}{kT}\right)}$	$\ln\left(\frac{J}{T^2}\right) \propto \frac{1}{T}$	$\ln(J) \propto V^{1/2}$
Poole-Frenkel	$\mathrm{J} \propto Ve^{\left(-\frac{q\varphi-q\sqrt{qV/\pi\varepsilon d}}{kT}\right)}$	$\ln\left(\frac{J}{V}\right) \propto \frac{1}{T}$	$\ln\left(\frac{J}{V}\right) \propto V^{1/2}$
Hopping	$\mathrm{J} \propto Ve^{\left(-\frac{q\varphi}{\kappa T}\right)}$	$\ln\left(\frac{J}{V}\right) \propto \frac{1}{T}$	$\mathrm{J} \propto V$

Table 2. Distinct transport mechanisms for conduction through an MIM system. Adapted from [40, 43]

1.5 Transport Through Molecules:

In the late 1980s, the invention of the organic light-emitting diode (OLED) by Tang and Van Slyke proliferated the semiconductor industry's interest in organic semiconductor materials [44, 45]. For many years, the advantageous properties of molecular assemblies where overlooked due to the difficulty of creating sufficient quantities of material with high purity and structural integrity. As technology progressed, molecular assemblies have made their way into promising fields of research such as the organic field effect transistors (OFET) [46] and organic photovoltaics (OPV). The most notable advantages of molecular devices are their flexibility and their optical properties although potential has been demonstrated in other areas such as organic spintronics.

In chapter 4, we look at charge transport through molecular devices. These devices possess the geometry of lateral transistors and use either assemblies of Fullerene (C_{60}) or the Pentacene ($C_{22}H_{14}$) molecules as the carrier transport channel. In this section we present the basic theory of molecular electronics as is relevant for chapter 4.

Like most materials, the properties of molecular assemblies depend on how their constituent elements combine to make up the material. Carbon-based molecules have attracted considerable attention due to the covalent bonding between carbon atoms. The binding of carbon atoms takes place via the hybridization of their p and s orbitals, which gives rise to π and σ molecular orbitals respectively.

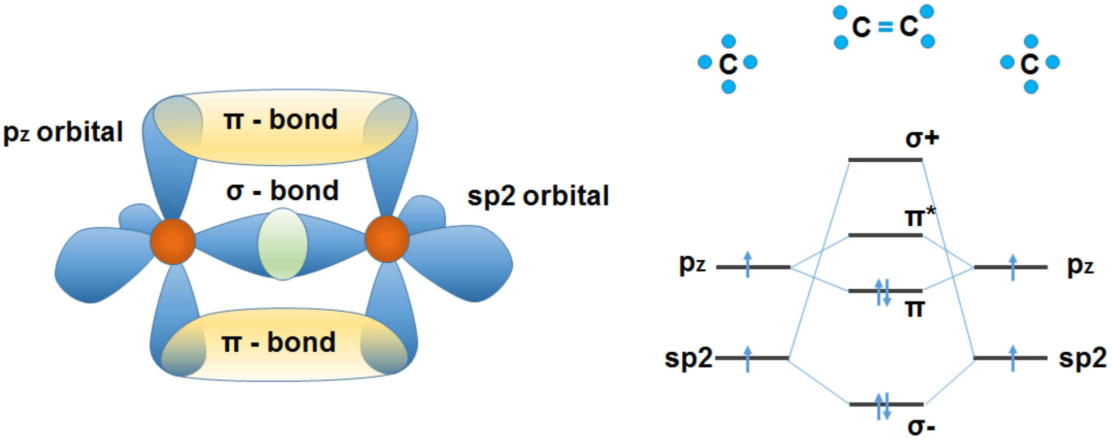

Figure 6. Carbon-Carbon bond showing orbital hybridization and formation of π and σ bonds. Adapted from [47] and [48].

The hybridization of atomic orbitals defines both the mechanical and electrical properties of molecules and determines how they assemble into bulk materials. While, the strong σ bonds contribute to mechanical stability, the π orbitals form a cloud of loosely bound (delocalized) electrons between the two atoms. The delocalization of carriers is an exceptional characteristic which has direct implications for the optical properties and charge carrier transport.

The consequences of conjugated carbon bonding are also seen in the assembly of carbon-based molecules into bulk materials. Given that the electrons are engaged in covalent bonds, the binding of individual molecules to one another will be implemented only via weak van der Waals forces. This weak intermolecular interaction results in molecules assembling in a highly disordered fashion and bulk materials being either polycrystalline or completely amorphous. Furthermore this bonding is responsible for some mechanical and thermodynamic properties of the bulk material such as the reduced hardness and low melting points [49]. Although such properties can be useful for given applications, the creation of highly order large scale molecular crystals is an important goal of organic electronics as it would allow for unprecedented charge transport properties.

The energy landscape of these weakly bound materials, consists of a collection of localized states, which broaden the resulting energy bands. Instead of sharp well defined band edges, exponential tails of localized states extend into the band gap [50] (see Fig. 7). Since the notion of a *band* of energy is not always appropriate, a different terminology is used for molecular assemblies. The energy levels equivalent to the conduction and valence bands are referred to as the Highest Occupied Molecular Orbital (HOMO) and the Lowest Unoccupied Molecular Level (LUMO). Similarly, the energy difference equivalent to the bandgap is referred to as the HOMO-LUMO Gap (HMG).

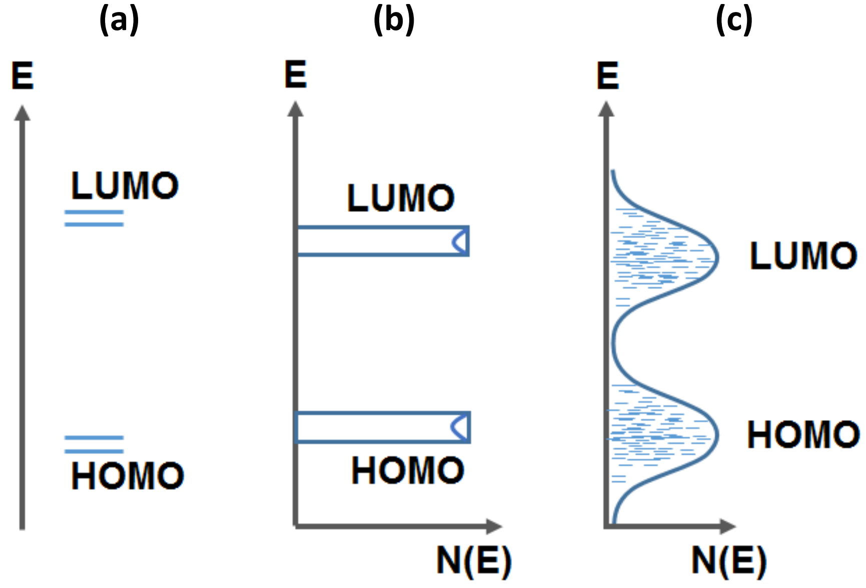

Figure 7. Energy Band diagram for π-conjugated (a) single molecule (b) ideal molecular crystal (c) realistic, disordered assembly of molecules. Adapted from [50].

Molecular assemblies usually behave either as insulators or as large-bandgap semiconductors [51]. The inherently large disorder, gives rise to a complicated conduction process in which principally delocalized carriers combine tunneling, hopping, thermionic emission and even band conduction to transverse a series of localized states connected through potential barriers [50]. Band conduction becomes more probable as the order of the molecular assembly is increased and can usually be expected in more conductive systems. For large disorder, the transport is dominated by intermolecular hopping [52] and the conductance is expected to be lower [48]. Tunneling should be limited to short organic interlayers, although multi-step tunneling, which allows for tunneling to dominate transport in large channels (>10nm) has also been proposed [53].

To further complicate matters, the addition or extraction of a charge to a molecule will cause a considerable structural deformation of the surrounding atomic and electronic environment [51] resulting in the bond lengths of neighboring atoms and the overall energy landscape to change. Consequently, charge transport in molecular assemblies is not carried out by electrons and holes but by their quasiparticle counterparts known polarons. Electron polarons and hole polarons consist of the respective charges and their associated lattice distortions [48, 51]. For simplicity, this fact is typically ignored and the carriers are considered to simply be electrons and holes [51].

As previously mentioned, the molecular devices studied during this thesis, make use of either Fullerence (C60) or Pentacene (Pc) molecules. When assembled, these molecules exhibit semiconducting characteristics and just like their inorganic counterparts they can become either n-type (electrons dominate conduction) or p-type (holes dominate conduction). Unfortunately, the standard method of ion implantation used for Silicon (Si) and Gallium Arsenide (GaAs) cannot be applied to molecular assemblies, as the ion beam process results in excessive concomitant damage to neighboring molecules. Molecular assemblies can experience unintentional doping during the synthesis and handling of the materials, so accurate tuning of the materials transport properties is a challenging task [49, 54]. Even a brief exposure to air can cause sufficient doping and radically change the material properties [55-57].

Controlled doping of molecular assemblies has been an important milestone in the field of organic electronics and has been the subject of a significant amount of work [49, 58, 59, 60, 55]. On one hand this work addresses the recovery of unintentionally doped materials and the other hand the work focuses on the development of novel doping techniques which are compatible with molecular assemblies. On both fronts significant advancements have been made. Techniques such as thermal annealing have been shown to enhance either n-type or p-type transport, and improve the stability of devices [55, 61, 62]. Similarly, chemical doping techniques have been used successfully to dope semiconducting molecular assemblies [49, 55].

In addition to doping, the dominance of either electron or hole transport in a molecular device will depend on the interface between the electrodes and the molecular layer as this determines the entrance of charge carriers into either the HOMO (holes) or LUMO (electrons).

When a semiconducting material is brought into contact with a metal, the chemical potentials on each side must be equalized to maintain thermodynamic equilibrium. To achieve this equilibrium, charges from the materials can be moved towards the interface causing energy bands to bend and dipoles to form around the interface [40]. While this interfacial interaction is perfectly credible for inorganic semiconductors, molecular assemblies have been found to behave differently. The weak van der Wals interaction between individual molecules implies that the charge carriers are localized, and their reallocation to the interface can be quite different to that occurring in the more conductive inorganic semiconductors [63]. In addition the amount of adsorption (adhesion) of molecules onto the metal surface can vary greatly

(10 meV for weak physisorption to several eV for strong chemisorption) and can largely affect the state of the resulting interface [64].

In the last decade such interfaces have received a considerable amount of attention. In spite of the appreciable progress made, many aspects of the metal-molecule interfacial interaction remain a mystery. Current models of organic devices apply band bending in certain cases (solar cells) and ignore it in others (light emitting diodes) [63]. Photoemission spectroscopy experiments have shown that the formation of interface dipoles occurs in most metal-molecule interfaces [65, 66, 67]. The presence of such dipoles has been attributed various origins such as charge transfer, metal-induced interface states, chemical bonding and permanent molecular dipole moments [68, 69, 65, 70].

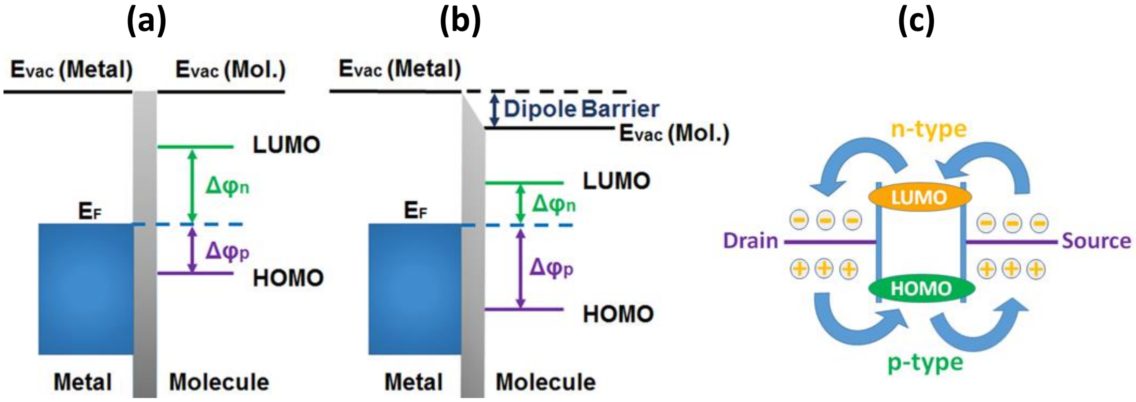

Figure 8. (a)Metal-molecule interface without dipole (Shottky-Mott Interface [71, 72]) (b) Dipole barrier causes the trasport barriers into the LUMO and the HOMO to change. (c) n-type and p-type transport

Interface dipoles appear as an energetic discontinuity between the metal and molecular vacuum levels. Its graver consequence is the shift of the positions of the HOMO and LUMO levels with respect to the metal Fermi level. This causes a simultaneous change of the potential barriers for electron or hole transport which can result in materials that are normally n-type being found (or engineered) to exhibit p-type behavior and vice-versa.

Charge transport in molecular devices is a multifaceted process, many aspect of which have not yet been fully understood [50, 51]. However the unique structural and thermodynamic properties of molecular assemblies as well as the ability to chemically tune the electrical and optical properties of molecular semiconductors has kept researchers highly interested in the field. Molecular assemblies have already found their way into several commercial applications and their vast potential will ensure them a growing presence in future electronic devices.

1.6 Single Electron Transistors:

In this section we present the theory relevant to single electron transistors (SET) which appear in chapter 3. As the name suggests, SETs have a transistor-like geometry, where a conduction channel is found between three terminals (Source, Drain and Gate). The conduction channel, consists of a small conducting island or dot, such as a nanoparticle. The island is coupled to the source and drain terminals via tunnel barriers, and to the gate terminal via a dielectric layer. The capacitive coupling of the electrodes to the nanoparticle, means that a potential change in the three electrodes can modify the electrostatic potential of the dot.

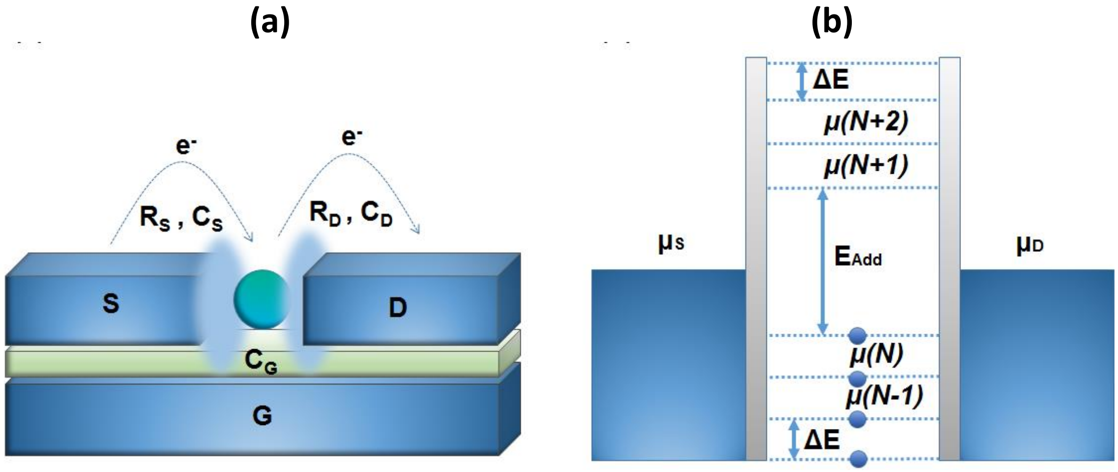

Figure 9. (a)Single Electron Transistor (SET). R represents the tunnel resistance of the barriers around the island, C is the capacitance and S,D and G represent source drain and gate electrodes respectively (b) Energy landscape of SET, adapted from [73]

The interest in miniscule conducting particles, comes from the charge quantization effect [74], a unique transport characteristic, which was first observed experimentally in 1987 [75] and arises directly from the small size of the island [40]. When the dimensions of the island are comparable to the Fermi wavelength (i.e. the de Broglie wavelength at the Fermi level), size quantization can transpire (see Table 1). In this scenario, the interference of electron waves can lead to the formation of discrete energy levels [50] and the island will behave like an artificial atom.

The tunnel junction coupling of this dot to the device's electrodes results in its partial electrical isolation. Although electrons can move onto and off the dot, doing so will require them to tunnel. Hence, under the right conditions the island can be considered to contain a well-defined number of electrons N, within it.

For an island with N electrons, the electrostatic energy (U_e) is expressed as $U_e = (Nq^2)/2C$, where C is the total capacitance of the dot to its surroundings ($C = C_S+C_D+C_G$). The total energy of the island can be written as [76]:

$$U(N) = \sum_{i=1}^{N} E_i + \frac{(Nq)^2}{2C} \qquad (18)$$

where E_i is the chemical potential of an island containing i electrons. The minimum energy needed to add the Nth electron to the island, i.e. its electrochemical potential is given by:

$$\mu_N = U(N) - U(N-1) = \sum_{i=1}^{N} E_i + \frac{(Nq)^2}{2C} - \sum_{i=1}^{N-1} E_i + \frac{((N-1)q)^2}{2C}$$

$$= E_N + \frac{(2N-1)q^2}{2C} \qquad (19)$$

Then, to add one more electron we require an energy of $\mu_{N+1} = U(N+1) - U(N)$:

$$\mu_{N+1} = \sum_{i=1}^{N+1} E_i + \frac{((N+1)q)^2}{2C} - \sum_{i=1}^{N} E_i + \frac{(Nq)^2}{2C} = E_{N+1} + \frac{(2N+1)q^2}{2C}$$

Combining the above equations we find:

$$\mu_{n+1} - \mu_n = E_{N+1} - E_N + \frac{(2N+1-2N+1)q^2}{2C} = E_{N+1} - E_N + \frac{q^2}{C}$$

$$E_{Add} = \mathit{\Delta} E + \frac{q^2}{C} \qquad (20)$$

This electrochemical potential difference, represents the difference in energy between occupied and unoccupied energy levels within the dot, and thus the total energy that will be gained by adding an electron to it. The term ΔE represents the energy difference between the dot's quantized levels and is a measure of the discretization in effect. The term q^2/C, is the charging energy E_C which represents the Coulomb repulsion of the electrons already occupying the island.

In a SET, this energy gap between the island's occupied and unoccupied levels is manifested as an absence of states on which the Source/Drain electrons can tunnel. As a result, a region of energy exists for which transport is blocked. This phenomenon, is a characteristic aspect of SET transport and is known as Coulomb Blockade (CB).

The blockade can be lifted by shifting the SETs energy landscape appropriately. Applying a potential difference between the leads can result in the μ(N+1) level being situated between the source and drain Fermi levels. In this scenario, electrons are able to tunnel from one lead onto the dot and then from the dot onto the other lead in a two step tunneling process. While the μ(N+1) level is kept between the two Fermi levels, this process will repeat continuously, and electrons are transferred across the channel one at a time in a process known as sequential tunneling.

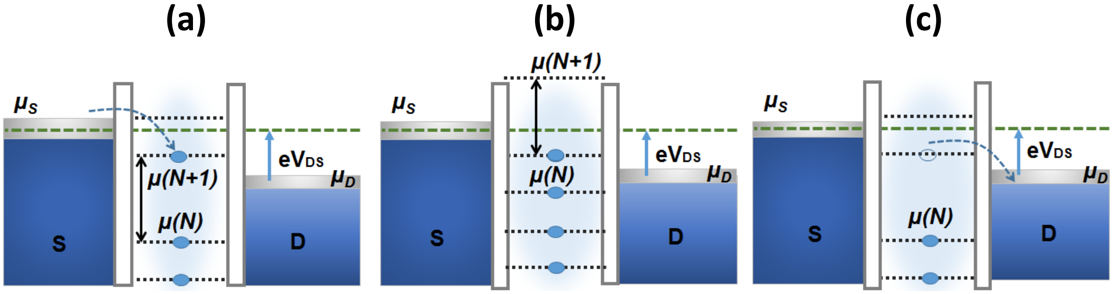

Figure 10. Applying V_{DS} lifts CB. (a)Tunneling from source electrode to dot. (b)Addition of electron raises the energy of the dot by E_{Add}.(c) Electron Tunnels off the dot and into the drain electrode. Images adapted from [73].

Another way to overcome the blockade, is by applying a positive gate voltage. The positive gate voltage on the gate will pull the μ(N+1) level down so that it is aligned with the Source and Drain Fermi levels. This way transport is once more allowed. Note that although the gap size is E_{Add}, since the gap is situated at the electrode Fermi levels, the shift in energy needed to overcome the CB is only $E_{Add}/2$.

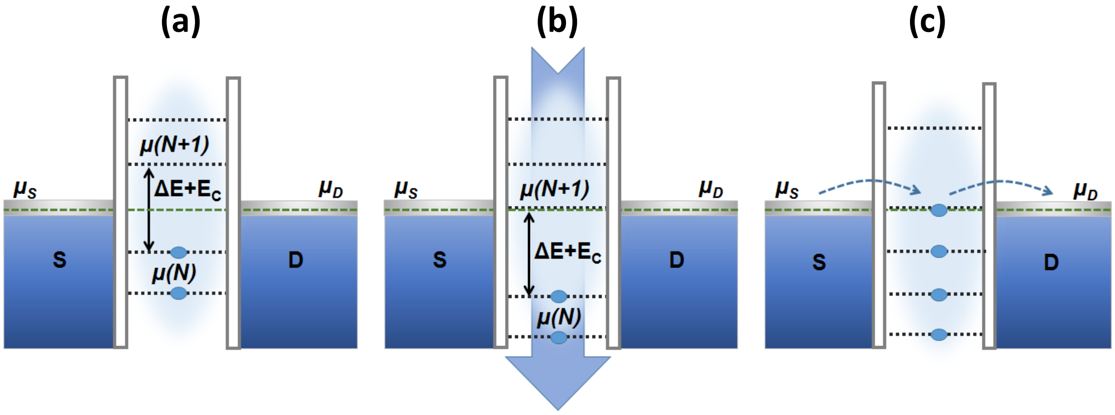

Figure 11. Lifting CB by applying a gate voltage. (a)Equilibrium (b) Positive gate voltage aligns μ(N+1) with electrode Fermi levels (c)Tunneling from Source to Drain via the dot

To observe CB, the resulting gap, should be larger than the energy fluctuations of the Source/Drain electrodes due to thermal energy k_BT (25.8meV for T=300K, 0.17meV for T=2K), $E_{Add} > k_BT$. This allows for the source/drain electrons to *feel* the gap. Furthermore, the relationship between the thermal energy and the energy level spacing ΔE determines the significance of the size quantization in the transport, and is often used to further categorize the system. If the thermal energy k_BT is larger than the energy level spacing ΔE, then the tunneling electrons can access what is effectively a continuum of available states on the dot. In this case the dot is called a classical dot. When $\Delta E > k_BT$, then the individual levels of the dot can be observed and the dot is referred to as a quantum dot. For metals the free electron density is so large, that to obtain a quantum dot, nanoparticles should be no bigger than a few nanometers wide. For semiconductors, the free electron density is much smaller and appreciable size quantization effects are present for dots of around 100nm.

Another condition for CB observation is that the number of charges on the dot, is well defined. To ensure this, we must ensure that the fluctuations of the charge state that may occur, occur on a time scale larger than our measurement. To turn this into a more concrete condition, we can say that shortest time taken to charge the dot by an electron is $\Delta t = R_tC$, where R_t is the smallest of the two tunnel junction resistances. Knowing that the charge of one electron changes the electrostatic potential energy by q^2/C many authors [76, 77] make use of the Heisenberg uncertainty principal to set a limit for Coulomb blockade detection, $\Delta E\Delta t = (q^2/C)*R_tC \geq h$. This implies that to observe CB, the smallest contact resistance to the dot should exceed h/e^2. Hence, when measuring SETs we are subject to the following conditions:

So that electrons feel a gap: $\boldsymbol{E_{Add} > k_BT}$

So that the dot charge state is well defined: $\boldsymbol{R_t > h / q^2}$*,*

So that individual discrete levels can be discerned: $\Delta E > k_BT$

The last condition above, is not a prerequisite for the observation of CB, but for additional observation of the dots energy discretization. The second condition, can be used to introduce an important concept of SET, coupling. It states that to observe CB the dot must be well isolated from, or weakly coupled to the leads. The coupling Γ, between the dot and the leads is determined by the amount of overlap between the electron wavefunctions on the dot and in the leads. In principle, this overlap should depend on the charge state of the dot and hence the coupling should be a function of the number of electrons occupying the dot [78].

Depending on the total coupling of the channel $\Gamma=\Gamma_S+\Gamma_D$, the SET is said to operate in either the weak or strong coupling regimes. In the weak coupling regime, the tunnel resistances are high, the charge state well defined and the transport is dominated by so called first-order tunneling processes. As the dot's isolation weakens and the states of the dot and the electrodes hybridize appreciably, we enter the strong coupling regime, where transport is dominated by higher-order tunneling processes.

First-order tunneling processes refer to tunneling where transport occurs via allowed states, one electron at a time. An example is the sequential tunneling described above. Higher-order processes involve tunneling via virtual forbidden states and can involve more than one tunneling process at a time. Examples of higher-order processes include elastic and inelastic cotunneling and the Kondo effect.

Such processes can blur the CB effect by causing non-negligible conductance in the blockaded regions. Considering the above conditions for observing CB, one can see than CB is more visible while weak coupling is present and becomes increasingly blurred as the coupling increases. A third regime, called the intermediate coupling regime may also be defined, where CB is observable but higher order tunneling processes are present. In chapter 5, we discuss only weakly coupled dots, and hence we will not go into further details here.

1.7 Spintronics:

Spintronics [79] or spin electronics, is an alternative to mainstream electronics that makes use of the spin angular momentum of carriers to generate, store and process information. In chapter 5 we study a spintronic device known as the lateral spin valve (LSV) whose operation is based on the use of spin-polarized current. The specifics of this device will be discussed in the next section. In this section we discuss spin angular momentum and its significance in the field of spintronics.

Spin is a quantum mechanical property of elementary particles. Although its explanation is found deep in relativistic quantum mechanics, it can simply be visualized as an intrinsic angular momentum of particles, as if they were spinning about their own axes [80, 81]. In a preferential axis, this *spin angular momentum*, S_Z, is quantized as $S_Z = m_S \hbar$ where m_S is the *spin projection quantum number*. The quantization of m_S allows two possible values. These are $m_S = \frac{1}{2}$ and $m_S = -\frac{1}{2}$ and correspond to the *spin up* and *spin down* states respectively [82].

This quantized angular momentum of particles has a magnetic dipole moment associated to it. Together with orbital angular momentum, spin angular momentum is hence responsible for the magnetization (moment per unit volume) of materials. For simplicity, when we speak of spin in this section we will in fact refer to the magnetic moment associated to the spin angular momentum. Similarly in the context of devices, electrons with same spin orientation will simply be referred to as spins, and their motion as spin transport.

Materials with an intrinsic net magnetization are called ferromagnets (FM). Net magnetization is a result of a difference between the number of spin up and spin down electrons which arises from the exchange interaction of electrons in certain materials. The most well-known FM materials (^{26}Fe, ^{27}Co, ^{28}Ni) are transition metals, which have a partially filled 3d band and whose active electrons come both from the 4s and the 3d orbitals.

The Pauli Exclusion Principle states that the many-electron wavefunction of indistinguishable fermions (i.e. electrons occupying the same orbital) must be antisymmetric. In FMs compliance with this principle is achieved by aligning the electron spins parallel to one another. This minimizes the overlap of the spatial component of their wavefunctions and while causing a reduction of the inter-electron Coulomb repulsion it achieves an antisymmetric many-electron wavefunction [83]. The crucial implication of this exchange interaction is that the 3d spin sub-bands of FM shift with respect to each other causing an imbalance between the spin-dependent density of states (DOS) [84]. The density of states in a FM metal is illustrated in Fig. 12.

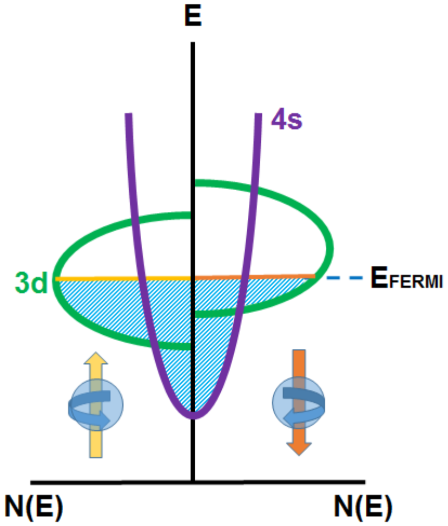

Figure 12. Density of states of a FM metal

In FMs, the density of states (DOS) at the Fermi level for spin up and spin down electrons is different. As a result the spin up and spin down electrons, can have different Fermi velocities, and scattering behavior. When such an imbalance of spins is present, the spin type with the largest population is called the majority spin type and the type with the smallest population is called minority spin type. Given the distinct DOS, each type of electrons can conduct differently. The spin dependent conductivity in each channel is given by the Einstein relation [85]:

$$\sigma_{\uparrow\downarrow} = q^2 N(E)_{\uparrow\downarrow} D_{\uparrow\downarrow} \tag{21}$$

Here $\sigma_{\uparrow c}$ is the spin dependent conductivity, q is the electron charge, $N(E)_{\uparrow\downarrow}$ is the spin dependent density of states and $D_{\uparrow\downarrow} = \frac{1}{3} v_{\uparrow\downarrow} l_{e\uparrow\downarrow}$ is the spin dependent diffusion coefficient with $v_{\uparrow\downarrow}$ representing the Fermi velocity and $l_{e\uparrow\downarrow}$ the electron mean free path. Clearly, $\sigma_{\uparrow}$ is found by using $N(E)_{\uparrow}$ and $D_{\uparrow}$ while $\sigma_{\downarrow}$ is found by using $N(E)_{\downarrow}$ and $D_{\downarrow}$. This imbalance in the DOS, allowed Mott to put forward his renowned two-channel model in 1936 [86]. In this model FM materials are portrayed as if they consisted of two distinct parallel conduction channels, one for spin up transport and one for spin down transport.

Given an imbalanced spin population during transport implies that our resulting currents will be spin polarized. The polarization, P_F of a FM can thus be defined as:

$$P_F = \frac{\sigma_{\uparrow} - \sigma_{\downarrow}}{\sigma_{\uparrow} + \sigma_{\downarrow}} \tag{22}$$

In the late 1980s, A. Fert and P. Grunberg [87, 88] produced groundbreaking work, in which devices using spin-polarized current exhibited the giant magnetoresistance effect (GMR). This discovery is often regarded as the starting point of modern spintronics and was awarded the Nobel prize in 2007.

Magnetoresistance (MR) is effectively the change in the resistance of a material due to an applied magnetic field. Many types of MR exist with different physical origins. Although MR effects have been observed as far back as 1856 [89], until the discovery of GMR the effect they resulted in about a 2% change of resistance [90]. The discovery of GMR and its subsequent variants [91, 92, 93] paved the way for so called first-generation spintronic devices such as hard-disk read heads and magnetic random access memory (MRAM) [94]. Advancement of the devices have enabled devices to present MR (TMR) in excess of 600% [95, 96]. The GMR effect and a corresponding two channel model are depicted in Fig. 13.

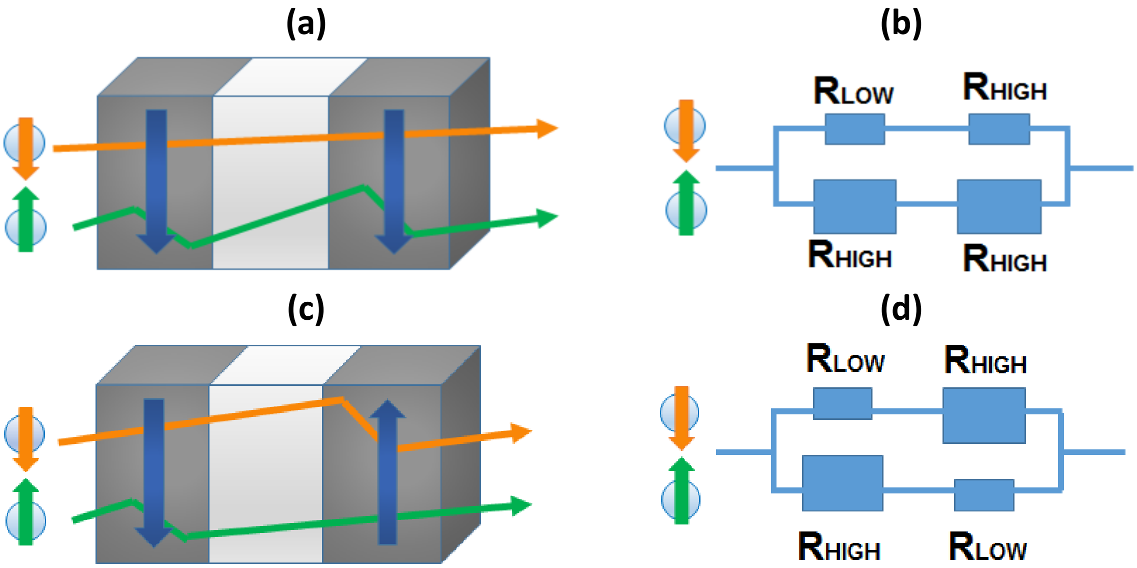

Figure 13. Spin dependent electron transport. Charge transport through a FM/NM/FM tri-layer and the equivalent circuit model for (a, b) parallel and (c, d) anti-parallel state. For most materials, the total resistance in (b) is lower than the total resistance in (d)

When electrons are made to transverse multiple FM layers of distinct magnetization directions, we find that the resistance is lower when the FMs are oriented parallel to each other. By choosing FM layers with distinct coercivities, an externally applied magnetic field can be used to switch the magnetization of layers individually.

In a magnetic field, electrons will align their spins to the direction of the field. As a result, electrons in FMs, will try to align their spins to the direction of the net magnetization and during transport will feel an augmented resistance when the FM's magnetic orientation is different from their own. If we make electrons transverse multiple FM layers, we find that the resistance is lower when the FMs are magnetically oriented parallel to each other. This concept brought forth the device known as the Spin Valve, whose easily accessible and well defined resistive states (parallel and antiparallel) have revolutionized modern memory storage applications.

1.8 Lateral Spin Valves:

In chapter 5, we study the dynamics of spin currents in one of the most studied spintronic devices, the lateral spin valve (LSV). The LSV, was first realized by Johnson and Silsbee in 1985 in a ground breaking experiment [97], and since then has fueled a vast amount of research. This device, consists of two ferromagnetic metals (FM) connected by one non-magnetic metal (NM) as depicted in Fig. 14(a). The FMs are used to inject and detect same spin electrons (spin populations) inside the NM. The LSV belongs to the second generation of spintronic devices as it is capable of employing spin currents without a net transfer of charge. Such currents are known as pure spin currents and will be explained below. In this section we will review the basic features of the LSV devices as is relevant for the work presented in chapter 5.

1.8.1 Spin Injection, Spin Accumulation & Spin Detection:

The steady state of a NM is one where the spin sub-bands of the DOS are equilibrated. If an imbalance is forced to occur in the DOS of the NM, a finite time period will have to elapse before returning to equilibrium. In this case, an excess of a given spin type (i.e. a spin population) is temporarily present in the NM. In spintronic devices, spin populations can be created within NMs using any of several methods (eg. spin pumping, optical, thermal) [98-100]. For the LSVs of chapter 5, such spin imbalance is created by forcing a spin polarized current to flow from a FM electrode into the NM. When the spin polarized current enters the NM, the majority type (↓ in Fig. 14(b)) electrons occupy more available states than the minority type (↑ in Fig. 14(b)) electrons resulting in a temporary shift of the spin sub-bands of the NM. This shift represents the excess spin population, or *spin accumulation* within the NM. The creation of spin accumulation in such a way is known as *electrical spin injection*.

As illustrated in Fig. 14(b) the spin imbalance in the FM can be transferred to the NM. The induced spin accumulation is quantified by the shift in the electrochemical potential (ECP), which amounts to $\Delta\mu/2$ for each spin sub-band. The ECP can be expressed by $\mu=\varepsilon^F+q\phi$, where ε^F is the Fermi Energy level and ϕ is the electrical potential energy. This amount $\Delta\mu$ can be expressed as a potential difference from the Fermi level, or a Voltage given by $V_S = \Delta\mu/2q$ for each spin sub-band.

(a) **(b)**

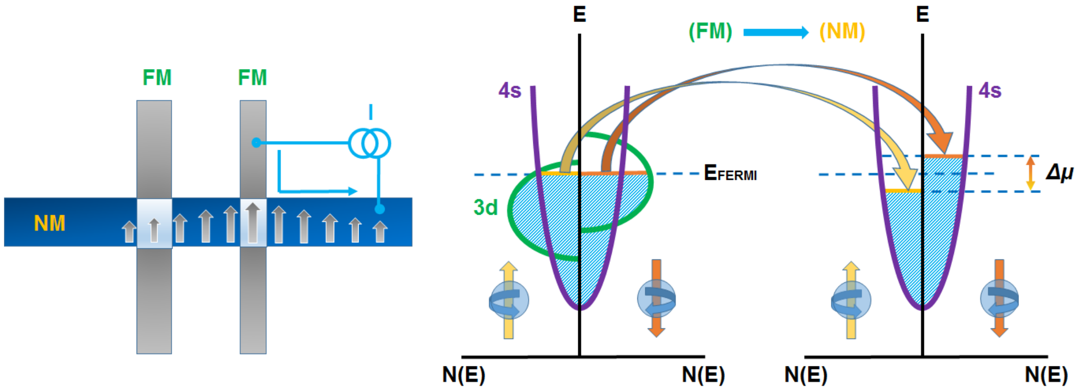

Figure 14. (a) Schematic of spin injection by means of a spin polarized current through a FM/NM interface in a LSV. The excess spins injected at the interface diffuse equilaterally throughout the NM. (b) DOS viewpoint of spin injection. The imbalance in the DOS of the FM is transferred to the NM causing each spin sub-band to shift by Δμ/2 from the Fermi Level.

When a detector FM is placed in proximity to the injection point, depending on its magnetic orientation it will align its Fermi level to either the majority (parallel) or minority (antiparallel) spin sub-bands of the NM channel [101].

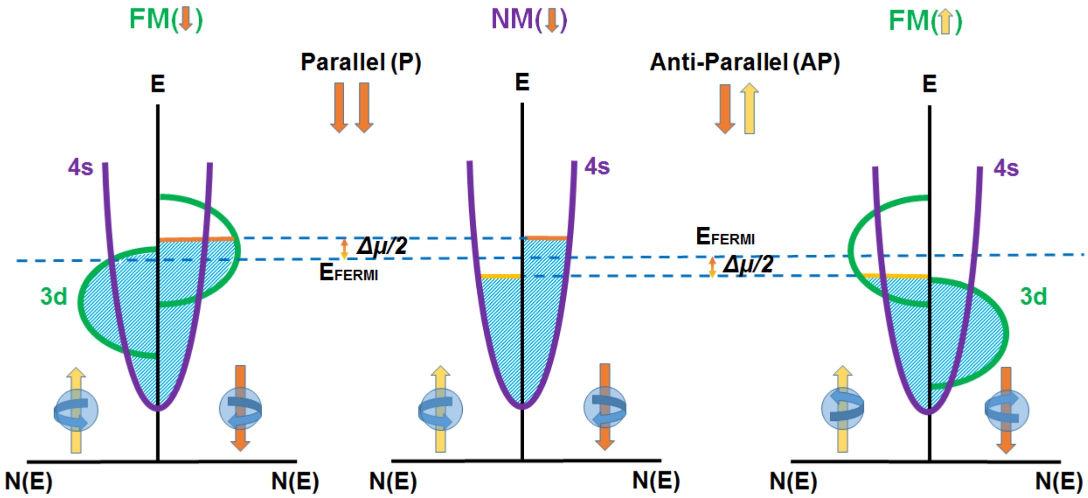

Figure 15. Detection of spin accumulation in a NM. Depending on the magnetic orientation of the detector FMs, the interfacial voltage of Vs = + Δμ/2q or Vs = - Δμ/2q will arise at the detector interface.

Hence at the detector FM/NM interface the Fermi level of the FM will be Δμ/2 away from the Fermi level of the NM. This will give rise to a measureable voltage $V_{S(P/AP)} = \pm \Delta\mu/2q$. Application of an external magnetic field can change the relative orientation of the two FMs from parallel to antiparallel giving rise to $V_{S(P/AP)}$ each time. In doing so, we can determine the interfacial voltage which represents the total spin accumulation at the detector interface, $V_S = \Delta\mu/q$. The DOS perspective of spin detection is illustrated in Fig. 15.

1.8.2 Spin Diffusion and Spin Relaxation:

The injection of spins into a balanced NM, gives rise to a gradient of carrier density concentration for each spin type. In accordance to the two channel model described above, the electrical current density for each spin channel can be expressed as [85]:

$$j_{\uparrow,\downarrow} = \sigma_{\uparrow,\downarrow} E - qD_{\uparrow,\downarrow} \nabla n_{\uparrow,\downarrow} \tag{23}$$

where j is the current density, σ is the conductivity, E is the applied electric field, q the charge of the electron, D the diffusion coefficient and ∇n is the spatial gradient $\left(\frac{dn_{\uparrow,\downarrow}}{dx}\right)$ of the carrier density within the conductor.

In the example of Fig. 14(a) we see that the spin polarized current is injected from the right-most FM/NM junction and flows towards the right side of the channel. The current in the right side of the injection point will hence be the superimposed currents due to the spin density gradients $\left(\frac{dn_{\uparrow,\downarrow}}{dx}\right)$ and the electric field. On the left side of the injection point, the electric field is absent and the carriers will move only to balance the spin populations. While the majority spin population will move away from the injection point, the minority spin population will move towards it. Given that the gradients are of equal strength and opposite direction, the majority and minority electrons will be displaced by equal amounts within the metal. As a result the total charge transfer in this process is zero, and the electron transfer taking place is referred to as a *pure spin current*.

Spin current is hence the diffusive distribution of spin accumulation, Δμ, due to distinct spin dependent carrier densities. Remembering Equation 21, and using $\nabla n = N_{\uparrow,\downarrow}(E)\nabla\varepsilon^F_{\uparrow,\downarrow}$, the spin dependent current density can be expressed as:

$$j_{\uparrow,\downarrow} = -\frac{\sigma_{\uparrow,\downarrow}}{q}\frac{d\mu_{\uparrow,\downarrow}}{dx} \tag{24}$$

The charge current density is given by $j_C = j_\uparrow + j_\downarrow$ the spin current density is given by $j_S = j_\uparrow - j_\downarrow$. Note that the values (and directions) of $j_\uparrow$ and $j_\downarrow$ and consequently j_C and j_S are independent of each other. In Fig. 16, we see an illustration of the distribution of the ECP throughout a LSV. Here, current is injected via the left-most FM/NM interface causing spin accumulation. The colored lines depict the spin dependent ECPs. As we move away from the injection point, the spin population is being balanced and the spin splitting of the ECP decreases within the NM. Finally the accumulation within the NM is detected a distance L away from the injection point by a second FM/NM interface.

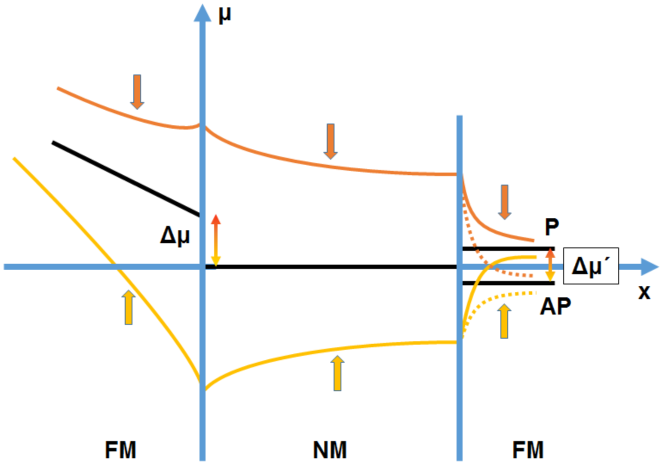

Figure 16. Schematic of the electrochemical potential for a LSV. Spins are injected at the left-most FM/NM interface creating a spin accumulation Δμ. Within the NM, the spin population decays. At the second FM/NM interface spin accumulation Δμ´ can be detected as the difference in interfacial voltage between the parallel and anti-parallel cases.

To detect spin accumulation we require a second FM electrode to be placed in proximity to the injection point. This proximity is defined by the amount of time (or space) needed for the spin accumulation to be neutralized. In addition to diffusion, equilibration of excess spins can occur due to spin flipping or spin relaxation, a process whereby an electron of a certain spin type is turned into an electron of opposite spin type. Spin relaxation is related to how conducting electrons interact with their surroundings (defects, phonons, nuclei and even other electrons). These interactions can affect the electrons angular momentum causing spin dephasing and even complete spin reversal (spin flip) to occur. Spin relaxation occurs via four major mechanisms: the Elliot-Yafet mechanism (mainly in metals), the Dyakonov-Perel mechanism (mainly in semiconductors), the Bir-Aronov-Pikus mechanism (in highly doped semiconductors) and the hyperfine interaction [102].

In the devices of chapter 5 spin transport occurs in metals, and the dominant spin relaxation mechanism is Elliot-Yafet (EY) [103, 104]. The EY mechanism states that during scattering events electrons can experience spin reversal due to the spin-orbit interaction. According to this mechanism the spin lifetime, or spin flip scattering time τ_{sf} is proportional to the momentum scattering time τ_e. The EY relationship ($\tau_{sf} \propto \tau_e$) implies that the time taken for the electron to have its spin reversed is inversely proportional to the number of scattering events taking place [81, 105, 106]. In this framework, spin lifetime decreases in materials with strong spin-orbit coupling and large resistivity.

The spin lifetime describes how long it will take (on average) for a single electron to flip its spin. For spintronic applications, a more interesting question is how far spin currents will propagate. This characteristic is quantified by the spin diffusion length λ, defined as the shortest distance between the spin injection point and the point of spin balance in a material. The relationship between λ and τ_{sf} is given by:

$$\lambda = \sqrt{D\tau_{sf}} \tag{24}$$

Although τ_{sf} reflects the relaxation process, λ reflects the decay of the spin population, whether it is due to diffusion or relaxation. Hence for spintronic applications λ is usually a more interesting quantity. The average cumulative distance travelled by an electron prior to spin flip is called the spin flip length, l_{sf}, and can be estimated by $l_{sf} = v_F\tau_{sf}$, where v_F is the Fermi velocity. This value reflects electron motion in every possible direction and is much larger than λ. Nevertheless, for spintronic applications λ is by far a more relevant parameter.

To detect an appreciable spin accumulation the spin transport channel is chosen to be a material with large λ. This generally implies materials exhibiting low spin orbit coupling and low resistivity. These conditions are generally fulfilled by materials with low atomic numbers (Z) and high crystallinity. Demonstration of appreciable spin transport has been shown both in metals and semiconductors [107, 108].

1.8.3 Modelling Spin Transport:

In the LSVs of chapter 5, spin transport is examined in the context of the one-dimensional (1D) spin diffusion model [109]. This model is applicable for devices with dimensions considerably smaller than λ, in which framework the 1D spin diffusion equation can be formulated as:

$$\frac{\partial^2(\mu_\uparrow - \mu_\downarrow)}{\partial x^2} = \frac{(\mu_\uparrow - \mu_\downarrow)}{\lambda^2} \tag{25}$$

The extensive solution to Equation 25, allows the derivation of an expression for the spin accumulation at the detector interface. Appropriate parametrization demands continuity of charge and spin currents at the FM/NM interfaces and allows the introduction of device parameters. In this manner, an expression can be derived for the interfacial voltage V_S detected at any point L along the NM due to the injection of a spin polarized current. This expression is given below:

$$V_{S(P/AP)} = \pm 2IR_N e^{-L/\lambda_N} \frac{\prod_1^2\left(\frac{P_i R_i}{R_N(1-P_i^2)} + \frac{P_F R_F}{R_N(1-P_F^2)}\right)}{\prod_1^2\left(1 + \frac{2R_i}{R_N(1-P_i^2)} + \frac{2R_F}{R_N(1-P_F^2)}\right) - e^{-2L/\lambda_N}} \tag{26}$$

Here, I is the injected current, $R_N = \rho_N\lambda_N/A_N$ and $R_F = \rho_F\lambda_F/A_i$ are the spin resistances of the NM and the FM respectively, ρ is the resistivity, A_N the cross sectional area of the channel and A_i the area of the interface. R_i and P_i are the interface resistance and interface polarization respectively and L is the distance between injection and detection. The product indices 1 and 2 refer to the 1st and 2nd FM/NM interfaces respectively while the + and – signs correspond to the parallel and antiparallel alignments of magnetization (of the FMs).

In Equation 26, we see several important concepts for spin transport. Primarily, we see a spin equivalent to electrical resistance which we call spin resistance. Furthermore we see that the detected interface voltage is affected by the interfacial properties R_i and P_i. The importance of these parameters with on the spin transport in LSVs is discussed in the next section.

1.8.4 Spin Resistance and FM/NM Interfaces:

In LSVs the spin imbalance is transferred from a FM into a NM. The imbalance is present in the FM due to the exchange interaction which causes each spin sub-band to have distinct conductivities. This spin polarization can be further influenced by the resistance of the FM/NM interface which can lead to an interface polarization P_i, expressed as:

$$P_i = \frac{R_i^{\uparrow} - R_i^{\downarrow}}{R_i^{\uparrow} + R_i^{\downarrow}} = \frac{R_i^{\uparrow} - R_i^{\downarrow}}{R_i} \qquad (27)$$

The interfacial properties are of great significance to spin transport and are often used to classify spin valve devices. By comparing R_i to the spin resistances R_N and R_F, LSVs can be said to have either transparent contacts, resistive contacts or tunneling contacts. The devices of chapter 5 employ so called transparent contacts, where $R_i << R_N$, R_F. In this case, R_i can be set to zero and Equation 27 can be transformed into the much simpler Equation 28 below:

$$V_{S(P/AP)} = \pm 2IR_N e^{-L/\lambda_N} \frac{\prod_1^2 \left(\frac{P_F R_F}{R_N (1-P_F^2)} \right)}{\prod_1^2 \left(1 + \frac{2R_F}{R_N(1-P_F^2)} \right) - e^{-2L/\lambda_N}} \qquad (28)$$

Clearly, the interface polarization is absent from this scenario implying that the spin imbalance generated in the NM will depend solely on that present in the FM. LSV can also be created with resistive contacts whereby R_i is comparable to R_N and R_F and tunneling contacts where $R_i >> R_N$, R_F. In these cases the spin imbalance in the NM can be very different as additional polarization comes into play.

The effect of the interface is closely related to the concept of spin resistance, which much like electrical resistance reflects the difficulty for spins to transverse a certain medium. Increasing R_i makes it harder for injected spins to return to the FM electrode from which they came which results in a larger spin accumulation in the NM [110, 19, 20, 108].

Chapter 2:

NanoFabrication

2.1 Introduction:

For decades, the main method for defining structures in the electronics industry has been lithography. As the need for smaller structures grew, the technique evolved and its resolution was pushed into the nanometer regime. The continuous trend of miniaturization is now demanding sub-10nm device features which even the most advanced lithographic techniques are unable to provide.

Numerous alternative techniques have been proposed to overcome this limit but they cannot compete with the simplicity and reproducibility of lithography [111]. Currently, pushing features below 10nm is one of the greatest challenges of nanotechnology and an essential goal for next-generation devices.

In this chapter, we present the fabrication processes applied during this thesis and scrutinize the controlled minimization of device features. While larger structures are created by typical ultraviolet photo-lithography methods, the creation of sub-10nm features such as constrictions and nanogaps is approached using three distinct methods: *Electron Beam Lithography* (EBL), *Electromigration* (EM) and a method we refer to as the *Overhang Method*.

The purpose of our devices was to explore charge and spin transport in spatially confined metals, tunnel junctions and organic assemblies. For this reason two types of devices where made. For charge transport we create lateral transistors with air/vaccum channels between 1nm and 100nm which are used to probe ballistic transport, tunneling transport and organic transport in subsequent work. For spin transport we created lateral metallic spin valves which are presented in chapter 5.

Typically, the fabrication of devices involves starting with the less critical processes and moving onto the more critical processes. In the same way, we will first present a generic look on the method of lithography, and then focus on the methods used to push our structures towards a vanishing dimensionality. The processes involved in fabricating devices for this thesis can be seen in the Fig. 1.

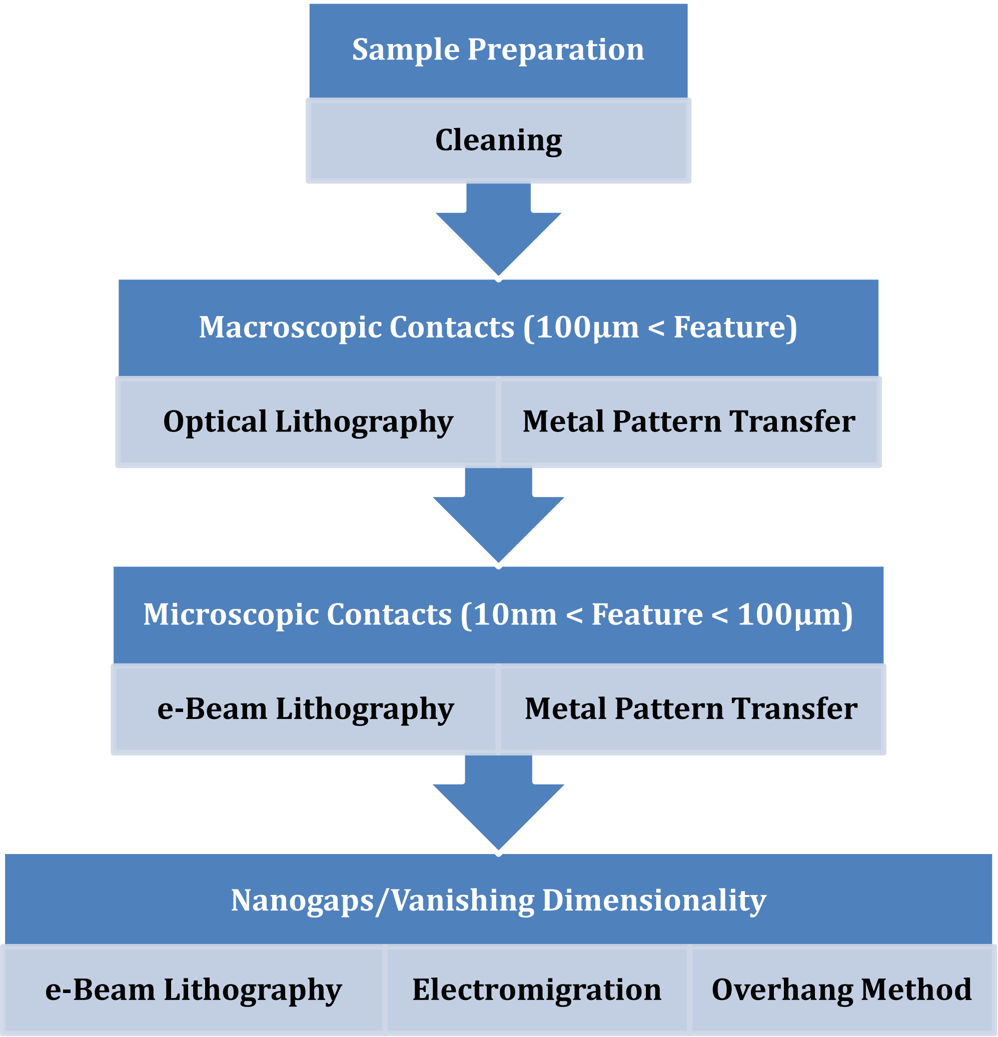

Figure 1. Flowchart of fabrication process

PART A:

Introduction to Fabrication

We begin this chapter by presenting the methodology applied to create basic device structures using lithography. Essentially, in PART A of this chapter we will look at the first three steps of the flowchart illustrated in Fig. 1. This process is applicable to all devices made during this thesis, including the spin valve structures and hence we believe it must be thoroughly reviewed.

2.2 Substrate Preparation:

The process begins with a Silicon wafer. All devices were made on 500μm thick, highly doped silicon (Si) substrates (both n-type and p-type) covered with 150nm-300nm thermally grown silicon dioxide (SiO_2). Silicon wafers were cut down to a chip size of 10mm x 10mm and every design implemented was fit into this area. When appropriate, the Si substrate was used as a gate (and the SiO_2 as the gate dielectric).

While in storage, substrates can accumulate a variety of unwanted substances on their surface. To ensure that the fabrication process begins with a pure SiO_2 surface the first step of any fabrication process is to clean the Si/SiO_2 substrate. For our samples we perform a standard cleaning process which consists of the following steps:

1) 5 min in Acetone under ultra-sonic (US) agitation
2) 5 min in Isopropyl Alcohol (IPA) under US agitation
3) Nitrogen (N_2) blow dry
4) 5min at 110^{o}C

During the above process, care must be taken to avoid damaging the substrate's surface. Tiny particles that are left in the beakers can damage the surface of the substrate during US agitation, and therefore steps 1 and 2 must be done using clean beakers and applying moderate US power. For many devices, the use of the substrate as a back gate is implemented by using the SiO_2 layer as a gate dielectric. If the dielectric is damaged, this can lead to considerable leakage currents which for many purposes renders the device useless.

Although cleaning is always the first step, it may also be implemented at other points throughout the fabrication process. Argon (Ar) ion milling is used to clean the interfaces of spin valve devices (see chapter 5), while soft Ar and oxygen (O_2) plasma can be used to remove spurious organic materials such as residue resist which can adhere to the device. When using such methods, care must be taken to avoid implantation of the highly energetic ions or unwanted etching. Although, the cleanliness of the substrate is not always critical, as we venture into the sub-10nm regime the structures become extremely delicate and careful, non-invasive cleaning is needed as small defects or impurities can decrease the fabrication's yield considerably.

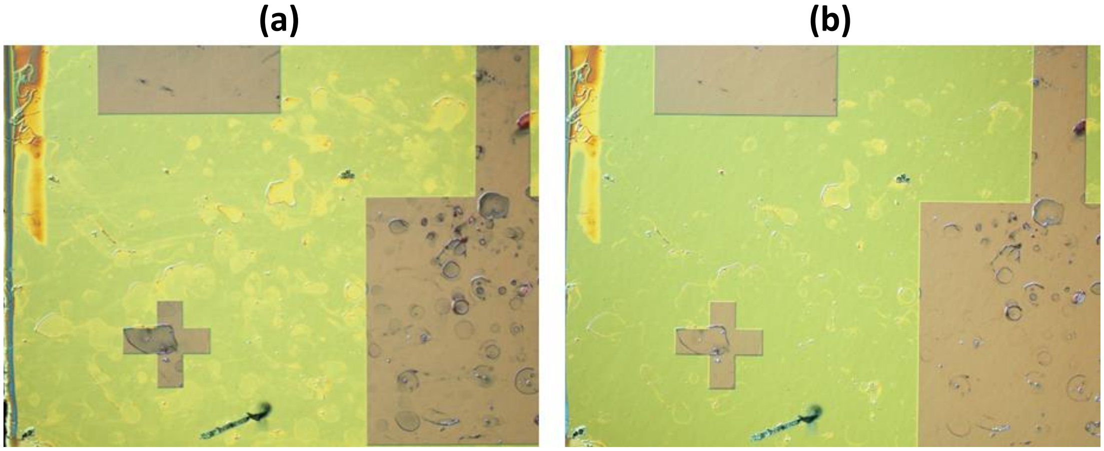

Figure 2. Optical microscope image of the effect of plasma cleaning. (a) Substrate surface covered with organic residues (b) Same substrate after soft plasma clean. After the cleaning, a considerable amount of residues has been removed.

2.3 Patterning with Lithography:

Lithography is a method of *printing* which has been in use for over 200 years. As it evolved, it made its way into the electronics industry as one of the principal techniques for transferring patterns onto a substrate. The working principal of lithography is similar to that of stencil printing. The original pattern is engraved into a sacrificial layer (a stencil) which is placed covering the surface on which we wish to *print*. Then a material is spread over the entire surface seeping through the sacrificial layer according to the engraved pattern. The sacrificial layer is then removed leaving only the material which directly contacted the underlying surface in the previously engraved pattern.

In the context of lithography, the sacrificial layer is called a resist and consists of a material which changes its chemical properties upon exposure to either photons or electrons of sufficient energy. By such exposure, the pattern can be engraved into the resist. After exposure, the substrate is submerged into a chemical called a developer, in which the exposed areas of the resist are selectively washed away revealing the engraved design in the resist. The lithography technique can also be compared to photography where light chemically changes a film, which is later developed. Once the pattern in on the resist, metal (or other materials) is deposited over the entire surface. The substrate is then submerged into a second chemical which selectively dissolves the resist layer leaving the metallic structure on the SiO_2 surface. The process can be summarized by the following steps:

1. **Resist Coating**
2. **Resist Exposure**
3. **Developing**
4. **Material Deposition**
5. **Lift-Off**

For this thesis, we apply photolithography for large scale patterning and electron beam lithography (EBL) to pattern smaller structures. Photolithography uses light to expose the resist and makes use of an additional pre-patterned stencil called a mask. EBL uses a highly energetic beam of electrons and a direct patterning scheme to pattern the resist. While EBL can achieve much larger resolution than photolithography it is considerably slower and hence is used only when necessary.
In the following two sections we will briefly present the two lithographic techniques used. Then, while focusing on EBL, we will scrutinize the fabrication process and see how each step influences the final resolution.

2. 4 Photolithography:

For several decades, photolithography has been the principal technology for patterning progressively smaller and denser features in microelectronic devices [112]. For this work, we use photolithography to efficiently pattern large areas such as our device's macroscopic contacts.

Photolithography uses an additional *stencil* and an ultra-violet (UV) light source to expose the resist. The additional stencil is called a mask and is prefabricated by patterning chromium (Cr) on glass. The substrate is covered by photosensitive resist, covered with the mask and then light is shone though the mask onto the resist. As light is blocked by the Cr pattern the resist under the Cr is not exposed and the mask's pattern is transferred to the resist.

For our structures we applied the positive resist S1818, which was spin-coated onto the substrate at 1500 rotations per minute (rpm) and baked on a hotplate at 115^oC for 1 min (see section 2.6.1). Pre-patterned masks where aligned to our substrates using a mask alignment system by EVG. Using a lamp power of approximately 18mW/cm^2, we found that a 10sec exposure to UV light and a 30sec development in MF319 can be used to pattern very large structures. Swirling of the beaker during development largely improves the results. To end the development the sample is rinsed in D.I. water and then dried with a N_2 gun. To ensure clear structures and minimize resist residues we recommend that while the sample is submerged in D.I. water the resist surface be sprayed with a D.I. water gun. We have found that the added turbulence improves the rinsing process drastically, resulting in much less resist residues in the structure.

The resolution of this system is limited by the wavelength of light and is generally much lower than that of EBL [112, 113]. The minimum achievable feature size (MFS) is given by [50]:

$$MFS = \sqrt{(d+g)\lambda} \tag{1}$$

where d is the thickness of the resist, g is the gap between the sample and the mask and λ is the wavelength of the incident light. Although our EVG system has a resolution of 1μm, the state of the art optical lithography systems have improved this number considerably. The efficiency of this method has inspired a great deal of effort to be directed towards maintaining optical lithography as the main patterning technique of the semiconductor industry. While standard UV photolithography uses a λ of around 300nm, Deep UV and Extreme UV lithography makes use of smaller wavelengths (λ<100nm) and can achieve much better resolution allowing for minimum feature sizes well-under 100nm [50, 114, 115]. Nonetheless the resolution of optical lithography is still inferior to that of EBL and the requirement of a prefabricated mask makes it less versatile and unattractive for research purposes.

2.5 Electron Beam Lithography:

The EBL technique enables the direct patterning of devices with nanometric features. Here, contrary to the case of photolithography the electron beam moves following a CAD design previously loaded in the system and a mask is not required. The simplicity of direct patterning makes EBL extremely attractive, especially for creating electrodes with nanometric features.

As with photolithography, the first step of this technique is to spin coat resist onto the substrates' surface. Once coated, the substrate is exposed to a high energy electron beam which defines the pattern directly into the resist layer. The exposed area can then be selectively washed away (resist development), leaving the desired design engraved in the polymer. The next step is to cover the surface (deposition/ materialization) with the material which we wish to print onto the SiO_2 surface. After the material has been deposited, the remaining polymer is dissolved and removed (lift-off), leaving the desired material in the pattern defined by the exposure.

The outcome of this technique depends on a multitude of parameters. For patterning, the key determinants will be the quality of the electron optics (e.g., the ability to create a finely focused spot), the choice of resist, substrate and developer, as well as the process conditions: electron beam energy and dose, and development time and temperature [116]. Moreover, even with a high quality patterning, the materialization of structures in this regime can be quite challenging and change the resulting features substantially.

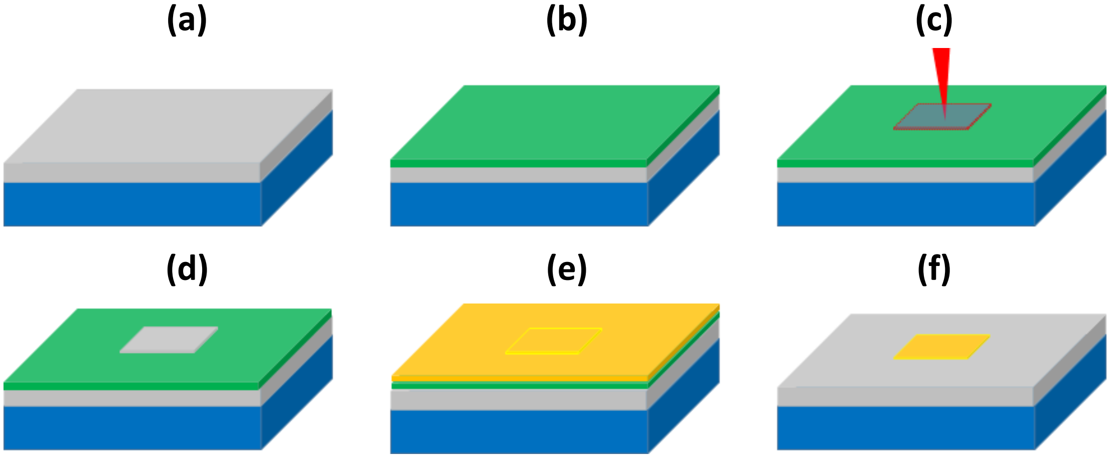

Figure 3. Work flow diagram of EBL process. (a) start with clean substrate (b) coat with resist (c) expose resist to e-beam (d) develop to remove exposed resist, creating resist window (e) deposit material (f) lift-off resist to reveal material structure

In pursuing sub 20nm features, the control and reproducibility of this technique start to decrease significantly and good control over the resulting structures requires a good understanding of how each step affects the process. In section 2.6, we take a closer look at the nuances of EBL and highlight important factors required to improve the minimum obtainable feature size.

2.6 A closer look at EBL:

2.6.1 Resist Coating:

For EBL, the most popular resists are the positive-tone organic resist poly-methyl-methacrylate (PMMA), the positive-tone chemically amplified resist ZEP and the negative-tone inorganic resist hydrogen silsesquioxane (HSQ). Positive-tone describes resist in which the exposed areas are developed and negative-tone refers to resists where the unexposed areas are developed.

Although many types of EBL resist are available, we will discuss organic chain-scission (a.k.a. crosslinking) positive-tone resist, which is the only type used during this work. For all our devices we chose to use PMMA dissolved in anisole. The reason was that our group already had experience using PMMA and the processing conditions were better controlled. This resist consists of a polymer solution and is deposited by spin-coating. The thickness of the resulting layer depends on the concentration of the solution and the spinning speed. Typical thicknesses are between 30nm and 500nm. Once coated, the substrate (and resist layer) is baked on a hotplate which removes the polymers solvent, increases the films density and reduces the films roughness [117]. Baking temperatures roughly vary between 150°C and 250°C and baking times vary between 15sec and 1day [118, 117]. We varied baking between 170°C for 10min and 195°C for 1min and no notable difference in resolution was observed. Given the much shorter baking time required, we chose to bake our resist layers at 190°C for 1min.

2.6.2 Resist Exposure:

Exposure of the substrate to a high-energy electron beam causes a scission of the resist layers' polymer backbone. The exposed area, hence consists of broken polymer chains with reduced molecular weight.

The resolution of the EBL patterning ultimately depends on the scattering of electrons within the resist. Elastic interactions will cause incoming (primary) electrons to deflect causing the incident electron beam to broaden. This effective beam diameter, or *spot size*, D_{eff}, is given by the empirical formula [119]:

$$D_{eff} = 0.9 \left(\frac{R_t}{V_b}\right)^{1.5} \qquad (2)$$

where R_t is the resist thickness in nanometers and V_b is the beam voltage in kilovolts [119]. Inelastic scattering events give rise to so-called secondary electrons. These are less energetic and responsible for the majority of the resist exposure [120]. Finally, in some cases, a particular series of scattering events with large scattering angles can result in backscattered electrons which move backwards, away from the substrate as if reflected.

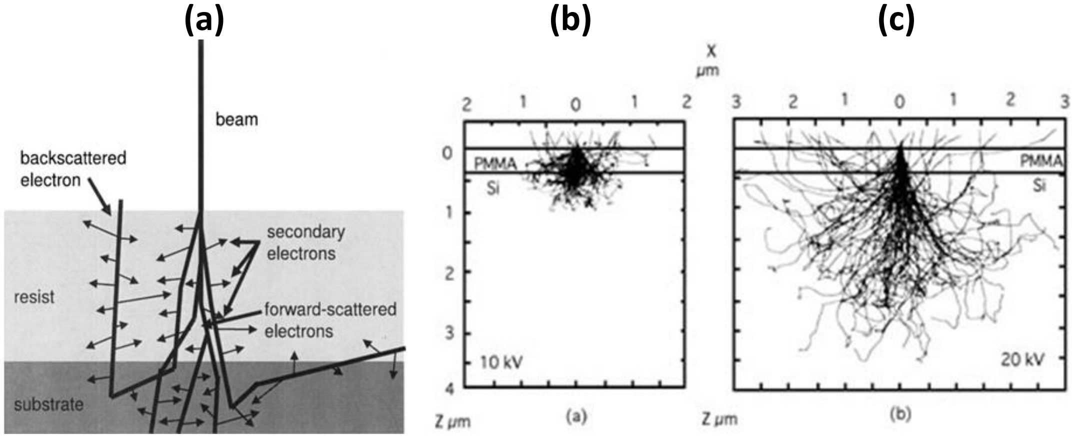

Figure 4. (a) Schematic of scattering of electrons in resist [121]. (b)Monte Carlo simulation of incoming electrons in resist for 10kV accelerating voltage and (c) 20kV accelerating voltage [122].

Backscattered electrons can travel a large distance away from where they entered the resist furthering exposure and broadening the shape of the pattern [121]. From Equation (2) we can see that larger accelerating voltage and thinner resist layers decrease the spot size and hence increase the resolution. This effect of the beam voltage on the exposure can be seen clearly via Monte-Carlo simulations of electron scattering in resist [123, 122].

As shown in Fig. 4(b), larger accelerating voltages create a sharper path towards the substrate with less scattering events occurring in the PMMA resist. In addition to the voltage the amount of scattering taking place also depends on the type of resist and the type of substrate. In a resist of lower molecular weight, the incoming electrons will experience a larger amount of scattering events giving rise to more polymer chain scission. The type of substrate influences the dissipation of charge within it. While metallic conductive substrate will attract and dissipate the incoming electrons efficiently, insulating substrates can result in charge accumulating at the area of exposure giving rise to additional scattering within the resist.

2.6.3 Proximity Effect:

The broadening of the beam due to scattering is often referred to as the proximity effect [120, 124]. Its most obvious consequence is a conical exposure profile which implies that the exposure of a feature will depend on exposure of nearby features and the final pattern may differ substantially from the one designed [125]. The proximity effect is directly related to the resolution of the EBL process [126], and lots of work has been done in order to understand and correct the excess exposure [125, 127-132].

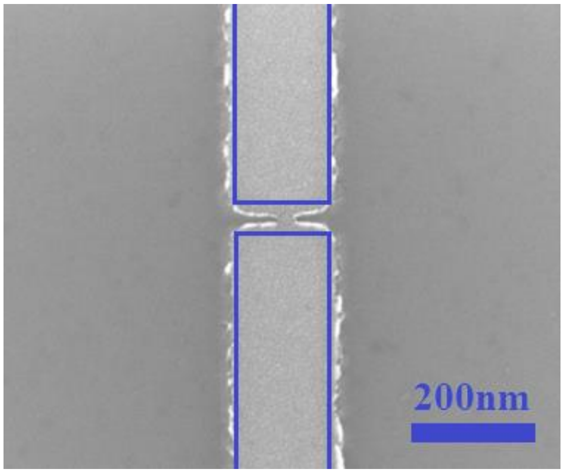

Figure 5. SEM image of swollen EBL structures due to the proximity effect. Blue line indicates designed structure.

In addition to the accelerating voltage, a very important parameter is the number of electrons that will be used to expose an area. This is known as the dose and typically assumes units of $\mu C/cm^2$. It is given by the product of the beam current and the dwell time (i.e. the time spent exposing each spot) [125] per area exposed. The dose is a critical parameter as it defines how much each area of the design will be exposed. While a minimum amount of electrons is needed to cause scission throughout the entire thickness of the resist, increasing the dose beyond that results in excess exposure and broadening of the desired pattern.

The majority of proximity correction methods apply a dose gradient in the CAD design pattern so as to compensate for exposure from backscattered and secondary electrons [133]. Although improvements can be seen, the method is geometry specific, labor intensive, increases the patterning time and does not completely solve the problem.

2.6.4 Development:

After the resist has been exposed to the electron beam, it is time to develop it. Development involves submerging the sample into a bath of the developer, a selective chemical which dissolves the exposed resist and reveals the embedded pattern. The development of PMMA is typically done in a mixture of Methyl Isobutyl Ketone (MIBK) and Isopropyl Alcohol (IPA). To stop the developing process, the sample is transferred into a bath of IPA.

As discussed earlier, the development involves the removal of low molecular weight polymer fragments that the electron beam has broken off. The dissolution rate of the resist, D_{diss}, follows a kinetic diffusion-like process described by the following equation [116, 134, 135]:

$$D_{diss} = Ae^{\left(-\frac{\Delta E_a}{kT}\right)} \tag{3}$$

where A is a constant, ΔE_a is the PMMA activation energy (which is a function of the molecular weight), k is Boltzmann's constant and T is temperature. Although, both the molecular weight and the temperature play an important role in development, at low temperatures (approximately -10^{o}C) the effect of the molecular weight has been found to be negligible [136].

While a multitude of developers can be applied, our standard procedure involved using a 1:3 part mixture of MIBK:IPA at ambient temperature. Using this developer optimum resist resolution has been reported while developing at -15^{o}C. Alternatively, increased resolution has been reported using either IPA [137] or a mixture of IPA and water [118, 123] to develop PMMA resist.

In an attempt to improve the resolution the developer was stored in a refrigerator at -2^{o}C. Cold developing was found to require approximately three times more time than ambient developing and (after lift-off) no clear improvement in resolution was observed. While simple IPA development requires excessive amounts of time, developing with a mixture of IPA and water caused a large decrease in reproducibility. This developer was not commercially available, and the mixing ratio has been shown to largely affect the resulting developer properties. In our attempt to improve the resolution, we mixed IPA and de-ionized water with a 7:3 (IPA:H_2O) ratio which has been found to give optimum performance [118]. Again no clear improvement was observed and due to the unsettling uncertainty that the mixing ratio was being replicated perfectly, we decided to revert to using commercial MIBK:IPA(1:3).

An important design consideration when pushing to the nanoscale is the edge slope of features in resist. This will ultimately depend on the combination of exposure and development conditions and can result in both positive and negative slopes [138]. The edges of exposed features will almost never be entirely vertical and in many cases, the slope can be quite large. In fact, a slope is often used intentionally, to facilitate subsequent fabrication processes.

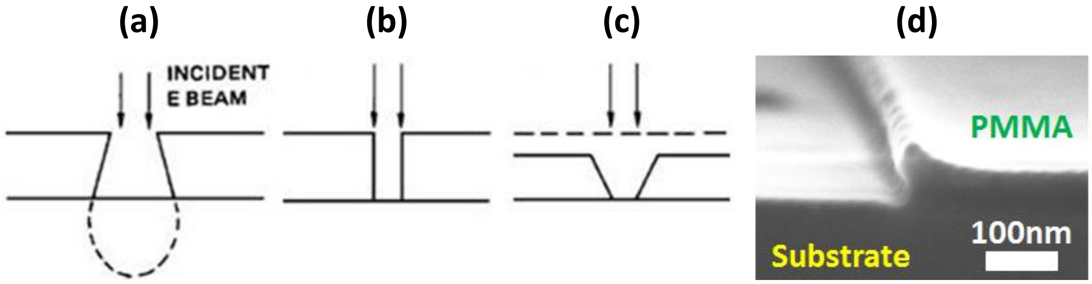

Figure 6. Edge profile in positive resist (a) high dose and short development time, (b) medium dose and development time, and (c) low dose and long development time (d) SEM image of undercut in double layer PMMA (495A2/950A2). (a), (b) and (c) taken from [133].

The edge slope and the metallization process essentially define the outcome of the lift-off process. A slope such as in Fig. 6 (a) and Fig. 6 (d) is commonly referred to as an undercut, and is often used to facilitate the lift-off. If it is so intended, an undercut is achieved by using a bi-layer of two PMMA resists with distinct molecular weights. The top layer consists of a polymer of larger molecular weight and the bottom layer consists of a polymer of lower molecular weight. The difference in molecular weight (and the fact that the bottom layer is closest to the substrate) will result in the bottom layer experiencing an increased exposure. This difference in exposure between the two layers results in the shadowing effect which can be seen in Fig. 6(d).

2.6.5 Deposition:

After the pattern has been engraved in the resist, we can proceed to deposit a desired material. The material deposition will define the properties of the film formed. For this thesis deposition was performed in high vacuum systems and involved techniques such as magnetron sputtering, evaporation (thermal and e-beam) and sublimation. Critical deposition parameters include the deposition rate, the substrate temperature, the directionality and the vacuum level. By tuning these, one can obtain a level of control over the resulting grain size, surface roughness, film density and edge quality. While a detailed presentation of each deposition method is beyond the scope of this thesis, we intend to showcase the effects of deposition parameters.

In Fig. 7 we see the effect of increasing the deposition rate on the surface roughness of a platinum (Pt) thin film, sputtered onto a SiO_2 surface. As we increase the deposition rate, the resulting Pt film becomes continually smoother (see Fig. 7(d)).

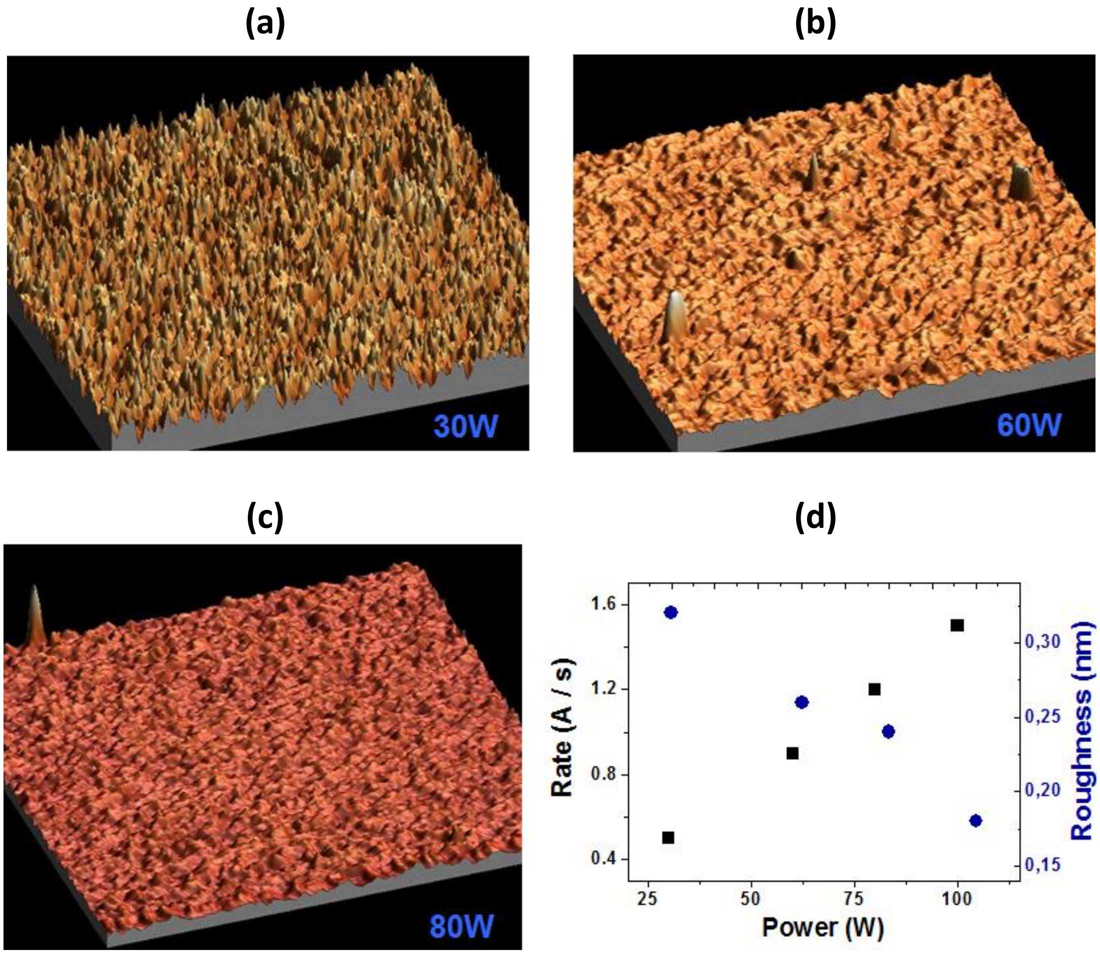

Figure 7. Deposition of Pt via sputtering. Increasing sputtering power increases the deposition rate and results in smoother surfaces. (a), (b) and (c) show AFM images of 10nm thick Pt films sputtered at 30W, 60W and 80W respectively. All other sputtering conditions were kept constant. (d) Plot of sputtering power versus deposition rate and surface roughness. We see that increasing the rate results in smoother surfaces.

The directionality of a deposition is largely related to the edges of the resulting structures. Deposition via the omni-directional magnetron sputtering or atomic layer deposition (ALD) techniques will have a higher chance of filling an undercut or covering the resist pattern’s walls. Depending on the material, this can result in distorted structures and unwanted vertical walls at the edges of the structure, commonly referred to as “horns”. Directional deposition techniques such as thermal or e-beam evaporation will have less chance of deposition in unwanted areas and will result in smoother edges.

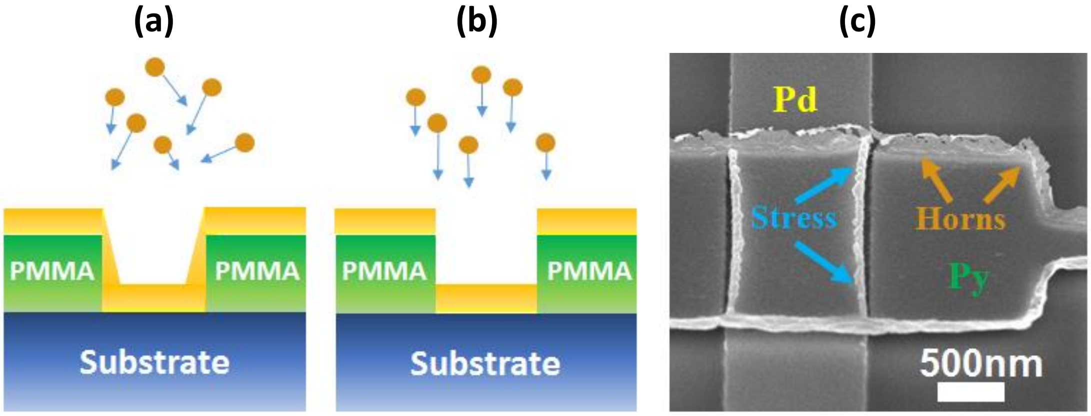

Figure 8. (a) Omni-directional deposition. Material is deposited on side-walls of resist. (b)Directional deposition. Material is deposited only in desired location. (c) SEM image of e-beam (directional) deposited Py structure with horns. (a) and (b) adapted from [125].

Fig. 8(c) shows a nickel-iron ($Ni_{80}Fe_{20}$, commonly permalloy, Py) structure which has been e-beam deposited (directionally) over a sputtered palladium (Pd) strip, laying on a SiO_2 surface. As can be seen, despite a directional deposition the Py forms large horns, whereas the omni-directional sputtered film does not. Clearly, this is contrary to what is expected and implies that the innate properties of the material in question can sometimes trump the effects of deposition parameters and dominate the formation of structures.

Another interesting feature of Fig. 8(c) is the discontinuity of the Py film at the edges of the Pd strip. Deposition of a material on an incompatible surface can lead to poor adhesion, roughness and even deformations due to excessive stress between the layers. Careful tuning of deposition parameters or even deposition of intermediate layers of other materials can sometimes improve the formation of the layers however sometimes the incompatibility of materials must be accepted as an unavoidable limitation on the design and fabrication of devices.

2.6.7 Lift-Off:

The final step of the EBL process is the lift-off. The lift-off involves the dissolution of the mask and the removal of the excess deposited material. This is usually achieved by submerging a sample into a resist stripper, i.e. a solvent which attacks and slowly dissolves the resist. Despite the grooves in the resist, the deposition usually results in a continuous film and for the excess material to be washed away the film has to be torn off at the structures edges. Clearly, this process will depend on the thickness of the resist, the thickness and strength of the material film deposited and the rate of resist dissolution.

Typical resist strippers are dichloromethane (CH_2Cl_2), dichloroethane ($C_2H_4Cl_2$), N-methylpyrrolidone (C_5H_9NO) and the most popular, acetone (C_3H_6O) [139]. The choice of stripper is based on the selectivity, the dissolution rate and the associated health risk. While some strippers can remove the resist very efficiently, they may sometimes attack the deposited materials making them incompatible for certain processes. Furthermore although strippers can be selective and have high dissolution rates if they present danger to one's health they can be very uncomfortable to work with frequently.

To promote lift-off certain measures can be taken. Primarily, we can ensure that the stripper has access to all areas which we wish to remove. Narrow strips of excess material tightly bound to surrounding structures will be hard to remove, as the stripper will be unable to access and dissolve the underlying resist. An empirical rule applied to this end is that the thickness of the resist layer is at least twice (ideally three times) that of the deposited material layer. This promotes the tearing of the material layer at the edges allowing the stripper to seep into the underlying resist layer and accelerate the dissolution. Secondly, increasing the temperature of the bath will accelerate the process however given that these solvents evaporate quickly, care must be taken to refill the bath when necessary and to not inhale any fumes. Finally, in certain cases lift-off can be assisted by ultra-sonic agitation which promotes the dissolution of the resist but also the dismantling of excess material. Although effective, this process is quite violent and is unsuitable for delicate structures. However, for robust devices it can be extremely useful as it can reduce the required lift-off time from hours to minutes.

During this thesis, the majority of lift-off processes were performed using acetone at ambient conditions. Depending on the materials deposited and the state of the resist (it can harden and become less soluble after several processing steps) at this stage, the lift-off method was varied between ambient acetone to warm dichloromethane and submersion times from 15min to entire days. When appropriate ultrasound agitation was used to accelerate the process, or assist the tearing of tightly bound excess metal.

PART B:

Pursuing sub-10nm Features

For the remainder of this chapter we will shift our attention to the pursuit of minimal device features. As mentioned above, a substantial aspect of our work called for the fabrication of metallic electrodes separated by nanometric gaps and hence we focus on this structure. At first, we look at pushing the limits of EBL. Then we present the Electromigration (EM) technique which by diminishing the dimensions of a metallic wire can create either a constricted region (see chapter 5) or nanogap electrodes (see chapters 3 and 4). Finally, we will present the Overhang method, which is applied to create large aspect ratio nanogaps.

2.7 Minimum EBL Features:

Obtaining sub-10nm resolution in EBL defined structures is only possible using certain geometries and requires tremendous control over the process [134]. However, the convenience of a one-step lithography process has inspired a considerable effort to be directed towards controlling the structure edges, improving the lift-off process and overcoming the proximity effect.

In terms of exposure, minimal features can be attempted by increasing the beam voltage and decreasing the resist thickness. However, even with minimal proximity effect, materialization of such structures can then only be done using thin metallic structures whose fragility can largely decrease the yield [140]. Although sub-5nm nanogaps by EBL have already been reported, their absence in relevant studies (single molecule, quantum dots, etc.) supports this claim and implies that reproducible fabrication of working devices is not trivial.

Like others before us, our approach to sub-10nm nanogaps by EBL involved acknowledging the unavoidable limits of control, and adjusting the design to obtain a geometry-specific optimization [125, 141]. We began by creating an array of rectangular electrodes with distinct widths and electrode separations. After each batch was examined we re-designed the array to optimize the outcome. Electrodes were fabricated simultaneously, in pairs whose separation varied between 5nm and 120nm. After lift-off, scanning electron microscopy (SEM) was used to determine the difference between the designed separation and the one obtained. In this way, we were able to account for the proximity effect and optimize our initial design. Finally, for the sub-10nm gaps obtained since the resolution of the SEM is less than 10nm electrical measurements were used to determine the *channel resistance* so as to understand weather we had obtained a short circuit, a tunnel junction or an open circuit.

In an attempt to further optimize the resolution, this process was repeated for a variety of fabrication parameters. Typically, we used thin resist layers (between 30nm and 150nm) to help the exposure and thin metallic layers (between 6nm and 30nm) to facilitate the lift off. Beam voltages of 10kV and 20kV where used and the dose was varied by about ±25% of the known clearing dose for each case. To avoid angle irreproducibility during deposition we chose to deposit platinum (Pt) and palladium (Pd) layers via Magnetron Sputtering. Lift-off was carried out in acetone, and in the case of wide Pt electrodes (robust enough) assisted by US.

Using this method, we were able to optimize the EBL process for given electrode shapes. Optimum results were obtained using a 50nm thick resist layer of 950A2 PMMA, spun at 5000rpm and baked at 190°C for 1 minute. Using a beam voltage of 10kV the optimum dose was 130μC/cm^2 while using 20kV the dose required to be increased to 320μC/cm^2. Although 20kV achieved noticeably shaper large-aspect-ratio structures, it did not increase the yield of sub-10nm nanogaps as compared to 10kV beam exposure.

The length of the electrodes was kept constant at 5μm while the width was varied between 50nm and 110nm. As expected, we found that the proximity effect increased for wider electrodes and each width gave optimum results for a distinct electrode separation. In this range, we found that initial separation of less than 10nm results in a short circuit and that initial separation of more than 30nm results in an open circuit. The optimum designed separation varied from 14nm for 50nm wide electrodes to 20 nm for 110nm wide electrodes. Using this method, while sub-15nm gaps can be achieved quite readily, the yield for working tunnel junction devices is less than 10%.

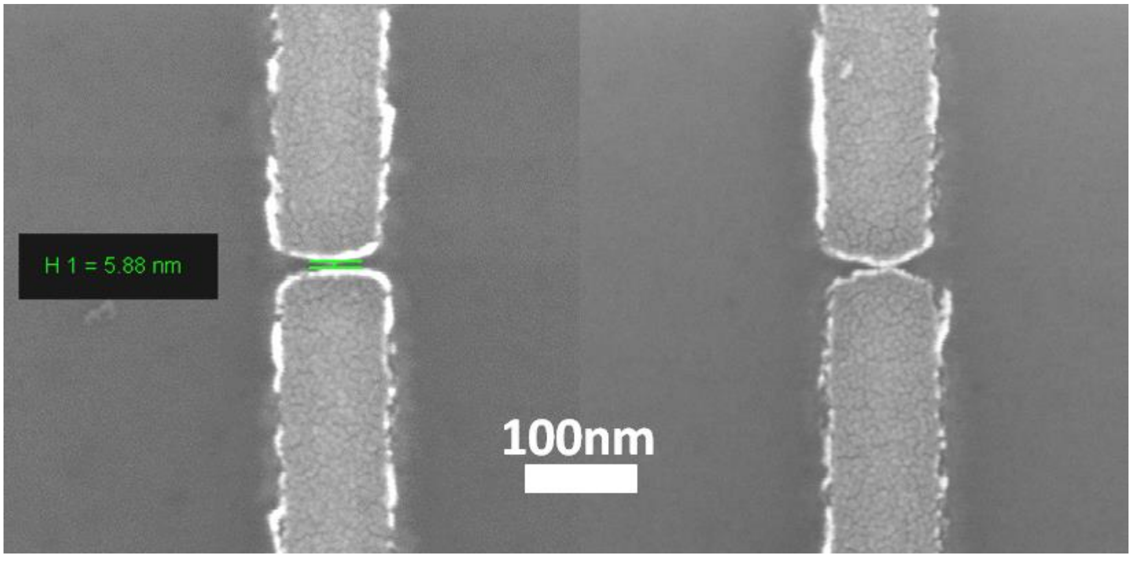

Figure 9. Two EBL nanogaps fabricated with the exact same processing condition and resulting in slightly different gaps

In Fig. 9 we see two nanogaps fabricated with the exact same design and processing conditions. Typically, the resulting electrode separation of identical devices was found to vary by approximately ±5nm which for many devices (eg. tunnel junctions) reflects unacceptable reproducibility. At this stage, the invariability of the yield of tunneling devices to the process parameters led us to believe that nanometric control of the fabrication is limited around 10nm and although further optimization could be attempted, it was decided to explore alternative methods of fabrication instead.

2.8 Electromigration:

2.8.1 Introduction:

The electromigration technique makes use of a large current density to cause the atoms of a metal to reallocate (migrate) to nearby locations. Although initially discovered as a failure mechanism of wire interconnects, in the last couple of decades it has been found to be a unique fabrication method, for creating nanogap electrodes [142, 143, 144, 145, 146]. Due to the nature of the process, the resulting shape of the electrode is often random, but for purposes such as single molecular, quantum dot, ballistic and tunneling transport systems it offers a unique platform for research [147, 143, 148].

EM is a form of mass transport caused by the exchange of momentum between metal ions and conducting electrons [149, 150]. When applying an electric field to a conductor, electrons start to move according to the potential gradient. This gush of electrons is often referred to as electron wind and if it is energetic enough it can result in the activation of metal ions, allowing them to escape their potential wells and be free to move through the metal lattice. These activated atoms are positively charged and will experience a force of opposite direction to that of the electron wind. On the other hand, the flowing electrons will collide with the activated atoms, forcing them along the path of the electron wind. Despite the predominant force being that of the electron wind [150], the resulting displacement of the activated metal ions will ultimately depend on the interplay of these two forces.

Given that EM was initially treated as a problem, the most common parameter for characterizing the EM process is the median time to failure (MTF) developed by Black [149-151].

$$MTF = \frac{A}{j^n} e^{\left(\frac{E_a}{k_B T}\right)} \tag{4}$$

where A is a constant, j is the current density, n is usually between 1 and 3 depending on the experiment [152], E_a is the activation energy, k_B is Boltzmann's constant and T is the temperature. The constant A embodies several physical parameters including the cross sectional area, the volume resistivity of the metal and the mean free path [150].

Unfortunately failure is a fairly vague term, but is often considered to be a certain percentage increase (10% - 20%) in resistance [152].

Black's Law implies that EM failure could occur in a range of current densities resulting in a range of times taken to fail. Clearly temperature and thermal conductivity are key parameters [153] in this process. The critical current density J_c is the one needed to bring about EM and for most metals is approximately 10^{12} A/m^2 which implies a great amount of Joule heating [153, 152]. Depending on the design, during EM metals can locally reach temperatures greater than 400^{o}C [154, 155], making the method unsuitable for certain applications.

During EM, diffusion of metallic atoms can occur via three paths: the lattice, the grain boundaries and the surface. Generally lattice diffusion is the slowest pathway and hence has the largest activation energy. Similarly, surface diffusion has the lwest activation energy ($E_a^{lattice}>E_a^{grain\ boundary}>E_a^{surface}$) [156]. The dominant diffusion path during EM will depend on the crystalline and grain structure present which is ultimately influenced by the type of material and the fabrication process. Although surface diffusion is often thought to dominate during EM, the large dispersion in reported activation energies implies that the mechanism is most probably specific to the wire involved [156, 146].

Characterization of the resulting structures is done both electrically and via microscopy. The electrical transport can be measured at different temperatures and the Si substrate can be used as a gate electrode to reveal specific conductance features. SEM allows the visualization and quantification of the resulting device dimensions but can only be done at room temperature, after the measurement. Electrical characterization is generally considered to be more relevant but SEM gives access to information which cannot be otherwise achieved, such as grain structure and heating effects (eg. metling).

2.8.2 Performing Electromigration:

For this thesis, EM was performed in gold (Au), copper (Cu) and nickel-iron alloy ($Ni_{80}Fe_{20}$, commonly called permalloy, Py) nanowires. Nominal wire dimensions were 130nm wide and 30nm thick. The length of the wires varied between 500nm and 4µm. EM was applied to obtain nanogaps, single-eletron transistors (SET) and in some cases simply to cause a local increase in resistance (see chapter 5). Despite its violent nature, a certain level of control can be achieved making it a uniquely useful technique.

Given the limitations of conventional fabrication techniques, nanogaps created by EM are quite common [157-159] and in this context are referred to as electrical break junctions. Despite the mechanism being the same, there are several ways of applying the EM technique [147, 142, 157, 160, 161]. In our case we use a multistep feedback-controlled method. Although EM has been performed successfully at room temperature the majority of our devices, where electromigrated either at 2K or 10K as this was usually the range in which we wished to measure the resulting devices.

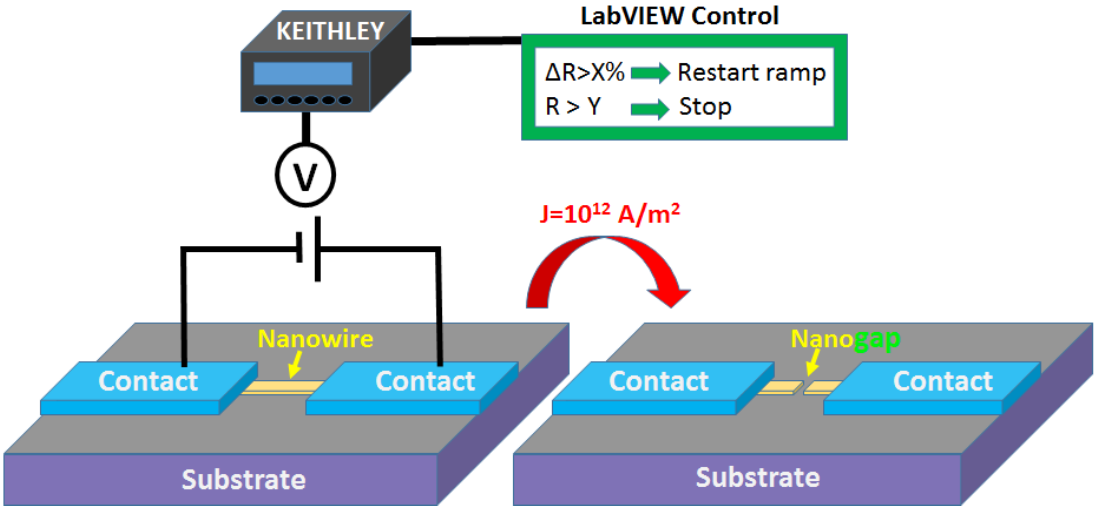

Figure 10. Schematic of EM process. A voltage source applies an increasing voltage to the nanowire in a 2-point configuration. Once the critical current density is reached EM takes place and the resistance increases abruptly. The increase in resistance resets the ramp via the feedback mechanism

To increase control over the process the voltage ramps are subject to feedback conditions applied via a LabVIEW interface. The voltage is increased in steps of 0.4mV and progressively calculates the resistance change (ΔR) for every 40 ramp points (16mV) as a percentage of the average resistance of these points. The voltage is reset to its initial value if ΔR exceeds a given value. For most cases we set this value to 1.5%, but the value can be actively changed during the EM process to whatever value is needed. Furthermore, the program will automatically stop applying voltage if the resistance exceeds a pre-set value. For the purpose of this work we refer to a permanent increase in the wire resistance as an EM step.

The gradual multi-step EM allows us to access different stages of the EM process. The first ramp is always distinguishable presenting a momentary negative slope and quite often resulting in a slight decrease of the resistance. This does not reflect EM, but a type of initial change required to proceed with the process.

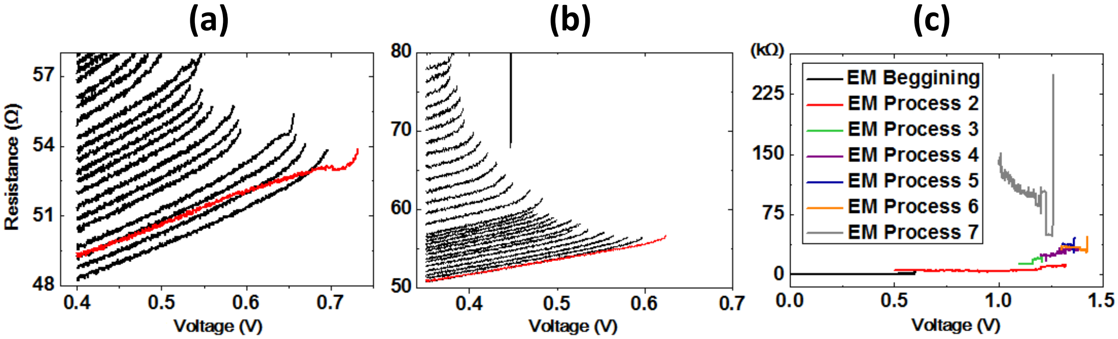

Figure 11. EM ramps of Au and Cu nanowires. (a) First EM ramp highlighted in red. (b) Controllable EM regime (c) High resistance regime.

The second stage is that of controllable EM. In this regime, by adjusting the feedback parameter ΔR, we are able to control the rate of EM with high precision. During this stage, the wire appears to have almost constant critical current density [158]. This concept depicts the wire undergoing a constant reduction of its cross sectional area. Every time the cross section is decreased, the wire will require less current to further the breaking. This can be seen in Fig. 11(b) where each ramp is broken at a slightly lower voltage compared to the one preceding it.

Note also that in Fig. 11(b) there are two subsets of ramps, one being at lower resistance and closely stacked together and the other being at larger resistances and appearing more scarcely. These two subsets demonstrate the control that can be obtained using feedback. Each subset corresponds to a distinct ΔR feedback condition which when tuned can be used to dynamically control the amount of EM that will occur in each ramp. Although a faster EM rate may often be tempting, increasing ΔR makes the process more violent and increases the risk of explosive EM. For the majority of our processes, we were unable to increase ΔR to over 5% while maintaining control. The exact limit however, is case specific, depending on the resistance, geometry, substrate and material properties.

Finally when this condition is exhausted we arrive at the 3rd regime, where the breaking becomes unpredictable. Feedback conditions are made more lenient and are enforced only to prevent the wire from completely exploding as smooth changes in resistance are replaced by abrupt jumps. In this regime, no real control over the result is viable. Nevertheless, although the resulting resistance is unpredictable, the order of magnitude is not and often a gradual increase can be achieved from 10^3 Ω to 10^8 Ω.

For certain materials, such as Au, nanowires broken to a resistance of several kΩ (3rd regime) are in a metastable state. This implies that over time, their resistance can either decrease or increase reaching even the MΩ range without any further stimulus [161, 160]. This technique is known as self-breaking.

2.8.3 EM Characterization:

From the EM ramps, we extract the breaking voltage and using Ohm's Law we calculate the critical current:

$$V_b = I_C R = J_C A \frac{\rho L}{A} = J_C \rho L \tag{5}$$

where V_b is the breaking voltage, I_c is the critical current, R is resistance, J_c is the critical current density, A is cross sectional area, ρ is resistivity and L is length. The cross sectional area is calculated using the thickness and width of the wire as extracted from X-Ray Reflectivity (XRR) measurements and SEM images respectively. Dividing the current by the cross section we obtain the current density.

A generally accepted concept is that larger breaking voltages give rise to more violent EM [142, 146]. With this in mind it is reasonable to assume that control over EM can be achieved by lowering the breaking voltage. As mentioned, the breaking voltage is the product of the series resistance and the critical current. This implies that the series resistance and the critical current density can be used to tune the breaking voltage and obtain a softer EM process. The critical current density is a property of the material and little can be done to adjust it. However altering the deposition parameters and the thermal conductivity of its surroundings is expected to have a significant effect on J_c [153, 154]. In fact, passivation of nanowires has been shown to dramatically alter the failure times [162].

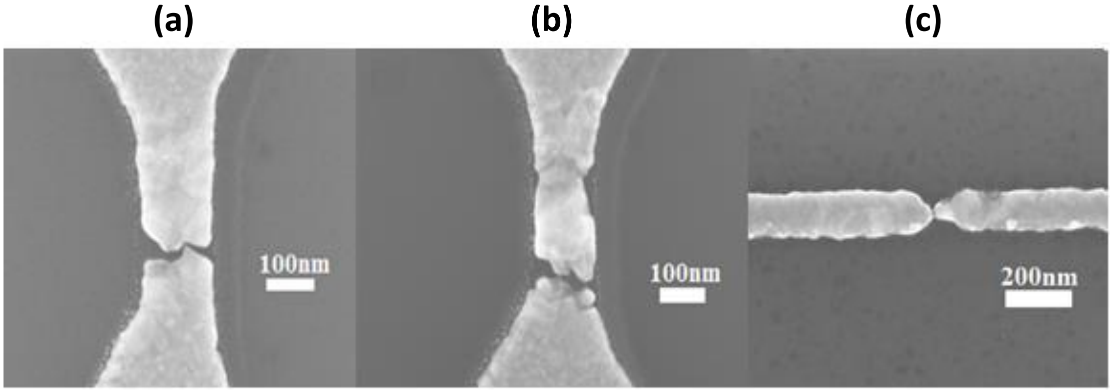

Figure 12. EM of nanowires. (a) EM resulting in single nanogap. (b) EM resulting in two parallel conductive channels. (c) EM of wire with spatial constriction.

The resulting gap size is believed to be proportional to the breaking voltage and hence to the total device resistance [142, 146, 161]. Optimization of the process for a specific wire can result in reproducible nanogap formation, with gap sizes between 1nm and 5nm corresponding to a resistance between 10kΩ and 100GΩ [146, 158, 161]. However, although some control can be obtained, for the majority of devices the resulting size and geometry of the electrodes remains largely uncontrollable [78]. Spatial constrictions can be incorporated in the wire to locally increase the current density and select the location in which EM takes place however in such schemes calculating the critical current density becomes severely more complicated.

Material	Resistance (Ω)	J_c (10^{12} A/m^2)
Gold (Au)	50	4
Copper (Cu)	150	2.5
Copper (Cu)	500	1.6
Permalloy (Py)	450	0.9

Table 1. Critical current densities extracted from EM ramps. Larger resistance seems to imply lower critical current densities.

In Table 1 we see the average J_c values extracted from a variety of devices made during this thesis. The tabulated resistance is the one measured at the beginning of the first voltage ramp (at 400mV) and is the series resistance of the nanowire and the large-scale contacts (2-point resistance). The calculated critical current densities are similar to ones obtained in literature [152, 156, 146].

As the cross section is continually diminished, electron transport in our nanowires enter the quasi-ballistic regime. Measuring the current as a function of voltage (I(V)) we see a deviation from the linear Ohmic behavior indicating that our device dimensions are approaching the non-linear transport regime [50, 163, 146].

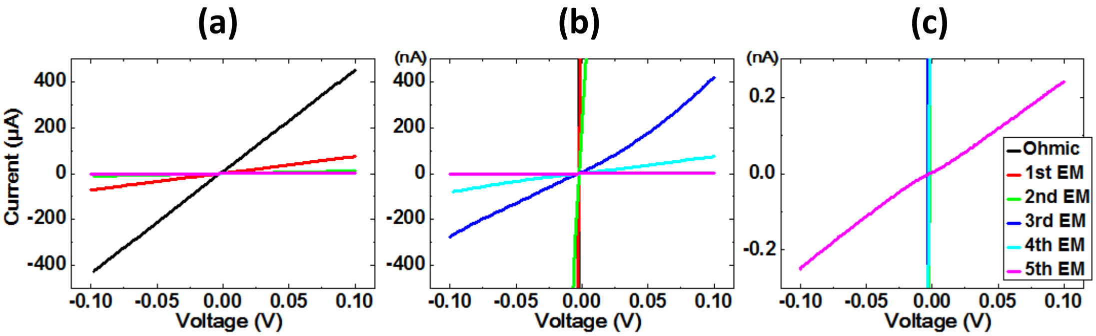

Figure 13. I(V) curves at various EM steps. During EM we see the transition from Ohmic (a) to non-linear (c) behavior.

The uniqueness of the EM technique is that it allows access to a variety of transport regimes by changing the geometry of a single wire. Due to its nature, the technique often results in various interesting conductive channels forming across the electrodes, such as metal particle quantum dots, clean tunnel junctions, and ballistic conductance channels [147, 159, 164].

2.9 Overhang Method:

2.9.1 Introduction:

The overhang method was developed by J. Tang et al. [165] and although it is more labor-intensive than EBL and EM, it offers the opportunity to create large aspect ratio gaps of essentially any shape. Although the method was meant to create 10-20nm gaps [165-167] with very high yield, sub-10nm gaps are possible. Using this method nanogap electrodes have been used to probe single molecules and metallic nanoparticles [168, 169].

The method requires two electrodes to be defined in independent EBL steps. The first electrode (Fig.14 (a)), consists of a metallic bilayer whose top layer is a readily oxidizing metal (Cr, Ti, Al, Cu etc.). After lift-off, the top layer oxidizes either naturally (exposure to air) or artificially (O_2 or H_2O environment) causing it to slightly swell (Fig.14 (b)). While the bottom layer remains unchanged, the swelling of the top layer causes it to grow to a slightly larger size causing a shadow over the entire border of the underlying electrode.

The second electrode is then patterned to overlap the bilayer (Fig.14 (c)). Due to the swelling of the top layer, the two electrodes will be separated by a gap. Finally the device undergoes a wet chemical etch which is used to remove the oxidized layer along with the overlapping section of the second electrode (Fig.14 (d)). The result is two electrodes, separated by a nanometric gap.

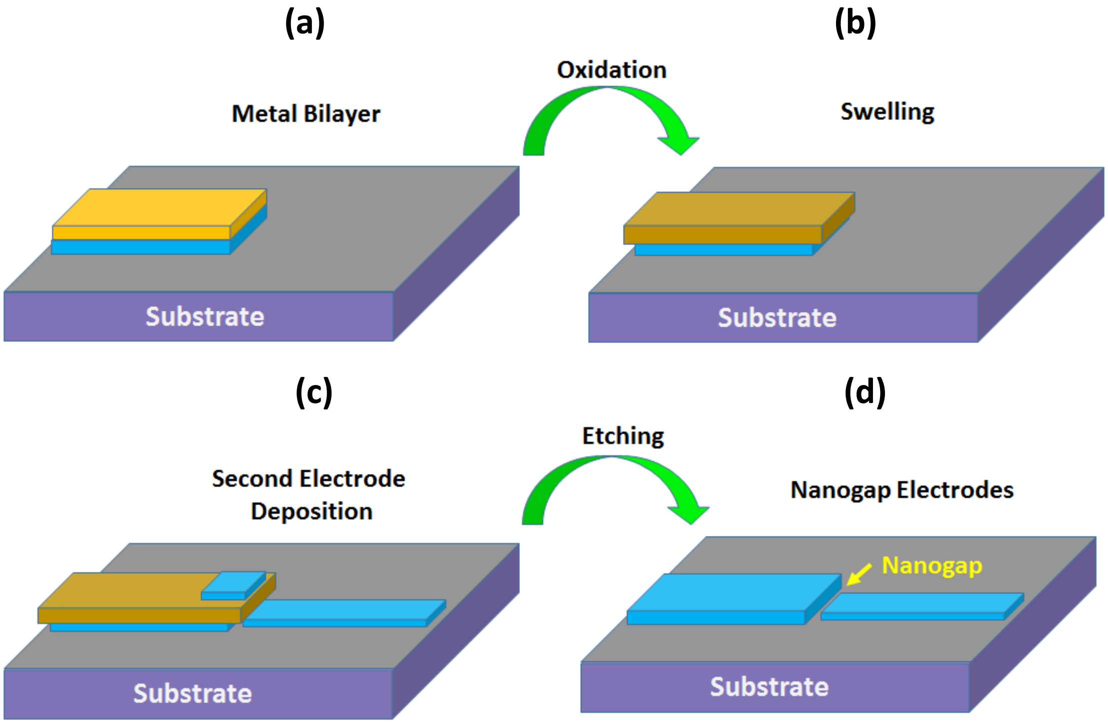

Figure 14. Process steps of the Overhang method. (a) Deposition and lift-off of metal bilayer. (b) Oxidation and swelling of top layer. (c) Second electrode is defined to overlap the bilayer. (d) Wet etching removes the top of the bilayer and the overlapping part of the second electrode exposing the nanogap.

Although this method offers easy alignment, good yield and theoretically any aspect ratio, it is the most complicated method of fabrication applied in this thesis. Here the directionality of the deposition, the etching selectivity and the uniformity and roughness of the bilayer edges are of great significance to the outcome.

Depending on the choice of materials there are distinct recipes which have been developed throughout this work. Initially we developed a recipe using titanium (Ti) or aluminum (Al) oxidizing layers which were etched in a solution of sulfuric acid (H_2SO_4) and hydrogen peroxide (H_2O_2), commonly known as acidic Piranha Solution. Then we explored using chromium (Cr) as the oxidizing layer and the ceric ammonium nitrate ($H_8N_8CeO_{18}$) based standard Chromium Etchant (Sigma-Aldrich) which appeared to be a much more attractive choice. The etch selectivity is of paramount importance since even the slightest etching of the electrode layers, results in significantly larger gaps. In the following sections we will discuss the design and fabrication strategies implicated to apply the Overhang method. For this discussion, many of the relevant technical details have been covered in section 2.6 and hence will not be explained here.

2.9.2 Design Considerations:

One of the most important and challenging requirements for this method is to control the sharpness of the metallic bilayer edges. Desirable bilayer edges present a vertical profile allowing the resulting electrode separation to depend mainly on the oxidation of the top layer. Given that sloped profiles are inherent to resist lithography, this is not a trivial task. A near-vertical resist profile is normally achieved in thin resists and since the resist thickness limits the amount of metal that can be deposited a trade-off emerges between the resist edge slope and the bilayer thickness. Furthermore to promote vertical bilayer profiles, the material deposition should be done directionally, with minimal deposition on the resist sidewalls and without breaking vacuum. In fact, the development of this method by Tang et al. was first applied using sub-5nm thick Pt electrodes.

Another important aspect of the process is the selectivity of the etching process for the top layer of the bimetal. The etching process must remove the excess material while leaving the electrodes, the substrate and any adhesive layers applied (eg. Ti for Au electrodes) unaffected. Given that the second electrode is defined by a lift-off mechanism during the etching process, the relative thicknesses of the bilayer and the second electrode must facilitate the lift-off process. Finally, since thicker oxidizing layers result in larger oxide shadows, a trade-off is presented between efficient removal of the overlapping metal and small gap size.

Thinner electrodes appear to solve two problems at once; the need for thin resist layer to achieve vertical profile and the need for thin oxidizing layer to achieve a small gap. Thick electrodes however are more robust and respond better to the multitude of process steps required. Optimization of the design will therefore be material and geometry specific depending on the amount of oxidation, and the ease of material lift-off.

For our devices, it was decided to work with natural oxidation. Attempts of using artificial oxidation seemed to complicate the process without any particular benefit and were quickly abandoned. The majority of the samples were left to oxidize in the nanoGUNE cleanroom for at least one day before applying resist for the second EBL step.

For Cr and Al, native oxide layers formed at ambient conditions are expected to grow to about 2nm-5nm thick [170-172]. Similarly, ambient oxidation of Ti will create a 5nm-10nm thick layer [173]. Devices where made using Ti, Al and Cr as oxidizing layers and as expected, while employing the same thickness, devices using Ti resulted in the largest gap sizes.

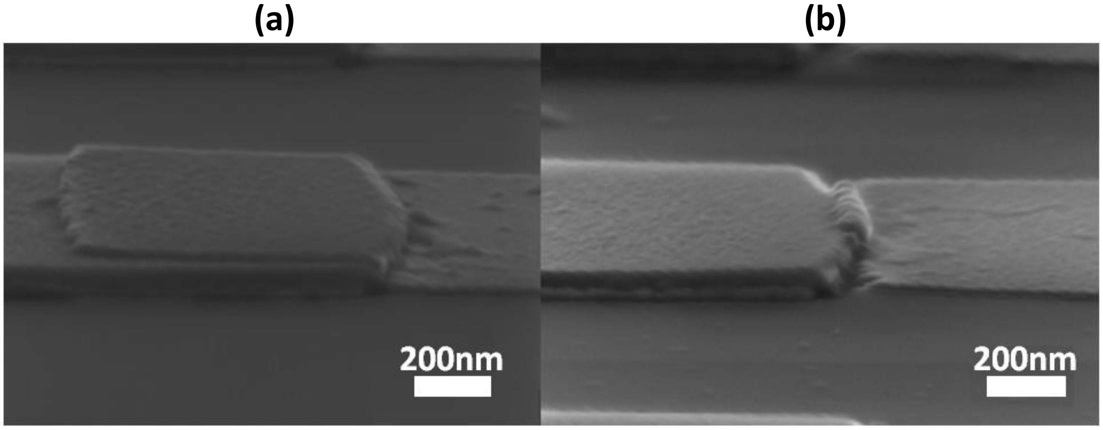

Figure 15. Bilayer (left) and overlapping electrode (right) before etching. (a)Large Overlap. (b)Small Overlap.

In addition to the amount of oxidation, the thickness of the oxidizing layer also affects the gap size. Effects of angle deposition could result in thickness dependent gap size, although under strict fabrication control and using specific design parameters (homogeneous, straight edges, oriented in same direction) the effect has been previously ruled out [166, 167]. Oxidation is usually caused by diffusion of metal cations and oxygen anions to and from the metal surface respectively. As the oxide is formed the oxidation rate decreases due to the increasing oxide thickness acting as a strong diffusion barrier [174]. Fursina et al. [166] suggest that extra oxidation can occur in subsequent high temperature fabrication steps, such as resist baking or thermal evaporation for the second electrode. In addition, they claim that for Cr oxidizing layers, stresses created in the metal/oxide interface may cause a deformation of the metal layer which would favor larger gap size and would increase with the oxidizing layer´s thickness. Despite these being viable possibilities, no clear evidence has been presented. In our devices increased gap size due to larger thickness has been attributed both to excess oxidation and to angle effects.

Using the same thickness, we see that Ti results in significantly larger gaps demonstrating the importance of oxidation. Given that we are using ambient oxidation, the increase of oxide thickness with layer thickness should be negligible. However we often observe a scaling of the conductivity with the orientation of the shadow on the substrate, implying that angle deposition effects are present.

Directional evaporation is often not entirely directional. It is quite well known that evaporated metal atoms either via e-beam or via thermal evaporation are driven towards the substrate in a conical shape and even if the substrate is entirely perpendicular to the cone center, unless it is exactly at the center of the cone, incoming metal atoms will arrive at an angle. Furthermore, although the effect is not very large, it is quite possible that while fixing the substrate in position, it is placed with a slight tilt with respect to the substrate holder. Hence, angle effects can arise both from tilted substrates and from the conical deposition profile. As illustrated in Fig. 16 (a) and Fig. 16 (b), the orientation of a shadow can result in distinct gap sizes.

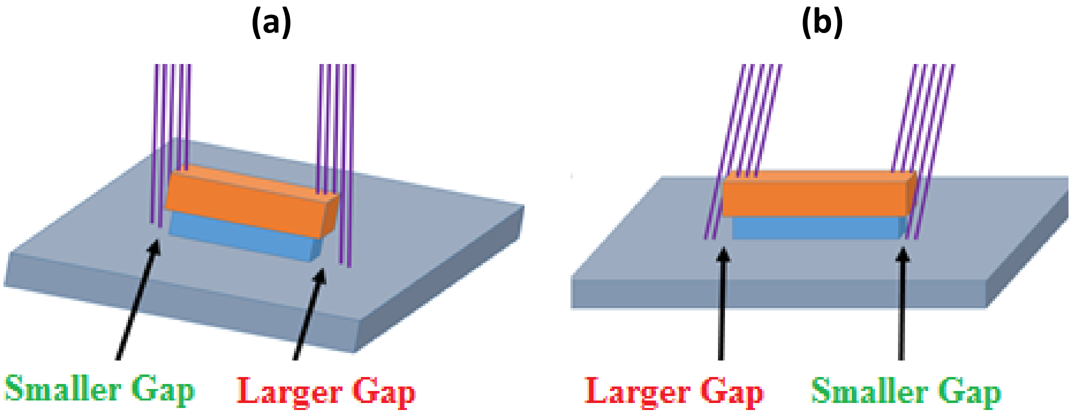

Figure 16. (a) The substrate is tilted and not perpendicular to the incoming metal atoms. (b) The incoming atoms arrive at an angle causing the resulting shadow to increase or decrease respectively

From these illustrations, we can also see that increasing the thickness of the oxidizing layer would result in augmenting the larger gaps and have no effect on the smaller ones. To avoid orientation-dependent shadowing effects the metal deposition can be performed while rotating the sample but as we found, this method significantly increases the risk of short-circuiting the two electrodes.

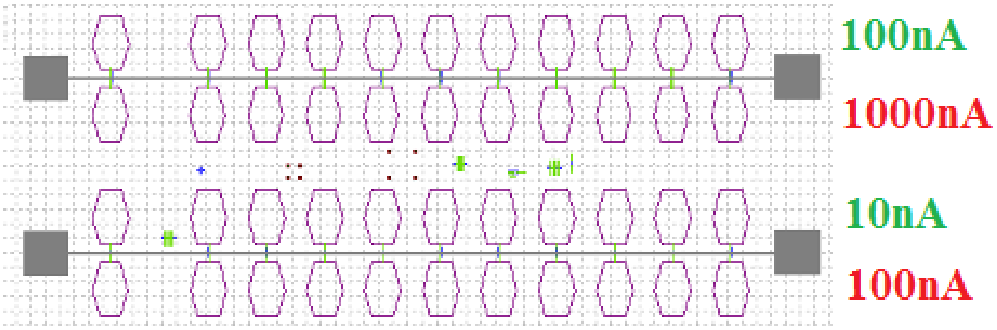

Figure 17. Design of sample fabricated using the overhang method. Current scales (for fixed bias) with the location on the substrate and the orientation of the shadow indicating large angle effects on the resulting gap size.

In Fig. 17 we see the design of an array of gaps made using this method. The gray lines represent metallic bilayers and serve as a common electrode to distinct individual gaps. The purple pads and small lines going towards the bilayers represent the *secondary electrodes*, i.e those deposited after oxidation. Each bilayer accommodates devices of given aspect ratios; the top bilayer having aspect ratios larger than 100:1 and the bottom bilayer having aspect ratios smaller than 100:1. In each bilayer, the top and bottom rows have the same geometry. We see that, although the rows of each bilayer accommodate identical devices, the top rows give rise to nanogaps, which are an order of magnitude less conductive than the top rows. Given that the devices are identical by design, the only explanation for this difference is the effect of an angled deposition.

As mentioned earlier, the thickness of the oxidizing layer determines the ease of lift-off. Similar to the dissolution of PMMA described earlier, when the oxidizing layer is etched, it dissolves and the excess metal on it rips off exposing the nanogap. While this is essentially a lift-off process, in this case both the material dissolved and the excess material are present in considerably smaller quantities and the appropriate quantities depend on the geometry of the electrodes. Here, the ability to *lift-off* the excess metal is determined by the discontinuity between the bilayer and the secondary electrode. While a thicker oxide layer would facilitate this process, it would inadvertently cause an increase in the size of the gaps. The lift-off process is therefore highly geometry dependent. Applying the method on a multitude of designs allowed us to ascertain that maximizing the overlapping area while minimizing the border size gives optimum results for this method. Finally, contamination of the electrodes from SEM imaging was found to largely impede the etching process. Although this phenomenon is not understood it has been frequently observed and care must be taken, to not use devices that have been imaged prior to etching.

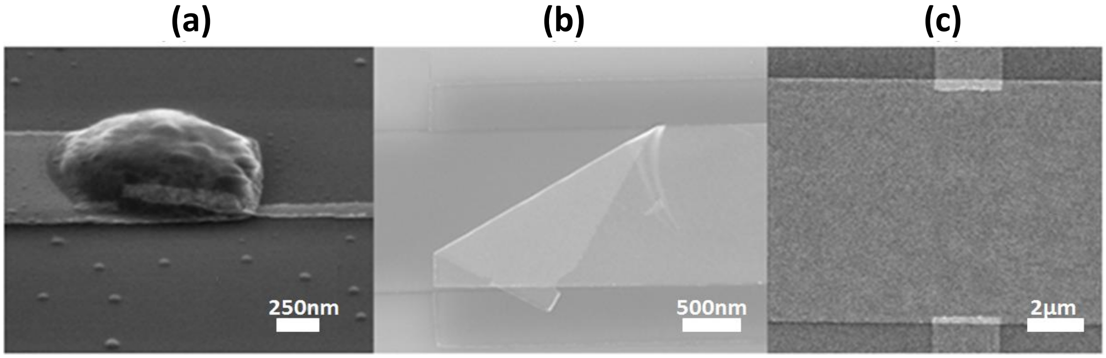

Figure 18. Failed lift-off. (a)Residues of the etch left under the overlapping metal. The edges did not allow the excess metal to rip off. (b) Excess metal ripping off in interdigitated design. The large border requires a large amount of ripping which impedes the removal of excess material. (c) Failed lift-off. Excess material is removed but rip occurred over bilayer.

2.9.3 Etching:

Each combination of materials requires a distinct etching recipe. The etching is done by submerging the entire chip in a beaker filled with the appropriate solution. To etch Ti and Al, we developed a recipe using acidic Piranha solution, which is a mixture of H_2SO_4 and H_2O_2. Mixing the two components creates an exothermic reaction, releasing enough heat to bring the solutions temperature above 100^o C. The exothermic reaction of the two components causes a rapid increase in the temperature of the solution, the value of which depends on the relative volumes of the two components and the rate of mixing. In addition, the solution loses its properties over time and the etching rate varies significantly. As a result, the Piranha Solution must be freshly prepared for each etch and control of the process requires care.

A variety of concentrations and temperatures were tested for the process, and the best results were obtained with 2:1, H_2SO_4:H_2O_2 concentration at a temperature of 55^oC. To increase reproducibility after mixing, the solution was left to cool down for about 15 minutes and then reheated on a hotplate. Given that the hotplate temperature was different from that of the solution, a thermometer was placed in the solution to directly monitor the real temperature. Depending on the state of the solution, the temperature could vary by approximately ±15^oC and hence to maintain a constant solution temperature, the hotplate temperature had to be dynamically adjusted. Using this recipe, although the etching requires several minutes, the lift-off of the overlap requires close to one hour in the solution. The process is stopped by placing the chip in H_2O. Ultrasonic agitation can be applied to assist the lift-off but can radically change (increase) the temperature and etching rate making the process less controllable.

The Cr etchant is a Cerium (Ce) based solution which is dramatically simpler to use and much more reproducible. The etchant is bought from Sigma Aldrich and the process is carried out at room temperature. Although the etching rate is significantly faster, the time required for lift-off is again much larger needing about one hour. For larger and more robust structures application of ultra-sonic agitation assists the process significantly.

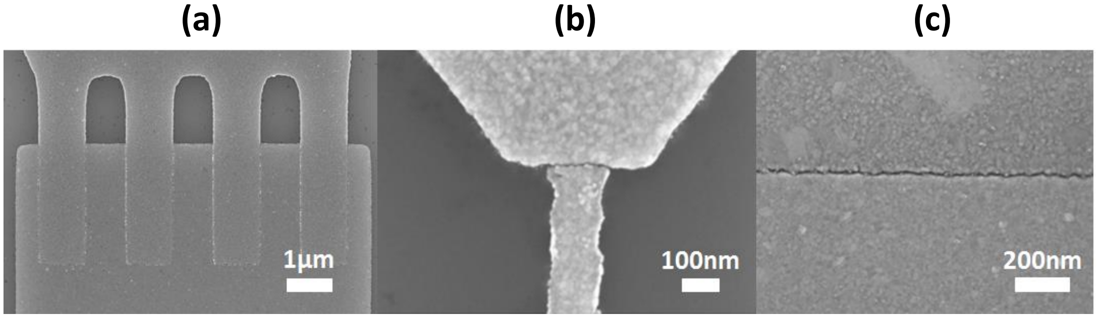

Figure 19. Devices made using Overhang Method. (a) Interdigitated electrodes (b) Low aspect ratio electrodes (c) Large aspect ratio electrodes

The inherent limitations of this method are induced by the oxide roughness and the lift-off of the overlapping metal. The oxide layer grown will have a certain roughness which will be transmitted to the secondary electrode via the oxides shadow. Just like in the case of EBL gaps, the exact geometry of the resulting gap will depend on the lift-off process and will almost certainly be inhomogeneous.

Due to the self-alignment of the two electrodes, this is a powerful method, offering a unique advantage over the ones previously presented. Self-alignment allows essentially any shape to be given to the gap as well as gaps of enormous aspect ratios.

Unfortunately, given the inherent roughness of the electrode edges, increasing the aspect ratio implies increasing the chance of shorting the two electrodes. This said, using this method lateral tunnel junctions 20μm long can be achieve quite readily. In addition, the cleanliness of the gap is similar to other methods, and using this method, we have also been able to probe trapped residue conducting nanoparticles.

Chapter 3

Device Characterization

3.1 Introduction:

In Chapter 2, we looked at three fabrication methods for creating Lateral Tunnel Junctions (LTJ). We have seen that no matter the method applied, precisely defining such structures is very challenging. Consequently, characterization of such devices must be done with care. At this scale, Scanning Electron Microscopy (SEM) cannot determine the geometrical details of the resulting structures accurately and the contamination it causes to the device surface can largely affect the resulting conductivity [175]. On the other hand, electrical characterization is non-invasive and can be used to extract a plethora of useful information.

This chapter focuses on electrical characterization of nanostructures. Firstly we present the instrumentation and methodology used to perform electrical measurements during this thesis. Then we present charge transport measurements of LTJs created by the techniques displayed in chapter 2. The electrical measurements are then fitted to tunneling theory, and analysis of the results is used to further the device characterization. With this method we are able to explore the uniformity and robustness of the tunnel junctions and visualize the energetic tunneling barrier.

The nature of nanoscale devices invites measurements in vacuum, at low temperatures and applying low voltages [169, 176]. By analyzing low temperature measurements of lateral tunnel junctions, we create a juxtaposition between the possible behaviors of the energetic barrier. In this way, and in accordance with other work [177-179], we find that fitting to tunneling theory is not a fully reliable characterization method. Nevertheless, the simplicity and non-invasiveness are very appealing and with care it can be a very powerful method of characterization.

Finally, we extend our characterization to nanogaps which contain conductive nanoparticles. We show that such devices can offer a unique opportunity to study single electron transport phenomena.

3.2 Electrical Characterization:

In this section we present the equipment and the set-up used for electrical characterization. Electrical measurements were performed using a Probe Station by Lakeshore and a Physical Parameter Measurement System (PPMS) by Quantum Design. Depending on the desired vacuum and temperature conditions, one was preferable to the other. For signal manipulation, we used a 2636 Source Meter, a 6221 Current Source, a 2182 Nanovoltmeter and a 4200 Parameter Analyzer all of which were made by KEITHLEY. Control over electrical measurement parameters but also temperature and magnetic field were obtained via Labview programs, custom-made for each type of measurement.

Contact to the sample is made manually, either by cold Indium (In) pressing or by direct contact of a probe tip to the device's macroscopic contacts. Typically, devices with sub-100nm features are very fragile and during contact can be damaged by static discharges. To prevent this from happening contacting such samples is always done while wearing grounding bracelets and during characterization the signal sources are grounded after each measurement cycle.

3.2.1 Probe Station:

The probe station allows measurement in a temperature range between 5K and 300K and a pressure of less than 10^{-5} mbar at room temperature. Its chamber is shielded from radiation and contains four probes which can be moved at will by micrometric actuators allowing in situ reconfiguration of the contacts. In addition, the sample stage can be rotated by 90 degrees and a magnetic field of up to 0.6T can be applied along its horizontal axis.

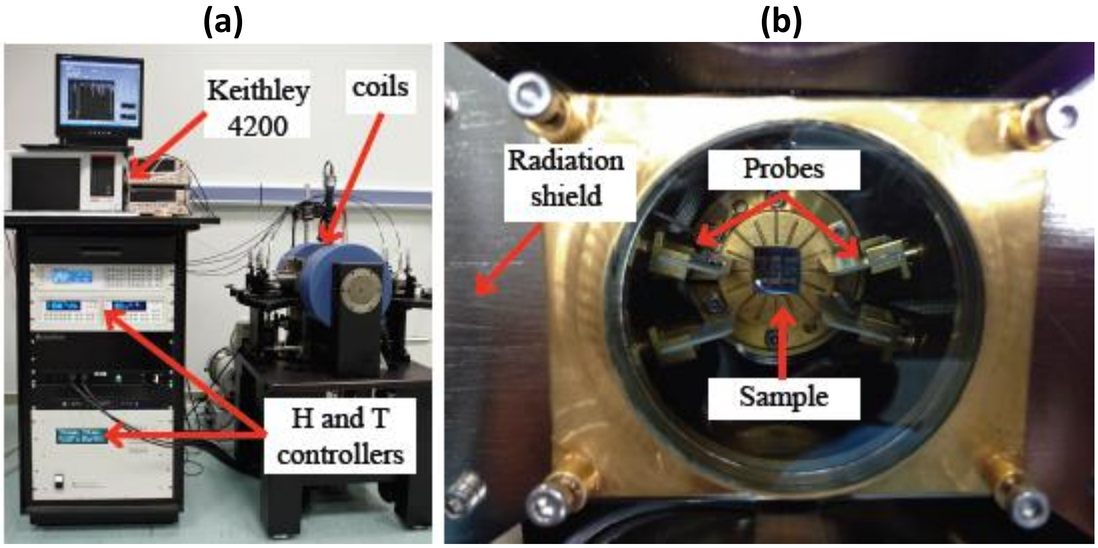

Figure 1. Probe Station Measurement Equipment. Adapted from [180]

The probe station was mostly used with the KEITHLEY 4200, which contains three source measurement units (SMU). The radiation shield, tri-axial cabling and the ultra-high SMU resolution of this setup allows a nominal sub-fA measurement resolution. Unfortunately, mechanical noise is introduced into the system raising this level significantly. This noise is mainly due to the poor contact between the probe tip and the thin contact pads of our devices. Additional noise is introduced when cooling down the sample stage as the helium compressor relays mechanical vibrations throughout the system. The contact between the tip and the sample can be improved by cold pressing pieces of In wire on the contacts and pressing the tips firmly onto the In. Care must be taken to not apply excessive force and damage the tips.

3.2.2 Physical Property Measurement System (PPMS):

The PPMS is a liquid Helium cryostat by *Quantum Design* which allows electrical characterization in the range between 1.8K and 400K. The sample stage can rotate 360 degrees and a magnetic field up to ±9T can be applied. Here, the contacts are manually wire-bonded using a copper (Cu) wire and cold indium (In) pressing to make contact. Our set-up provided eight distinct terminals to be controlled independently. A switchboard (which could be controlled either manually or automatically) was used to select which of the contacts to use at any one time. An unfortunate drawback of this set-up, is that once the sample is loaded, the contacts cannot be changed. For this reason, it is very important to ensure good contact prior to lowering the temperature.

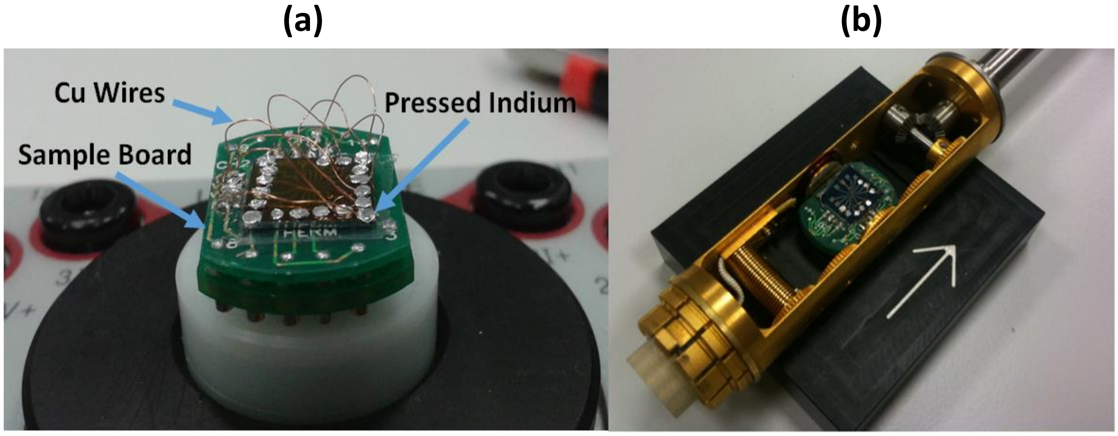

Figure 2. (a) Bonded Sample on test bed. (b) Sample in PPMS sample holder.

The sample is fixed to the sample board using either glue or double-sided tape. When using tape, it was found that applying multiple layers between the board and the sample improves contact between the sample and the board. This is especially important for LSV measurements, where the incident angle of a magnetic field on the sample must be well controlled. Once bonded, the sample board is placed into the PPMS's rotating sample holder (Fig. 2(b)) which is then used to lower the sample into the cryostat.

3.2.3 Measurement Details:

The precision of measurements can be controlled by setting the step size, delay and measuring range via the LabVIEW interface. Decreasing the step size, increases the sampling rate, resulting in more detailed measurements. The measurement range adjusts the level of sensitivity of the SMUs so as to better record the device output. Finally, a delay can be set to allow for the output to settle before it is measured, allowing for the exclusion of capacitive charging effects and thermal variations. Obviously, the desired accuracy of the measurements should always be weighted against the time required to record the data. Single electron transport and spin accumulation require very high precision measurements while current-voltage (I-V) curves of large aspect ratio tunnel junctions or resistance measurements of metals can be performed with less precision.

3.2.4 Signal to Noise Ratio (Delta Mode):

Lateral Spin Valve (LSV) measurements, consist of injecting a fixed amount of current into a device and detecting the resulting voltage arising (see chapter 5 for more details). These measurements require the detection of an interfacial voltage usually of the order of nV (10^{-9} V) across a metal-ferromagnet interface. Hence to acquire meaningful data the signal-to-noise ratio (SNR) must be kept very low. For the majority of measurements a current of 100µA was used. A simple method to improve the SNR, is by injecting more current and reading out large voltage signals. However, the frailty (low J_c of Py) of our LSV does not permit us to do so. To increase the quality of the measurement we apply a DC reversal technique which is an alternative to the commonly used AC lock-in technique (apply an AC current of given frequency and filter out all output signals with different frequency). To employ this method we use a 6221 current source and a 2182 nanovoltmeter.

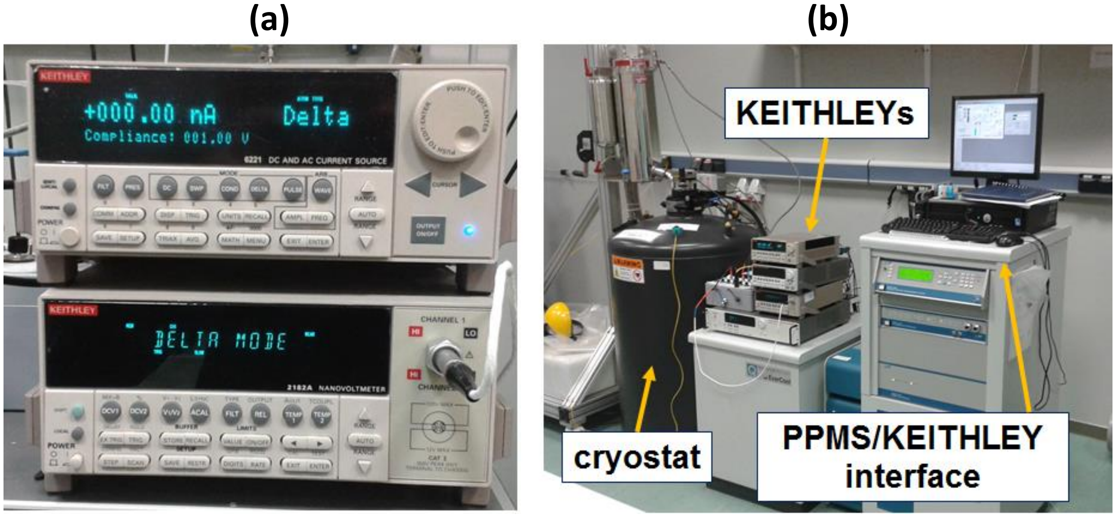

Figure 3. (a) 6221 Current Source (top) and 2182 nanovoltmeter (bottom) coupled for delta mode measurements. (b) Entire set-up. Cryostat, Switchbaord, KEITHLEYs and computer interface.

A series of DC current pulses of alternating polarity are applied and the resulting voltage during each pulse is recorded. If we assume a constant offset (eg. contact potential) and a (linearly) time-varying offset (eg. thermoelectric voltage) to be present in our signal we can write the first three pulse readings as:

$$V_A = V(A) + Noise$$
$$V_B = V(B) + Noise + \delta Noise$$
$$V_C = V(C) + Noise + 2\ \delta Noise$$

where V_i are the read values of each pulse, V(i) are the real signals, Noise represents the constant offset and δNoise represents the varying offset. We assume that V_A is taken at zero time. These three pulses constitute a delta cycle, whose final output is given by [181]:

$$V_{cycle} = \frac{1}{2}\left(\frac{V_A - V_B}{2} + \frac{V_c - V_B}{2}\right) = \frac{V_A - 2V_B + V_C}{4}$$

Finally, to further improve the measurement, the final output value is taken as the average value over a number of predefined cycles (typically 16). By setting the pulse amplitude, width, interval and the number of cycles the quality of measurement can be adjusted. Clearly, more accurate measurements require significantly longer time and put significantly more strain on the device. An illustration of the delta mode technique is illustrated in Fig. 4.

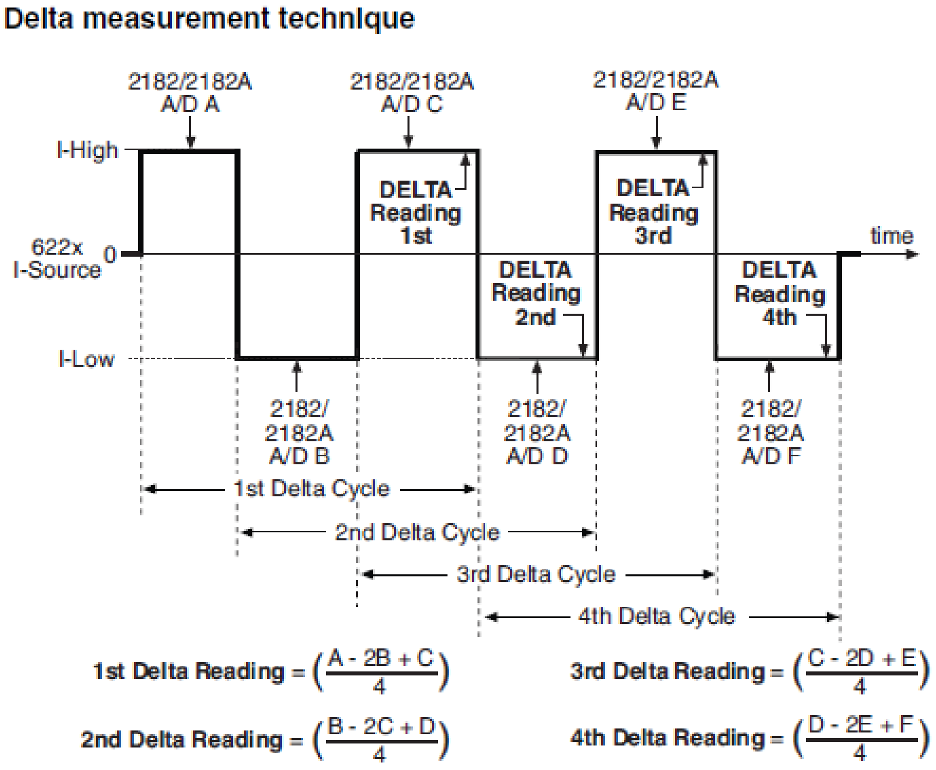

Figure 4. Delta measurement technique. Adapted from [182].

3.3 Tunnel Junctions:

In the following sections we discuss the charge transport in tunnel junctions made by all three methods described in chapter 2. In these devices, the electrode separation is so small that electrons can transfer across the insulating separation layer via quantum mechanical tunneling (see chapter 1).

The theoretical model for electron tunneling in Metal-Insulator-Metal (MIM) systems was put forward in 1933 by Sommerfeld and Bethe [183]. Since then, a vast amount of work has extended the theory in an effort to make it more representative of real devices [42, 177, 184-188]. The most notable and highly used works are those of Simmons [10, 42], which today are referred to as the Simmons model.

Similar to other reported methods the fabrication methods of chapter 2, yield devices whose tunnel junction characteristics have a certain degree of uncertainty [118, 189-192]. This uncertainty originates from the unavoidable nanoscopic non-uniformity of electrode edges which gives rise to multiple tunneling channels conducting simultaneously. By fitting our data to the Simmons model we are able to extract these characteristics and visualize the state of our junction.

3.3.1 The Simmons Model:

The Simmons model can be used to represent experimental systems but as pointed out [188, 177], its accuracy is inherently limited. The model assumes a vacuum insulating layer, significant uniformity in all parameters of the tunneling barrier and a temperature of T=0K [177], making it unrealistic for real devices. Unfortunately, attempts to improve the accuracy, although perfectly sound in a theoretical framework, are still not very useful for characterization of real devices. Early amendments of the model address issues such as the shape of the barrier, the asymmetry of the barrier as seen from each electrode, the effect of image forces on tunneling electrons and the effect of the insulator's dielectric constant. Later amendments have become more ambitious. Of these the most notable work is probably that of Miller and Beleya [177] who account for parallel tunneling channels and barrier height distributions. In this model, the authors use a variation of the WKB tunneling solution (see chapter 1) known as the Brinkman, Dynes and Rowell model [188] which presents an expression for the total tunneling current density in an asymmetric tunnel junction. To extend this work, the authors represent the barrier as a sum of individual barriers of parallel conduction channels. The contribution of each channel to the overall conductance is then weighted according to a given distribution, which in their work is chosen to be Gaussian. In this way their total current density is expressed as $j_{net}=\Sigma_n\alpha(\phi_n)j(\phi_n,s,V)$, where j is the current density, $\alpha(\phi_n)$ is the weighting coefficient of each channel, $j(\phi_n,s,V)$ is the current density of each channel, ϕ is the barrier height, s is the electrode separation, V is the applied bias and the index n represents the conductive tunneling channel in question.

Unfortunately, the advancements of such models often consist of increasing the fitting parameters and this can compromise the reliability of the fitting. Although these factors should be acknowledged when modeling a system, it is often best to use the original Simmons model and consent to the unavoidable variability within a tunnel junction. This way, the values obtained are appreciated as effective values, which represent the general conductivity of the system.

As described in chapter 1, the Simmons model represents the total tunneling current through an arbitrarily shaped energetic barrier. In order to fit our data to the Simmons model we rewrite the equation for intermediate voltages ($0<V_{ds}<V_b$) as [10]:

$$I(V) = A * \frac{6.17 * 10^{-6}}{s^2}\left[\left(V_b - \frac{V_{ds}}{2}\right)e^{-10s\sqrt{\left(V_b - \frac{V_{ds}}{2}\right)}} - \left(V_b + \frac{V_{ds}}{2}\right)e^{-10s\sqrt{\left(V_b + \frac{V_{ds}}{2}\right)}}\right] \tag{1}$$

where A is the tunneling area, s is the electrode separation, V_b is the potential barrier height and V_{ds} is the applied bias voltage. Parameters V_b and V_{ds} are expressed in Volts while A and s are expressed in nm^2 and nm respectively.

By fitting the measured bias-dependent current to this equation, the tunneling area, barrier height and barrier width (electrode separation) can be extracted.

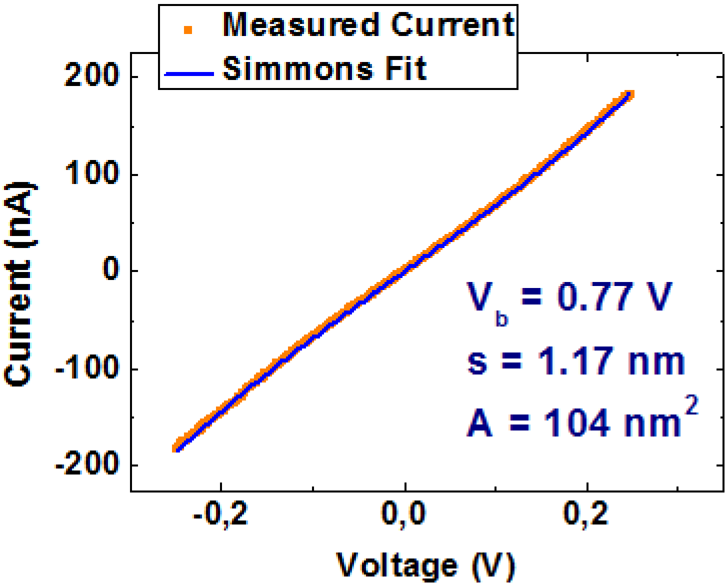

Figure 5. Fitting of measured I-V data to Simmons model.

The model assumes complete uniformity in all aspects of the barrier. In truth however, the current consists of that flowing via multiple conduction paths. The equation is hence used to extract the effective values of the entire junction which can best be used to describe the device in question.

Of the parameters included, the one which can be approximately know prior to electrical characterization is the tunneling area. The width of the electrodes is estimated by SEM while the thickness is estimated using either the quartz crystal microbalance (QCM) or X-Ray Reflectivity (XRR) measurements of a calibration film. For large tunnel junctions the relative error in such estimations is significantly decreased and fixing the area during the fitting is reasonable. In fact this is common practice in vertical tunnel junctions. However, due to the exponential dependence of the conductivity on the electrode separation and barrier height, the conduction can be dominated by localized paths of high conductivity [177]. These are known colloquially as *hot-spots*, and can result in the estimated area being significantly different from the effective area involved in the conduction process. For this reason, it is best to leave the tunneling area as a free parameter and use the QCM/XRR value as an upper limit to the fitting. This practice is increasingly important when the uniformity of the electrode separation decreases.

3.3.2 Limits of fitting:

Although increasing the number of fitting parameters can be more appropriate in certain cases, the results must be taken with caution. The reason for this is rooted in the inherent limitations of least square fitting methods such as the Levenberg-Marquardt method which we employ throughout this thesis. Least square fitting consists of applying algorithms to search the so-called chi-squared (χ^2) hyperspace for minima which represent solutions of the equation which are best suitable to the measured data. Chi-squared is a figure of merit which determines the goodness-of-fit and represents the difference between the measured data and the calculated solutions of the fitting equation. For the fittings of this thesis, we report a figure of merit called R, which is a variation of χ^2 and for which R=1 indicates a good fit. For each fitting parameter, χ^2 will assume a multitude of values and by converging to the minimum χ^2 a fit between the data and the theory can be achieved.

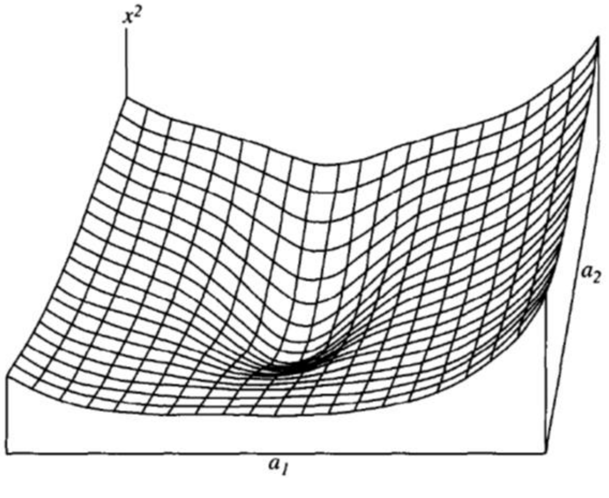

Figure 6. χ^2 hypersurface as a function of two parameters, a_1 and a_2. Taken from [193].

In Fig. 6, we see the χ^2 hypersurface resulting from the simultaneous fitting of two parameters. If a third parameter is introduced the surface will become a three-dimensional space and converging to a minimum of χ^2 can become troublesome. Convergence to a solution will depend on the details of the algorithm a detailed description of which can be found in [193]. By looking at the chi-squared hyperspace one can visualize the origin of commonly faced problems of fitting. The size, and shape of the minima as well as the starting points and search step size can cause the algorithm to overlook solutions and erroneously settle for solutions of local minima.

It is often the case that repeating the fitting results in the free parameters converging to distinct values each time, all with considerable fitting quality. Increasing the free parameters results in a more complex χ^2 hyperspace with more possible convergence points and increases the probability of false-minimum solutions. When faced with the problem of multiple minima, the fitting must be performed carefully. To avoid erroneous converging due to multiple minima, the fitting must be repeated multiple times. Each time, we can choose distinct free parameters and initial parameter values while checking the figure of merit. In our case, the estimation of the tunneling area can be used to fix the area parameter and fit only the barrier height and electrode separation. The tunneling area does not appear in the exponents and changes in its value do not largely affect the fitted barriers height and width. Hence, by repeating the fit for various values of tunneling area, we should be able to discern the values of the barrier height and electrode separation. Then the fit can be repeated by setting the initial values for these parameters to the ones found and fitting to find the tunneling area. As we see later on, the parameterization of fitting can result in distinct results and erroneous conclusions about the state of the barrier.

3.3.3 Role of Dielectric Constant: Vacuum versus Oxide Paths:

It is quite often that metal-vacuum-metal tunnel junctions made on insulating substrates are thought of as conducting only through vacuum. However, depending on the geometry and the oxide in question, the dielectric layer can be a viable conduction path. Realistic tunnel junctions will be faced with a multitude of conduction paths and the overall conduction can be dominated by an angstrom-sized area [194]. In order to fit an effective barrier, we require to select the effective mass of our medium and hence when faced with the parallel conduction paths of vacuum and the substrate oxide, we must consider both as possible paths.

The effective mass of the medium can largely affect the results of the fitting [179] and must therefore be chosen carefully. To be able to select an effective mass of $m/m_e = 1$, we must ensure that the conduction is dominated by the vacuum path. For the majority of devices, this dominance is supported by two simple arguments. Primarily, given that the electrons are sourced from the electrodes, the possible oxide paths will have larger electrode separation and smaller conduction area. The second argument lies in the quantum mechanical nature of tunneling which describes transport through and not over a potential barrier. Simmons has addressed this property in [10] where he shows that lower dielectric constants significantly lower the resistance for electron tunneling. For our devices, it is safe to assume that the vast majority of tunneling transverses the vacuum and the effective mass is always taken as 1.

3.3.4 Electrode Edge Roughness:

As deviations from the nominal design occur quite frequently when fabricating tunnel junctions, the conductivity of such devices is often unpredictable. As discussed in chapter 2 a certain degree of roughness is unavoidable at the electrode edges and this can have serious implications in the resulting tunnel junctions created.

This effect is exemplified in Fig. 7, where we see I-V measurements of tunnel junctions made via the Overhang method. The devices measured in Fig. 7 have been fabricated so as to be identical in every aspect except the width of the junction. Consequently, the tunneling area and the resulting current should increase with increasing width.

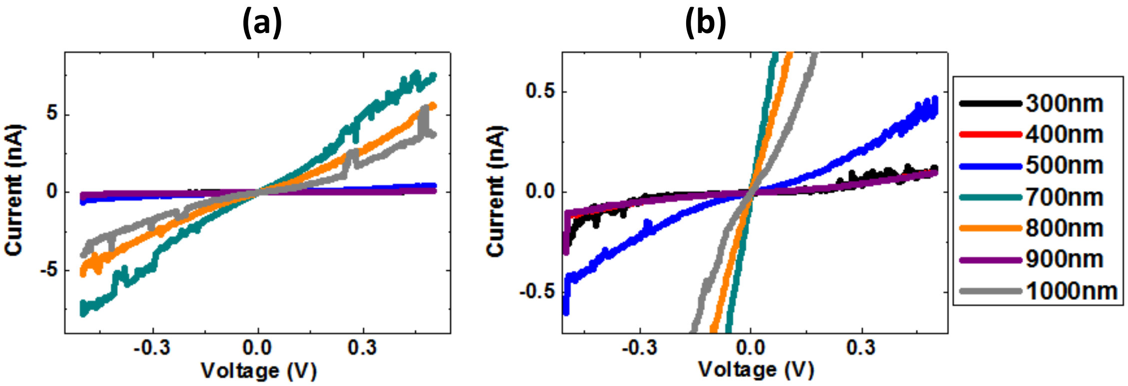

Figure 7. I-V Measurements of junctions of different tunneling areas made using the Overhang Method.

As can be seen, although a general scaling of the current with the tunneling area is present, it is by no means the one expected from tunneling theory implying that the effective tunneling area is not the one expected. This can be explained by considering a substantial electrode edge roughness. Protrusions from the electrode edges can activate localized points of shorter electrode separation which decrease the effective tunneling area and dominate conduction [194].

The unavoidable electrode edge roughness, is also responsible for asymmetric energetic tunnel barriers. As mentioned above, a large part of the advancements of theoretical tunneling models has been to account for the asymmetry of tunnel barriers. Having distinct barriers at each metal/vacuum interface gives rise to distinct conductivity for the forward and reverse directions of the current. To examine this, we can fit the forward and reverse current directions individually. Comparing this with the results obtained from the entire bias range we see that as expected the total bias represents a sort of average of the barriers of each direction. This shows that by using the model for a single effective barrier with individual bias directions the asymmetry can be highlighted and there is no need for more advanced models with increased parameterization.

	$-250mV < V_{ds} < 250mV$	$V_{ds} < 0$	$V_{ds} > 0$	Average
b (V)	0.188	0.168	0.224	0.2 ± 0.03
s (nm)	0.975	1.038	0.903	0.97 ± 0.07
A (nm^2)	141.847	159.830	127.750	144 ± 16
R^2	0.99923	0.99972	0.99976	

Table 2. Barrier height (b), barrier width (s) and tunneling area (A) obtained from Simmons fittings for various bias ranges

The junction area for the sample of Table 1, as estimated by SEM and XRR measurements is $250nm^2$. Given the high quality of the fitting ($R^2>0.999$) and the fact that the extracted values are reasonable, this fitting can be deemed trustworthy. The electrical characterization allows us to see that the effective tunneling area is much smaller than the one estimated, which means that only part of the metal-insulator-metal interfaces participate in the conduction. In Table 1, we see that parameters fitted to the entire voltage range are less accurate and give an average of the more accurate forward and reverse directions. This again supports the idea that the model represents an effective barrier and that protrusions from electrode edges can dominate the transport.

Another feature of the measurements of Fig. 7 is the significant amount of noise present. As discussed above, noise can originate from poor contacts. However, for some devices noise appears to produce reproducible conductance jumps at given voltages, or even permanent changes after several measurements. Such jumps are observed often [195] and can be attributed to unstable residues of the fabrication process which contaminate the tunnel junctions [169]. At sufficiently high voltages these residue particles can move and cause appreciable changes in the measured current.

In Fig. 8 below, we see repeated measurements of a tunnel junction. Note that at low voltages the differences are negligible whereas at higher voltages they become more pronounced. Furthermore note how the step present for positive bias during the first measurement disappears in the following measurements. Such measurements cannot be well fitted and the real state of the device remains unknown. In the presence of such measurements the tunnel junction can be cleaned thermally by applying a sufficient amount of current to result in a current annealing. However, it is best to ensure a clean junction by means of ultrasounds and N_2 gun spraying and ensure good electrical contact. If the source of noise cannot be identified and the noise cannot be removed, the devices must then be disregarded.

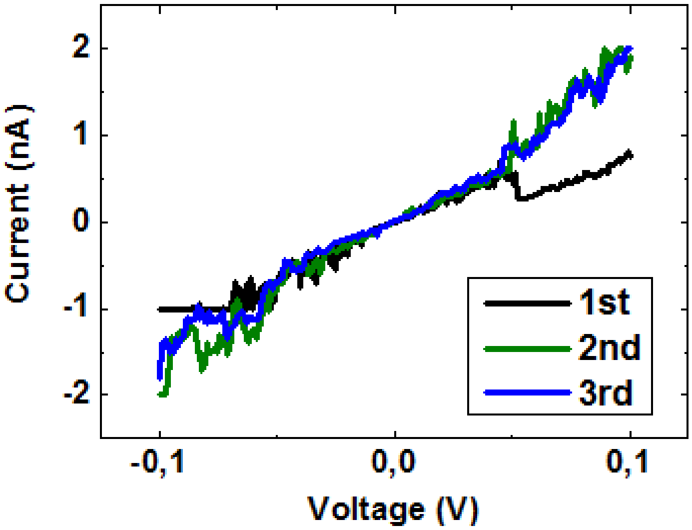

Figure 8. Repeating the measurement can cause the output to stabilize due to the current. In the first measurement (black) there is a large step for positive bias. Repeating the measurement causes a permanent alteration removing the step from the measurement. The step is hence an artifact.

3.3.5 Temperature Effects on Barrier Parameters:

The temperature dependence of tunnel junctions is often used to determine the quality of a tunnel junction, i.e. the amount of electrical insulation between the two electrodes. For a well-insulated junction, the resistance slightly increases at lower temperatures, while for a poorly-insulated junction the resistance will slightly decrease [196, 194, 197]. These changes in conductivity are accompanied by changes in the barrier parameters. The temperature dependence of the barrier parameters can be determined by fitting the current measured at each temperature to the Simmons model. This method of characterization has been widely applied to magnetic tunnel junctions (MTJs) and is used to determine the presence of metallic protrusions which short-circuit the two electrodes [194, 198, 196]. These protrusions are thought of as one dimensional wires connecting the electrodes and are known as pin-holes.

The common approach to such characterization is to fix the tunneling area to a constant value and fit the barrier height and electrode separation. As the temperature is lowered, well-insulated samples (no pin holes) show a decreasing electrode separation and an increasing barrier height whereas poorly-insulated samples (pin holes) show the opposite temperature dependences [194, 198].

In the late 60's Rowell's criteria dictated that the temperature dependence of a tunnel junction should be due solely to thermal smearing [197]. However, the meticulous analysis of Miller and Belyea showed that the effect of the Fermi-Dirac distribution on the effective barrier parameters is much smaller than that of the junction's interfacial roughness (electrode edge roughness) [177]. Moreover, they showed that increasing the standard deviation of such barrier distributions causes a reduction of the effective barrier height and an increase in the effective barrier thickness (electrode separation). This trend is exactly what is expected to occur when lowering the temperature of poorly insulated junctions, but despite a mention of a barrier distribution, there is no reference to poor insulation in [177].

In our analysis, we assume that a decrease of the tunnel resistance indicates a well-insulated barrier. Then, by fitting measurements of such a junction, we find that the temperature dependence of the barrier parameters depends on the choice of fitting parameters. If the area is fitted, we find a relationship similar to the case where pin holes are present and if the area is fixed we see the temperature dependence of a well-insulated barrier.

Table 2, shows the values extracted from fitting I-V measurements of a well-insulated tunnel junction taken at different temperatures. By fitting all three parameters, we find that the effect of decreasing temperature on tunnel junctions is similar to that of the case of pinholes and the case of increasing the standard deviation of the barrier distribution.

	300K	**120K**	**60K**	**8K**
Barrier Height (V)	0.19	0.09	0.077	0.07
Electrode Separation (nm)	1.12	1.51	1.75	1.84
Tunneling Area (nm^2)	15.97	21.25	26.3	32.1

Table 3: Variation of barrier parameters with temperature.

Having all three parameters free we observe than in fact a simultaneous change occurs. As the temperature is decreased, the electrodes become slightly more separated. While this happens the effective tunneling area increases and the effective barrier height is decreased (see Fig. 9).

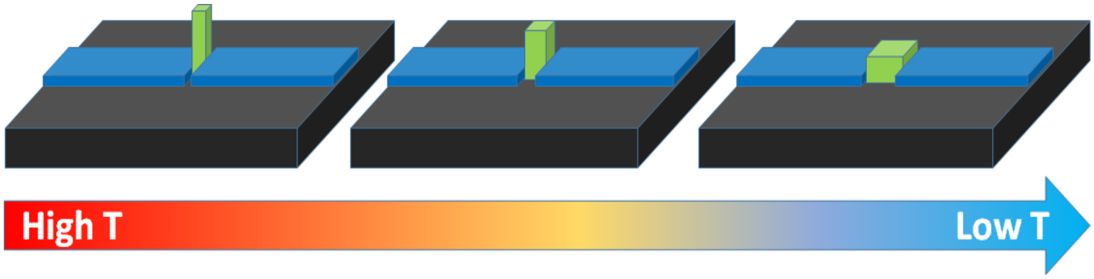

Figure 9. Illustration of the temperature effect on the potential barrier. As temperature decreases the height decreases, the electrode separation increases and the area increases.

The increase in the electrode separation observed is one which is highly plausible considering thermal expansion effects (Δs = 0.64nm over ΔT = 292K). In fact the use of thermal expansion has previously been proposed as a fabrication technique for nanogaps [199]. The change in length Δl due to a change in temperature ΔT of a given material structure can be expressed by [200]:

$$\frac{\Delta l}{l_0} = a\Delta T \qquad (2)$$

where l_0 is the initial length and a is the coefficient of thermal expansion (CTE). Considering the thermal expansion coefficient of our Si substrate ($a_{Si} = 2.9\ \text{x}10^{-6}$/K) we can imagine that a temperature variation of ΔT = 290K would cause a substrate of 10mm length to undergo a change of Δl = 290K * 10x10^{-3}m * 2.9x10^{-6}/K= 8.41μm. A similar calculation can be performed for the electrodes. Platinum (Pt) and palladium (Pd) which were commonly used as electrodes in our devices both have CTE of approximately 10x10^{-6}/K. For an electrode of length of 1μm the resulting deformation would be about Δl = 290K*1x10^{-6}m*10x10^{-6}/K= 2.9nm. From this simplistic calculation, we see that sub-nanometer changes in the electrode separation could in fact be attributed to thermal expansion. Considering the exponential dependence of tunneling current on inter-electrode distance, such changes could lead to extensive differences in the barrier shape and could explain the observed changes in the barrier.

An increase in electrode separation will decrease the relative inter-electrode distances between the adjacent conduction paths, allowing more channels to participate in the conduction. This would then result in a larger effective tunneling area, as observed. While this occurs, the effective barrier height decreases. Note that the effect of increasing the effective tunneling area that we observe is similar to the effect of increasing the standard deviation of the barrier distribution shown by [177].

Unfortunately, the exact calculation of how much expansion to expect and the resulting augmentation of the tunneling area is a complicated matter and methods of directly measuring it are unavailable.

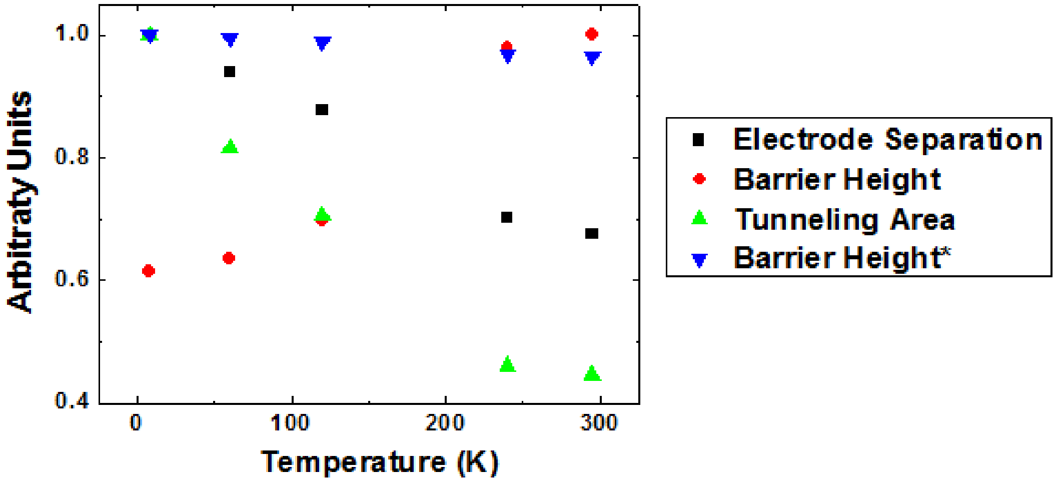

Figure 10. Normalized fitted barrier parameters for different temperatures. Barrier Height (blue) represents that found while fixing area and separation. Barrier Height (red) represents the results of the simultaneous fit.*

To test the reliability of our fit, the analysis is repeated while fixing the tunneling area. In this case, we find that the barrier height increases with decreasing temperature (see Fig. 10), which has previously been associated with well-insulated tunnel junctions [198, 194].

When fitting a well-insulated barrier one parameter at a time, the increase in tunnel resistance can only be accounted for by a change in the free parameter, and the parameter will be forced to assume the appropriate value. In contrast, in a simultaneous fitting, the increased tunnel resistance is accounted for by the increasing electrode separation while the area and the barrier height are *free* to change in any way.

Although the relative quality of single parameter fits is generally lower ($R^2 < 0.9983$) than that of multiple free parameters, the difference is practically insignificant. For this reason, the conclusion of the fitting must be chosen carefully. Clearly, fitting poorly insulated samples to models for well-insulated junctions can cause erroneous results and the results must not be trusted. The temperature dependence of the barrier parameters of a well-insulated device can hence be found to differ depending on the method of fitting. In our analysis, the change is believe to result from thermal expansion, which by physically altering the inter-electrode distance can change the distribution of the energetic barrier resulting in distinct effective tunneling areas and effective barrier heights.

3.4 Conductive Particles in Nanogaps:

To achieve tunnel junction structures we apply fabrication processes which involve tearing of metal sheets (lift-off) and forceful, high-temperature translocation of metallic ions (EM). Due to the nature of the fabrication processes, metal nanoparticles can sometimes brake off from the electrodes and find themselves trapped in the nanogaps. These nanoparticles can have any shape and size and if they happen to couple to the device electrodes they can transform the transport characteristics substantially. Although measures can be taken to encourage the presence of such particles the majority of available methods have exceptionally low yield. For this reason nanogap devices with nanopaticles were studied only when naturally occurring. In the remainder of this chapter we will focus on particle-dominated transport and see how such structures can give rise to single electron transistor (SET) devices.

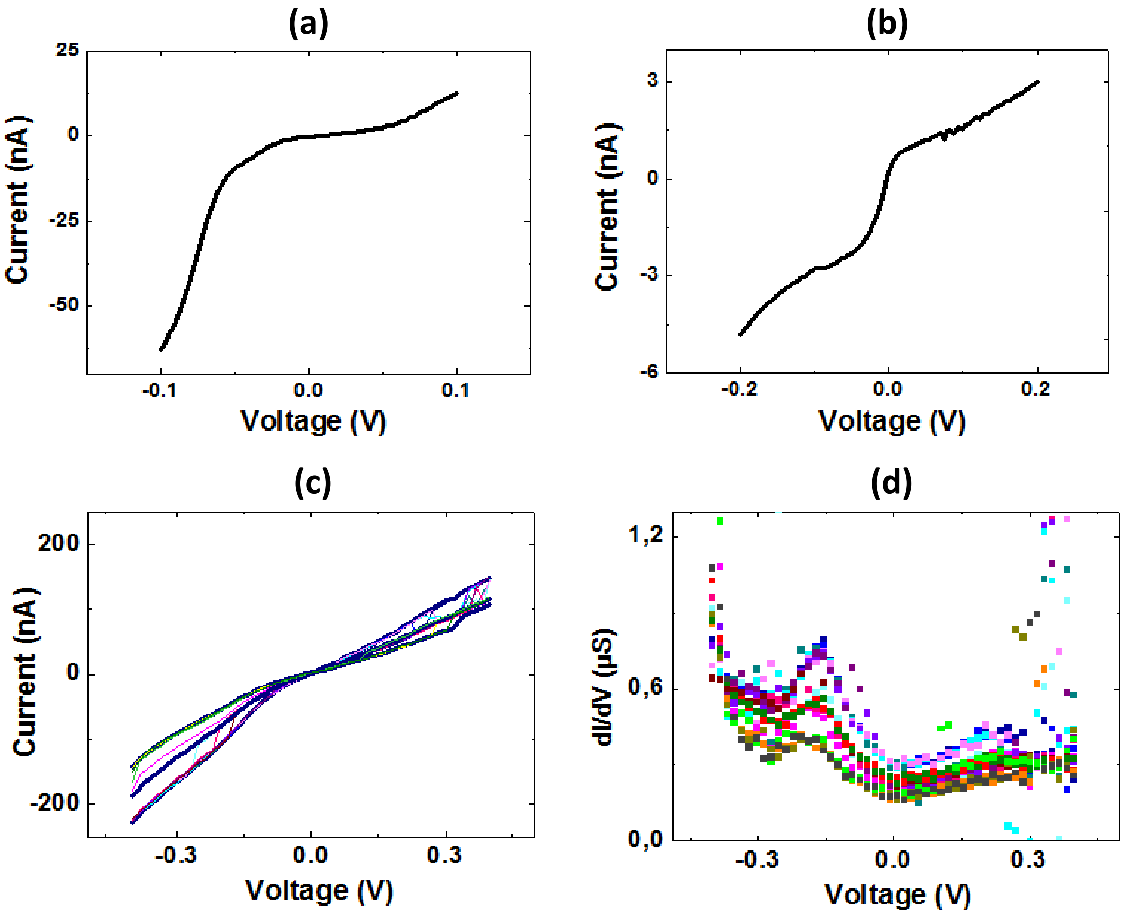

Figure 11. Features which often hint at the presence of a nanoparticle in the gap. (a)Excessive barrier asymmetry (b) Unusual current-voltage relationship (c) Gate dependence of channel transport. Measurement over the range -4.5V < V_{GATE} < 4.5V, with step size of 530mV. Curve jumps between 3 principal conduction curves. (b) Differential conductance (dI/dV) of data from (c). Conductivity shows a maximum around -170mV. This maximum can be modulated by a gate voltage via an electric field effect.

The effect of the particles on the devices transport will depend on the electrical coupling with the device electrodes. Hence, while the effect of some particles is clearly visible in simple I-V measurements, other particles might go unnoticed. Placing an amorphous particle in a nanogap, will effectively break the existing tunnel junction into two (or more) distinct tunnel junctions increasing the transport asymmetry. Although this does not provide definitive evidence, excessive asymmetry in a tunnel junction could hint towards the presence of a particle. A slightly stronger indication of particles is the appearance of unusual transport features such as plateaus or peaks in the measurements of current or differential conductance. However, while these features hint towards the presence of particles the only way to ensure their presence is to check if the transport is sensitive to the gate voltage, i.e. if a field effect is present.

Under very specific conditions, very small particles can behave as confined electronic systems, coupled to the electrodes via tunnel barriers. In this context, the concepts of coupling strength and transmission coefficients come into play and the particle is referred to as a dot. Dots exhibit discretization of their electronic spectrum which gives rise to unique transport characteristics. The addition of a gate electrode to the source-dot-drain system is commonly referred to as a single electron transistor (SET) [201].

3.5 Single Electron Transistors:

The coupling of the dot to the electrodes in a tunnel-barrier results in its electrical isolation which in combination with the particle's energy discretization give rise to Coulomb Blockade (CB), a characteristic property of SET transport. This property entails charges needing a specific amount of energy before they can tunnel onto and off of the dot. CB appears as a blockaded, zero-conductance region, which exhibits a bias-dependent periodicity. Its presence is favored by small particles (larger discretization) and large tunneling resistance (larger electrical isolation). Large tunneling resistance, indicates weak coupling and results in first order tunneling processes. Low tunneling resistance indicates strong coupling where transport will be dominated by higher order tunneling processes which will mask the presence of CB. To observe CB we must fulfill the following two conditions [50, 78]:

A. Charge Addition Energy >> Thermal Energy ($E_{Add} = e^2/C \gg k_BT$)

B. Tunneling Resistance >> Quantum of Resistance ($R_t \gg h / e^2$)

where e is the electron charge, h is planks constant, C is the total capacitance of the dot, k_B is Boltzmann's constant, T is temperature and R_t is the resistance of the tunnel barriers. E_{Add} is the charge addition energy, which consists of the sum of the charging energy E_C and the energy level spacing ΔE of the dot, $E_{Add} = E_C + \Delta E$. Typically, $E_C \gg \Delta E$ and accounts for the majority of the charge addition energy, and sometimes E_C and E_{Add} are used interchangeably. This implies that the principle reason for blockade is in fact electrostatic repulsion and not the discretization of energy. Clearly, low temperature and high tunnel junction resistance (weak coupling) promote the fulfillment of these conditions.

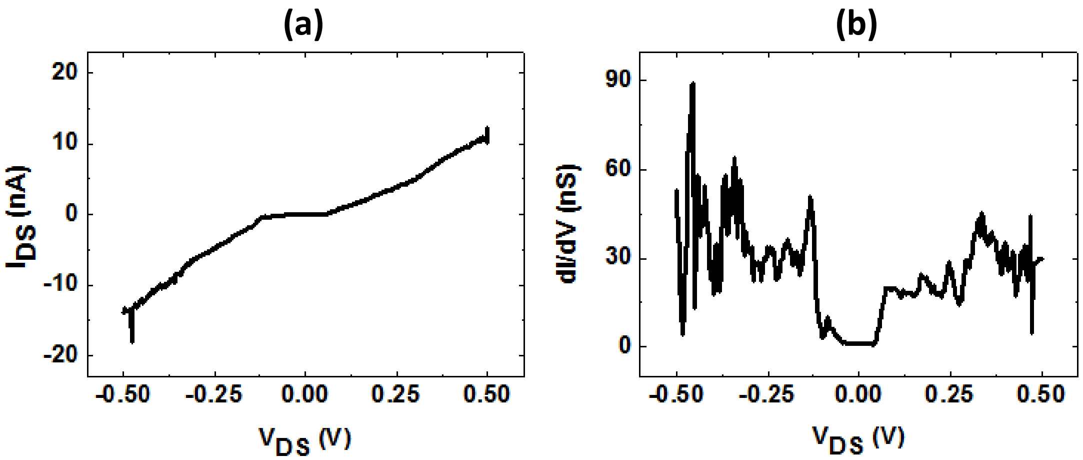

Figure 12. (a) Measurement of Coulomb staircase. Clear steps can be seen around V_{ds} *= ±320mV. (b) Differential conductance (dI/dV) plot of same data indicating the plateaus of conductivity*

In Fig. 12, we see a measurement of a sample with a metallic nanoparticle exhibiting CB. Tunneling through the dot depends on the relative tunneling rates (Γ_S, Γ_D) of the two tunnel barriers. Steps in the I-V measurement indicate addition of charge to the dot and addition of available transport channels [201-203]. These steps are collectively referred to as a Coulomb Staircase.

The staircase profile is thought to indicate single particle coupling in the device [169, 203]. In Fig. 12(a), at about V_{DS}= ±100mV, we see CB lifted by the increase of V_{DS}. CB can also be lifted using the gate voltage, which can shift the dot's discrete energy level and align them with the electrochemical potentials of the source and drain electrodes. The stronger the coupling of the dot to the gate electrode, the easier it will be to manipulate the dot's energy and lift the CB.

3.5.1 Stability Diagrams:

The intricate bias dependence of SET devices is best viewed via a type of conductivity map called a stability diagram. Such maps can be constructed by recording I_{DS}-V_{DS} measurements over a range of gate voltages, and simultaneously plotting the differential conductance ($\partial I_{DS}/\partial V_{DS}$) against V_{DS} and V_G. Due to the CB effect, blockaded states reflect negligible conductance which in such plots take the form of diamonds. In Fig. 13, we see an illustration of the energy diagram of an SET and a stability diagram that would emerge.

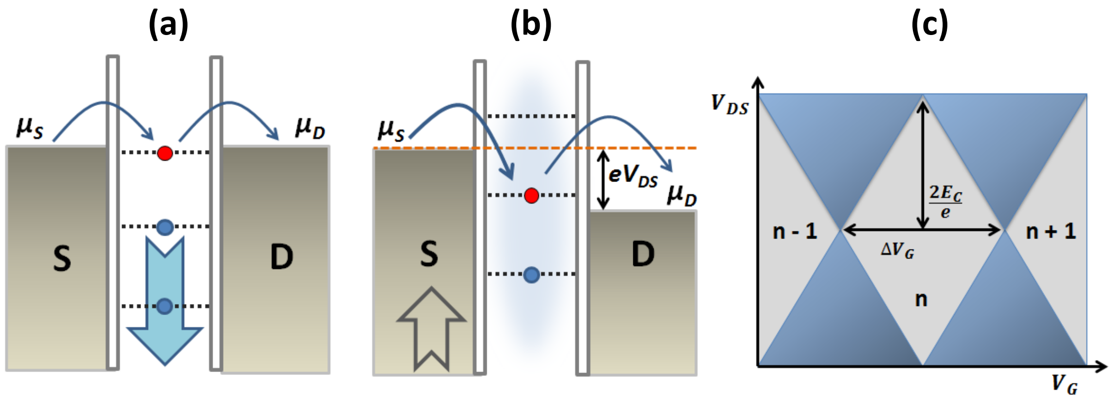

Figure 13. CB in an SET. The blockade is lifted either by applying a gate voltage V_G (a) or a source-drain voltage V_{SD} (b). (c) Sketch of a stability diagram. Light regions represent negligible conductance while darker regions represent appreciable conductance. Adapted from [204].

Stability diagrams contain a plethora of information about the devices. Each diamond represents a state of the dot in which the number of charges on it is fixed. Clearly, increasing V_G allows addition of charges to the system. The width of the diamonds reflects the capacitance of the dot to the gate electrode whereas the height of the diamonds is related to the charging energy [205]. The slopes of the diamond allow us to discern the dot's capacitance to the source and drain electrodes [78]. All this information can be extracted using the following simple set of equations [78]:

$$\Delta V_{SD} = \frac{4E_C}{e} \tag{3}$$

$$\Delta V_G = \frac{e}{C_G} = \frac{E_C}{e\beta} \tag{4}$$

$$\left(\frac{\Delta V_{SD}}{\Delta V_G}\right)^{+} = \frac{C_G}{C_G+C_D} \tag{5}$$

$$\left(\frac{\Delta V_{SD}}{\Delta V_G}\right)^{-} = -\frac{C_G}{C_S} \tag{6}$$

In Equations 3-6, ΔV is the width (G) or height (SD) of the diamonds, e is the electron charge, E_C is the charging energy, β is the gate coupling strength and C is capacitance. The indices S, D and G represent the source, drain and gate respectively while the indices + and – refer to the positive and negative slopes of the diamonds respectively.

The measurement is recorded at T=2K and requires a large amount of time (can be several hours), during which the characteristics of the plots can be shifted. Such shifts are ubiquitous in CB measurements and are thought to result from sudden changes in the local electrostatic environment [206]. Clearly, such changes are more probable in inhomogeneous systems such as ours, where residue particles play the role of dots and electrode-channel interface roughness gives rise to a distribution of tunnel barriers. Such random charges are very difficult to eliminate experimentally and represent a severe problem in realizing practical device technologies based on single-electron devices [207]. Just like with clean tunnel junctions, deviations from ideal behavior are to be expected and the stability diagrams recorded may not exhibit well-defined diamonds.

Additionally the random nature of particle trapping can result in multiple particles occupying a single gap. This gives rise to a superposition of CB effects which can be referred to as stochastic CB [208]. In this case, the ordered diamonds appear as a chaotic arrangement of shards, which despite its appearance consists of intricate but coherent patterns reflecting CB transport [208].

In Fig. 14 we see stability diagrams of particles trapped during the Overhang process. One device exhibits Coulomb diamonds while the other exhibits Coulomb shards, implying the presence of multiple particles. In the case of diamonds, we can use Equations 3-6 to extract information about our system. Unfortunately as the diamonds are not so well defined the resulting calculations will serve more as estimates than exact values.

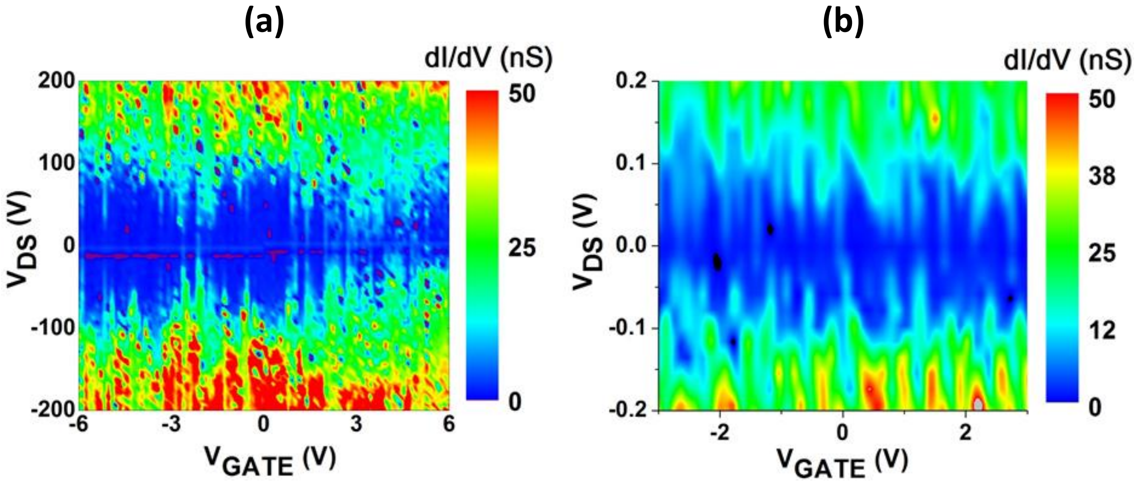

Figure 14. Stability diagrams of particles trapped during the Overhang process, displaying (a) Coulomb diamonds and (b) Coulomb shards.

From these calculations we can extract $C_G = 3.6x10^{-20}$ F, $C_S = 89x10^{-20}$ F, $C_D = 85x10^{-20}$ F giving a total capacitance of $C_{TOT} = C_G + C_S + C_D = 1.8x10^{-18}$ F. The charging energy is found to be $E_C = 45meV$, which is indeed substantially larger than the thermal energy at 2K, $k_BT = 0.17meV$. An estimation of the particles' size can be made by solving for self-capacitance. By approximating the particle to a sphere, we can use $C_{self} = 4\pi\varepsilon d$, where ε is the permittivity of the particles surrounding and d is its diameter. From this, we estimate d=16nm. As expected [203], C_G is an order of magnitude smaller than C_S and C_D. The gate coupling factor was found to be $\beta = 0.01$, indicating week coupling. The values obtained are in excellent agreement to those obtained by [205], in which

SETs were created by artificially positioning colloidal Au nanoparticles of 15nm diameter as dots. Finally the energy level spacing ΔE, can be estimated using the free-electron expression for the density of states at the Fermi surface of a 3D grain [203]:

$$\Delta E = \frac{2\pi^2\hbar^2}{mk_F Vol} = \frac{1.5eVnm^2}{k_F Vol}$$

where ħ is the reduced planks constant, m is the electron mass, k_F is the electron wave number, which for Au is 12.1nm^{-1} and Vol is the volume of the spherical particle ($4\pi r^3/3$). From this relationship, we can estimate the energy level spacing within the dot to be ΔE = 58μeV which as expected is significantly smaller than the charging energy [203].

Such a small ΔE puts our device into the classical Coulomb Blockade regime ($\Delta E << k_BT$) where a tunneling electron can access what is essentially a continuum of excited states of the dot [209, 158]. Alternatively, if $\Delta E >> k_BT$, we find ourselves in the quantum Coulomb Blockade regime, where each quantum state of the dot is treated separately. This distinction becomes important for further analysis of the device, when transmission coefficients are calculated.

3.5.2 Room Temperature Operation:

The first demonstration of room temperature operation of an SET [210] came about 8 years after the first SET [75] and was carried out using a Silicon nanowire as the SET's island. Semiconducting materials, such as Silicon, contain a smaller amount of electrons within them than metals, making level discretization easier which ultimately makes them a better choice of material for dots [40]. Regardless, to observe CB, the aforementioned conditions must be satisfied. For room temperature operation large charging energies are needed as E_{CA} must exceed the thermal energy of k_BT = 25.8meV. Such charging energies typically require dots with a diameter of less than 5nm [211, 40]. Given that decreasing the temperature is much simpler than coupling small dots to electrodes a great deal of work on SETs has involved low temperatures [147, 146, 212, 205, 75, 213].

Using the electromigration technique we have been able to convert Py nanowires into SETs functioning at room temperature. In this case the resulting device is quite different. In a method similar to before, we find E_C = 250mV, $C_{TOT} = 3.2\text{x}10^{-19}$ F, β = 0.18 and d = 3nm. The requirement of a small particle is most certainly fulfilled, and the charging energy is now substantially larger, allowing for room temperature operation. An interesting observation is that the gate coupling to the dot is much stronger. This effect could arise from the fact that the electromigrated Py nanowire consists of a tapered geometry, which has been found to improve the gate coupling by three orders of magnitude [214].

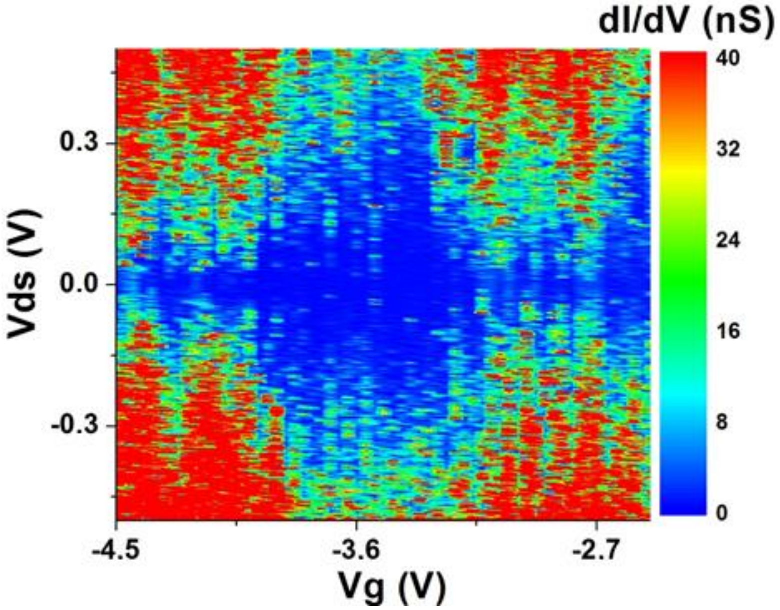

Figure 15. Stability Diagram of RT operating SET made by Py electromigration.

Using the methods described in chapter 2, fabrication of sub-10nm nanogaps can sometimes result in SET devices. These devices, arise form metal residues of the electrodes themselves which once trapped in the junction can behave as dots. While the yield of SETs is extremely low their presence during such fabrication methods has been previously observed [215, 147, 216]. SETs were obtained with all three fabrication methods applied offering a unique opportunity to study single electron transport phenomena.

Chapter 4:

Molecules in Nanogaps

4.1 Introduction:

In this chapter we make use of nanogap devices to study charge transport through molecular semiconductor (MS) materials. The unique electrical and structural properties as well as the distinct processing methods of such materials have pushed MS into a number of technologies such as displays, photovoltaics, sensors and transistors.

Of the materials available, carbon-based molecules have presented the most attractive electrical properties and for this reason we study charge transport through the molecular semiconductors C60 fullerene (C_{60}, C60) and Pentacene ($C_{22}H_{14}$, Pc). These materials are large-bandgap semiconductors whose transport properties are determined by the amount of order in their structure. As a result, the charge carriers residing within these materials can simultaneously be subjected to a variety of transport mechanisms. In addition the semiconducting nature of these materials implies that they exhibit an affinity for either electron (C60) or hole (Pc) dominated transport.

The dominance of a given mechanism will depend on the temperature, the channel length and the state of the material. Using our nanogap devices we probe distinct mechanisms of this multifaceted transport process, many aspects of which have yet to be understood [50, 51, 217]. Finally we see the changes that MS can undergo during operation and the resulting effect on the device's conductivity.

4.2. Molecular Devices:

4.2.1 Device Preparation:

As mentioned in Chapter 2, the devices assume a transistor geometry with channel length varying between 1nm and 100nm. Electrical characterization allows us to discern the cleanliness and approximate size of the channel and to select appropriate devices for this study. Devices exhibiting either an insulating junction or a clean tunneling junction behavior were selected for probing MS.

Using clean tunnel junction devices, an initial attempt was made to incorporate molecules into the channel via drop casting. The drop casting was performed by our colleague Thales de Oliveira and involved a solution comprising of a mixture of CH_3OH and CH_2Cl_2 which contained the molecule $C_{18}H_{12}Fe_{14}$ which was synthesized by collaborators from the Karlsruhe Institute of Technology in Karlsruhe, Germany. The solution was dropped onto the entire surface of a substrate and left to evaporate.

Electrical measurements revealed no increase in conductivity and SEM imaging showed that the molecules in question formed individual crystal-like structures whose size and shape where largely inappropriate for coupling to the nanogap electrodes (see

Fig. 1). After several failed attempts, it was decided to deposit the C60 and Pc molecules to which there was already affinity in our group.

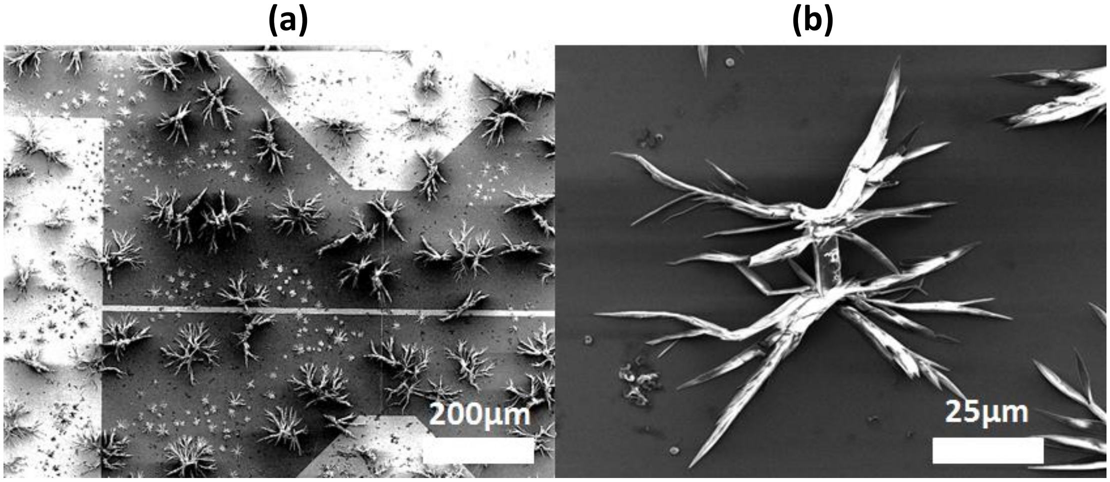

Figure 1. Result of drop-casting deposition of molecules. (a) substrate covered in conglomeration of molecules (b) individual molecular crystal formed after the evaporation of the solution

Film growth, was carried out by thermal evaporation and sublimation in ultra-high vacuum ($P<10^{-9}$ mbar). The molecules were deposited as thin films (15nm-60nm thick) over a masked substrate. To make sure that the macroscopic contacts were free of molecules, we created hark masks of either Aluminum foil or Kapton tape which were roughly shaped with scalpels.

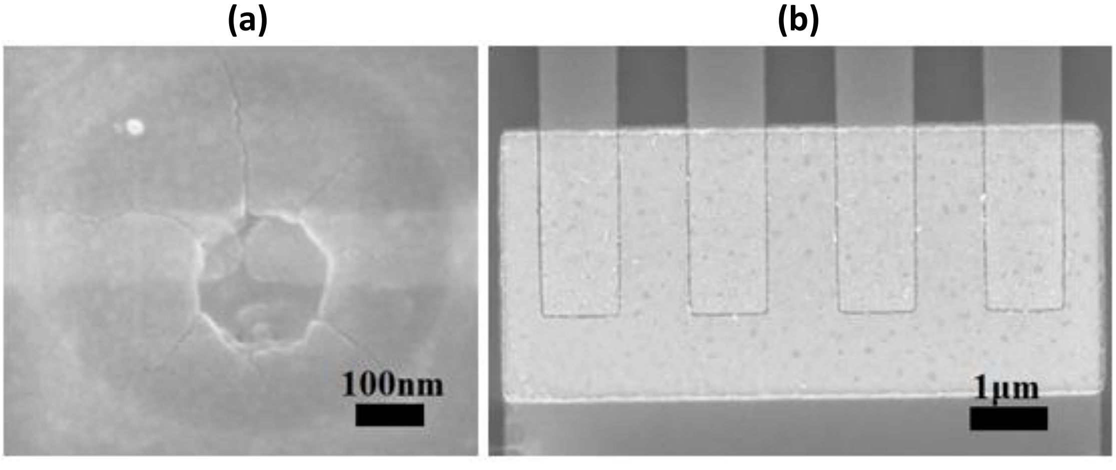

Figure 2. (a) EBL defined nanogap with circular PMMA window to isolate C60 in the channel. Outer circle is due to SEM charging effect. (b) Interdigitated Overhang nanogaps with rectangular PMMA window to isolate Pc in the channel.

Then to isolate the MS in the channel we used an EBL process with PMMA. For back-gated devices such as these, channel isolation has been found to improve device performance [218] but isolating nanogap channels can be quite challenging. In addition, standard EBL resists such as PMMA are known to chemically react with carbon based materials causing spurious doping and irreproducible MS layers. For this reason, the channel is exposed by defining a small window in PMMA overlapping the electrode edges and before the deposition of the molecular layer an Argon-Oxygen ($Ar:O_2$, 2:1) mixed plasma cleaning is performed to ensure the cleanliness of the channel. The resulting nanogap devices with MS layer in their channels can be seen in Fig.2.

4.2.2 Device Measurement:

In addition to the cautious preparation of molecular devices, the measurement of transport through a MS channel must be done with care. As in the case of metallic nanoparticles, MS transport can be modulated via an electric field which is applied by biasing the gate electrode. Effective application of such fields requires the dielectric layer to provide sufficient electrical isolation to avoid leakage currents appearing in the channel. Such currents can completely mask the channel signal rendering our devices useless.

This effect is showcased in Fig. 3(a) where we see that the measured channel current (black) is in fact a replica of the leakage current (red) appearing in the channel. Samples made on 150nm SiO_2 appeared to suffer frequently from large leakage currents implying that the dielectric layer received a substantial amount of damage during the fabrication process. To deal with this problem, we began to fabricate molecular devices on 250nm thick SiO_2 dielectrics and the leakage was considerably reduced. Reliable measurements were taken as ones where the channel current was at least an order of magnitude larger than the leakage (see Fig. 3(b)).

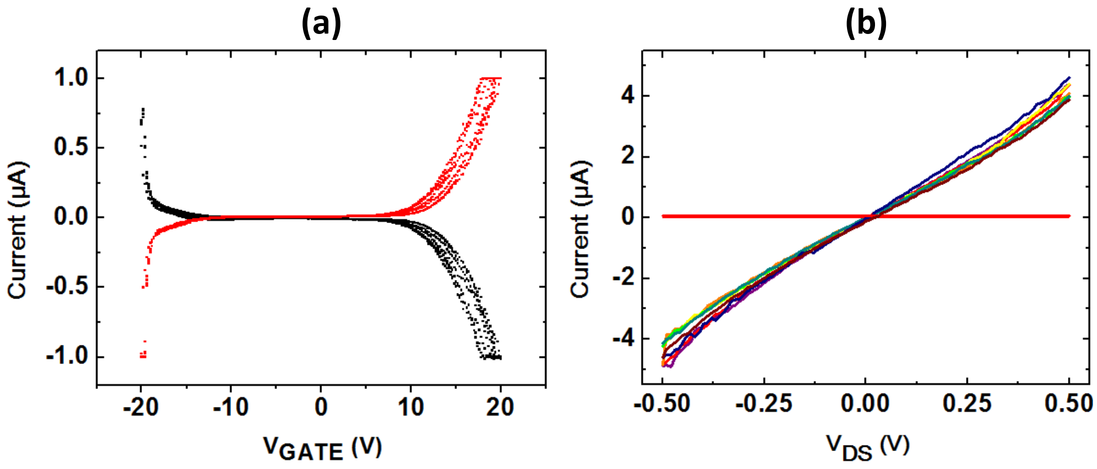

Figure 3. Leakage current (red) in molecular nanogap devices. (a) Channel current and leakage current are mirrored and increase at high gate voltages. Measurements taken over the range -1.5V < V_{DS} < 0 V. (b) Leakage current is negligible over the range -24V < V_G < 24V.

To ensure that we are measuring transport through the MS channel, we must hence confirm that the leakage current from the gate is negligible. Moreover, given that our channel consists of a large bandgap semiconductor spurious channel currents can also arise from incoming light in the form of photocurrent. To observe the true electrical transport of the channel one must hence ensure that the measurements occur in a dark space.

Finally, a significant amount of MS materials are subject to rapid oxidation, i.e. are not *air-stable*. Simple exposure to ambient conditions will alter their properties by oxidation and introduction of charge traps [56, 219-222]. This is a troublesome characteristic, which implies that devices must be measured directly after deposition and in decent vacuum ($P<10^{-4}$mbar).

4.3 Transport in Molecular Devices:

4.3.1 Bias and Temperature Dependent Transport:

Transport in molecular devices can occur via several mechanisms. Given the large disorder and the large bandgap of the MS layer, charge carriers are faced with potential barriers, and hence transport usually involves some form of tunneling or hopping. Unsurprisingly, transport measurements tend to yield non-linear current-voltage characteristics.

Transport in MS can simultaneously occur via distinct mechanisms. Affinity to a given mechanism may manifest depending on channel size, applied bias, and sample temperature and transitions between dominant mechanisms can be frequently observed [53, 11, 48, 12, 223]. Transitions between band transport and hopping transport, hopping and field emission as well as direct tunneling and field emission have been reported in MS [223, 11, 12]. As some of these mechanisms involve thermally assisted tunneling, measuring transport over a range of temperatures and discovering the temperature dependence of conduction helps reveal more information.

While weak temperature dependence is associated with direct tunneling and field emission (unassisted tunneling processes), large temperature dependence is associated with mechanisms such as hopping and Poole-Frenkel (PF) tunneling (assisted tunneling processes). Furthermore, negative temperature dependence is often regarded as evidence for band transport [217].

In Fig. 4 and Fig. 5, we see the measurements of two C60 devices over a range of temperatures. *Device A* was created via the overhang method and includes one Ti/Au (2.5nm/22.5nm) electrode and one Py (19nm) electrode. The electrode separation is approximately 120nm, and the thickness of the C60 channel is 40nm. *Device B* was created via a single step EBL process and consists of two 7nm thick Pt electrodes separated by less than 10nm and a 15nm thick C60 channel.

In both devices we see a temperature dependent conductance, indicative of thermally activated transport. However, despite both channels consisting of C60, we see that the two devices behave differently. For *device A* (Fig. 4), the mechanism is maintained over a large range of temperatures, while for *device B* (Fig. 5) there appears to be a transition between 200K and 160K, at which the transport becomes invariant to temperature. Furthermore, we can see that even though the electrode separation of *device B* is significantly shorter, its overall resistance is much higher.

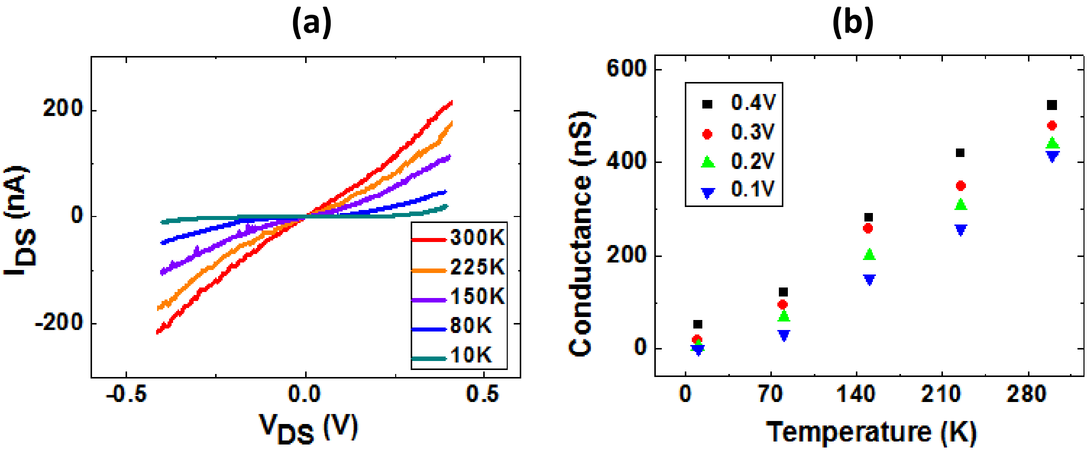

Figure 4. (a) Channel current and (b) conductance for device A indicating thermally activated transport. The transport mechanism is maintained during the entire range of temperatures

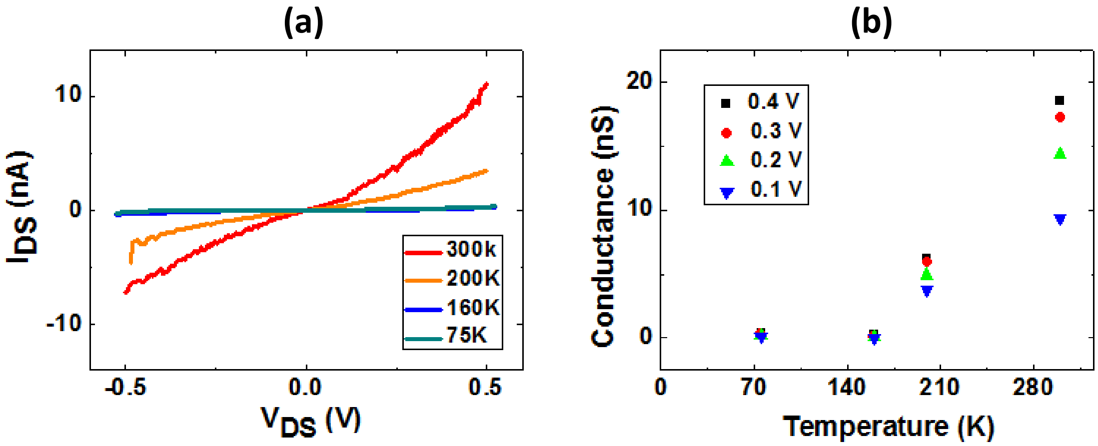

Figure 5. (a) Channel current and (b) conductance for device B. Below 200K, the transport mechanism undergoes a transition from thermally assisted transport to thermally invariant tunneling.

This could be attributed both to the lower quantity of C60 in the channel and to the use of Pt electrodes, which as we explain later are less (energetically) compatible with C60 than Au and Py. As the temperature is decreased, the resistance of the devices is increased. As this happens, the already resistive *device B* becomes so resistive, that the only transport mechanism available to electrons is tunneling.

The behavior of *device B* is similar to that of Worne et al. [12] who report a low temperature transition between thermally activated transport and thermally invariant field emission for devices using the MS materials P3HT (i.e. poly(3-hexylthiophene)) and TIPS-pentacene (i.e. 6,13-bis(triisopropyl-silylethynyl)).

Transition between thermally invariant mechanisms can also be identified. Following the work of Beebee et al [11], the transition between direct tunneling and field emission can be observed. When the applied bias exceeds the barrier height of a trapezoidal barrier, the barrier will assume a triangular shape and the transport will be dominated by Fowler-Nordheim (FN) tunneling (i.e. field emission). This transition point, represents the barrier height of the trapezoidal barrier, and can be determined by the slope of $\ln(I_{DS}/V_{DS}^2)$ versus (1/V). This relationship results from re-arranging and linearizing the Simmons model for high biases, which essentially describes the case of field emission. This transition can be seen in Fig. 6 which depicts the measurement (Fig. 6(a)) and appropriate transition plot (Fig. 6(b)) of a Pt-C60-Pt device. Note that such transitions have been reported in a multitude of molecules and devices geometries and are theoretically plausible in every system where tunneling is present [11, 224]. The dotted line indicates the transition between transport mechanisms. Clearly, the inadequacy of the Simmons model to precisely describe the system implies that the transition voltage, V_{trans} remains an estimate and not an exact measure of the barrier height [11].

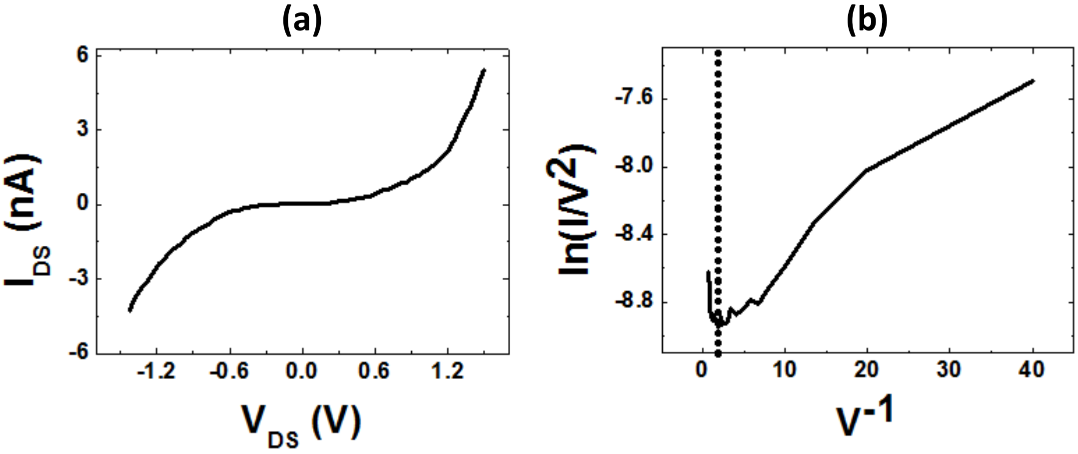

Figure 6. (a) I-V Measurement of channel current. (b) Plotting the data of (a) to reveal the bias dependent transition between direct tunneling and field emission. A transition is indicated by the dotted line at V_{DS}=0.38V.

Transport in MS can thus assume multiple forms, interchangeable under the appropriate stimulations of bias and temperature. Moreover, charge transport in such devices can transpire either by electrons moving through the LUMO or holes moving through the HOMO. The position of the electrode Fermi levels relative to the HOMO and LUMO levels of the MS will influence the bias-symmetry of the device, whether n-type or p-type transport will prevail and the overall resulting conductivity [53, 225, 220]. A better understanding of such features can be obtained by examining the dependence of transport on the bias of a gate electrode, which is commonly referred to as the field effect.

4.3.2 Field Effect:

In Fig. 7, we see a rigid band energy diagram displaying the relative energy levels of the materials used in our devices. The values given are approximate, and vary significantly within the literature due to dipole effects at the interfaces [53, 225-229].

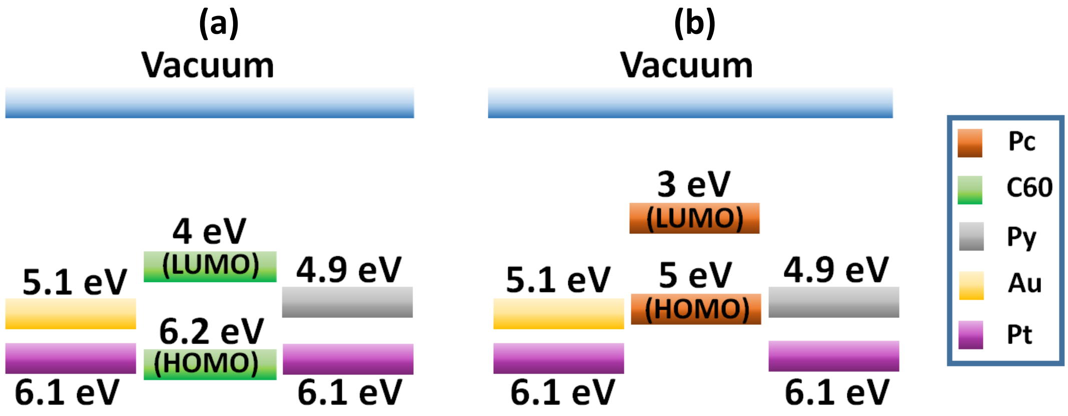

Figure 7. Rigid energy band diagram of our molecular devices with (a) C60 and (b)Pc. The metals used for source and drain electrodes were Permalloy (Py), Gold (Au) and Platinum (Pt).

To observe the semiconducting nature of these materials, we apply a gate voltage which via the field effect allows for a modulation of the charge carrier concentration within the MS and gives rise to a modulation of the channel current. For Pc the current increases with decreasing gate voltage, indicating the material's p-type nature [230]. Similarly, for C60, the device becomes more conductive as the gate voltage is increased, indicating the material's n-type nature [231]. This effect can be seen in Fig. 8, which shows measurements of the channel current under various applied gate voltages.

An interesting observation, is that the electrodes used in the device of Fig. 8(b) device are made of Pt, whose work function places it in an almost perfect energetic alignment with the C60 vacuum HOMO level. Despite this, the transport appears to be n-type, demanding at least the modulated component of the current to flow via the LUMO. Considering that interface dipoles can cause molecular orbitals to shift by more than 1eV, the preference of Pt charge carriers to inject into the LUMO is quite plausible [52, 232]. The Pc devices used Au electrodes whose work function places them energetically close to the HOMO, encouraging p-type transport. Given the p-type transport observed in Pc, we can assume that if any interface dipoles where present at the Au-Pc interface they would be considerably smaller than the ones observed in the Pt-C60 devices.

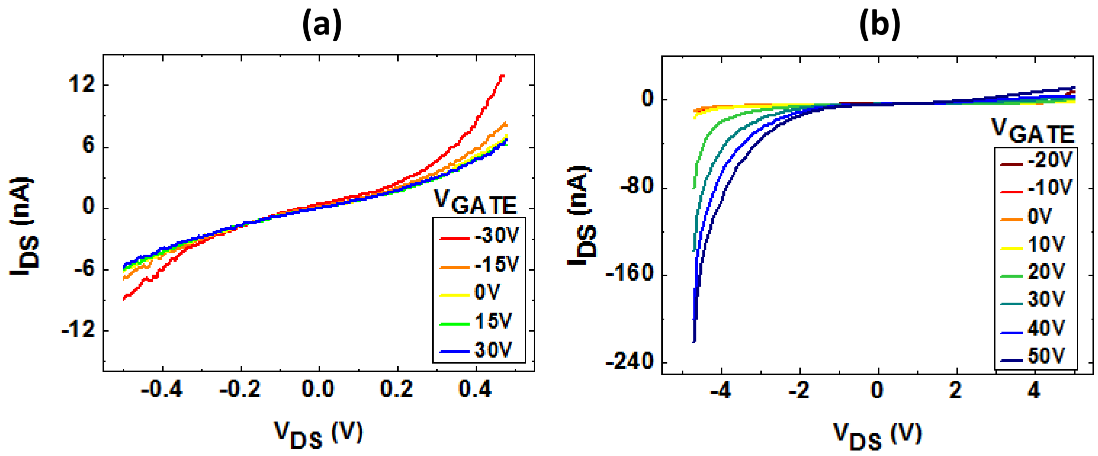

Figure 8. Field-Effect of (a) Pc showing p-type behavior and (b) C60 showing n-type behavior

A curious result is the asymmetry occurring in short-channel C60 devices. For *short-channel* (700nm) C60 devices, asymmetry has been reported before and has been attributed to a reduction of the *effective gate voltage* for $V_{DS}>0$, in samples with large contact resistance [233]. Similar asymmetry has also been noted in the large bandgap semiconductors ZnO and InGaZnO in large scale transistor geometries. In this case the asymmetry is attributed to a gate dependent channel resistance which largely depends on the polarity of V_{DS} [234].

In our devices, the typical channel lengths are much smaller (<100nm) and significant asymmetry has been observed only in C60 devices. Despite this, we have not found any explanation for which the asymmetry originates or is anyhow related to the presence of C60 in our devices and it seems plausible that the effect is in fact device-specific. Nevertheless, in accordance to other work, we have observed a multitude of unexpected transport features in C60 devices [219, 235, 236]. While a concrete explanation of these feature remains elusive, the next section will be dedicated to the presentation and discussion of unusual behavior observed in C60 devices.

4.4 Unusual C60 Transport Features:

Conduction through C60 has been associated to a variety of transport phenomena and can transpire both via electrons and holes [227, 223, 237]. In a series of measurements, our C60 devices showcased a variety of unusual transport characteristics. Several devices exhibited features which have previously been reported, such as negative differential conductance, rectification and bi-stable resistance [219, 235, 236], while instances of completely unexpected behavior were also observed. Electrical characterization of C60 channels revealed characteristic features of Coulomb Blockade, such as negligible conductance regimes and non-monotonic gate modulation.

These effects have been observed in large (<200nm) and small (<20nm) channels alike and are thought to be related to the formation of unique carbon-based structures within the C60 channel.

The most notable characteristic of our nanoscale devices was their limited tolerance to bias current. Similar to the cases of thin metallic wires, nanoscale molecular channels have proven to be susceptible to changes at sufficiently high voltages. These changes have been found to be partially reversible and are associated with diminishing of the field effect, increase of the bias-symmetry and an overall increase of conductivity. In Fig. 9, we see an example of a C60 device which starts by exhibiting asymmetric gate-modulated current and after several measurements permanently exhibits symmetry, no field effect and increased conductivity.

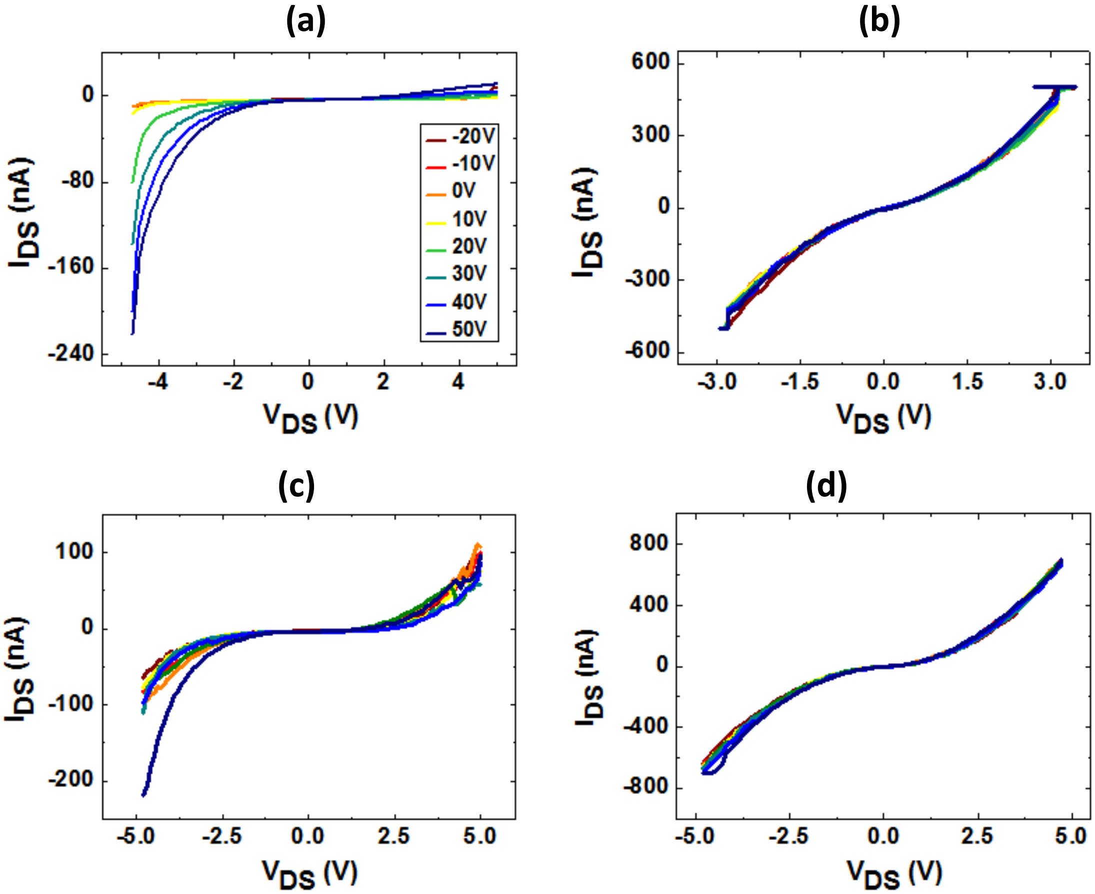

Figure 9. Evolution of conductivity during high bias measurements. Applied gate voltage is always as in (a) from -20V to 50V in steps of 10V. (a) First measurement shows gate modulation and asymmetry. (b) Second measurement shows increased conductance, almost no asymmetry and no gate response. (c)During the 3rd measurement, the device seems to revert to an intermediate state between (a) and (b). The fourth and all consequent measurements show increased conductance, symmetry and no field effect.

Improvement of the contact resistance via current annealing may contribute to the increase in current but cannot explain the damping of the field effect and hence other effects must come into play. SEM imaging of such devices has revealed that electrical measurements can result in severe degradation of the devices (see Fig. 10) and even result in the physical melting of the electrodes. Prior to this, increased leakage current has also been observed, hinting at the degradation of the insulating dielectric layer.

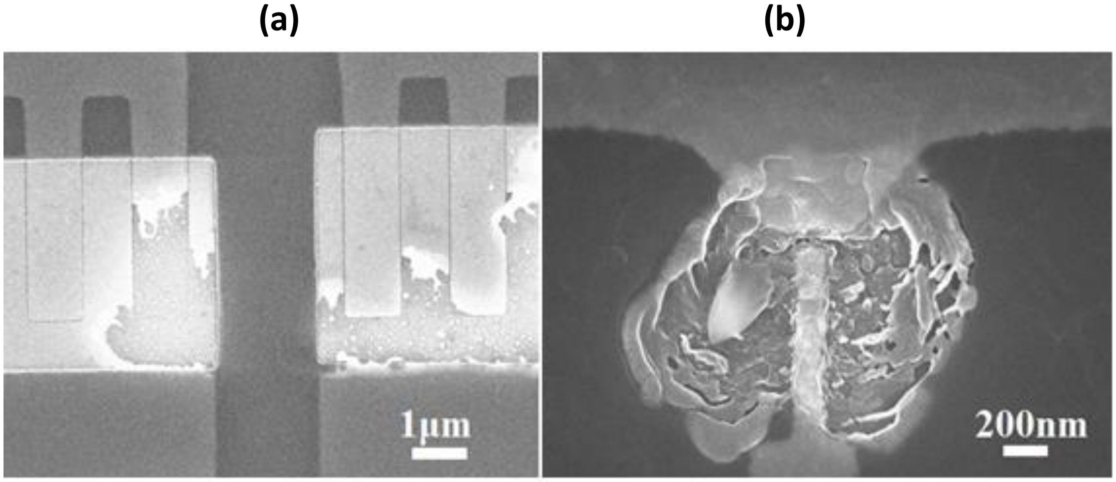

Figure 10. Device break down due to large bias. The melting of the electrodes indicated large temperatures are involved. In (b) we see that the organic material can be affected prior to the destruction of the electrodes.

These effects indicate that large local temperatures can arise in the area of the channel. Joule heating of face-center-cubic (fcc) C60 (which is the most common configuration), has been shown to result in a series of structural transformations, disbanding into disordered molecules and further changing into amorphous carbon (C) structures, with largely increased conductivity [238]. Interestingly, strain in C60 films has been found to result in both reversible and irreversible changes in the materials conductivity [237]. The collapse of the materials' structure, will also result in the reorganization of the molecular orbitals with sp^2 hybridization commonly emerging under high temperature [239, 238]. Although temperature induced transformations of our material are a highly possible source of the observed changes, a detailed study of the effect is required to confirm this.

While a series of unexpected characteristics have been observed in our C60 devices, the most curious effect has been the CB-like behavior of a device with a large channel (80nm). In this device, despite the channel consisting of a relatively *large-scale* semiconducting material we observe behavior similar to that of conductive nanoparticles, or single C60 molecules. Electrical measurements of this device are depicted in Fig. 11.

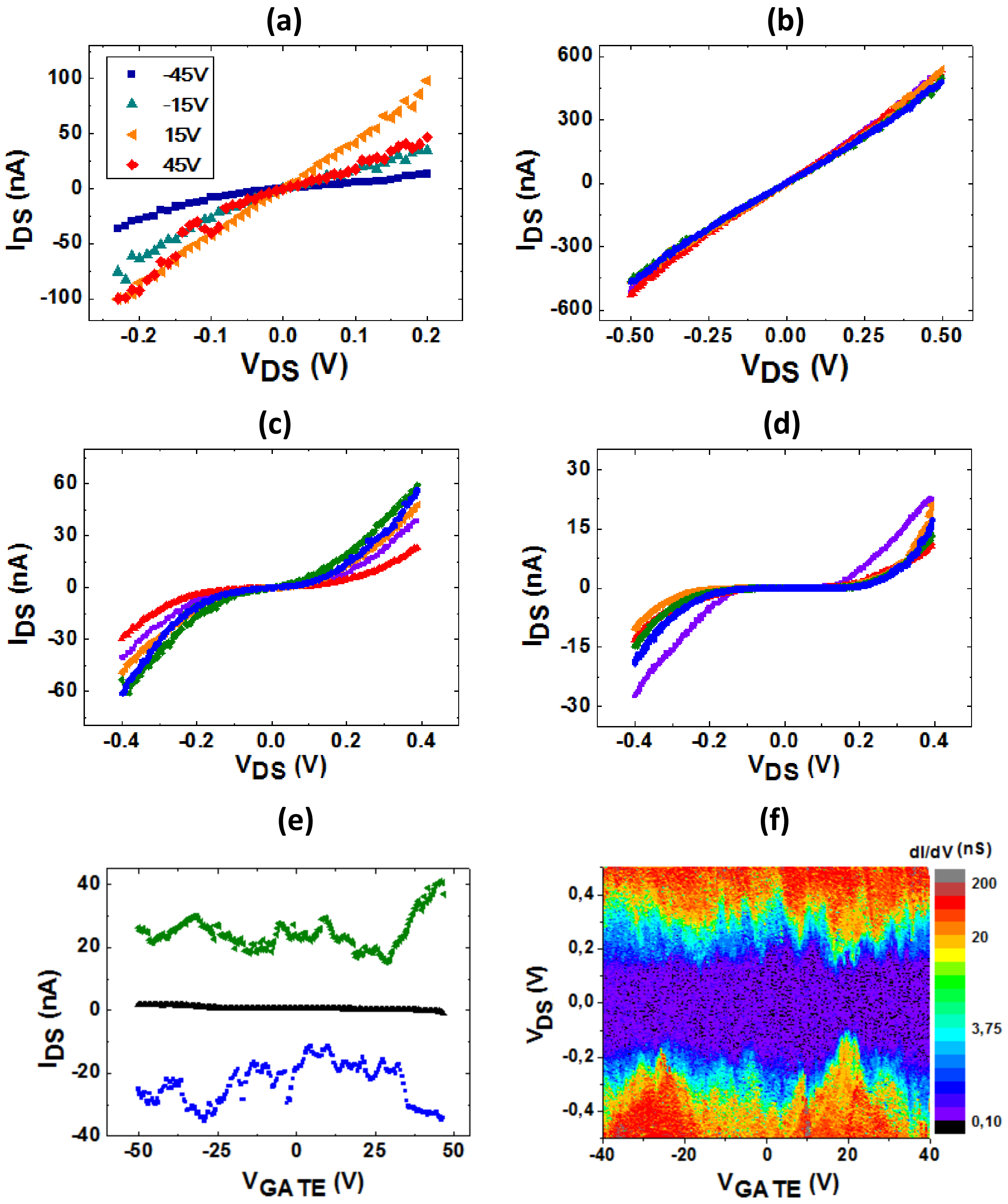

Figure 11. Anomalous behavior of a 80nm long C60 channel. In (a)-(f) the gate voltage was varied by more than ±40V. (a) First measurement shows non-monotonic gate modulation, i.e. conductance oscillates while steadily increasing or decreasing the applied gate voltage. (b) After three measurements the channel exhibits minimal modulation, increased conductivity and symmetry. (c) Lowering the temperature down to 80K, we observe a decrease of conductivity and the recovery of non-monotonic gate modulation. (d) At 10K we see signs of Coulomb Blockade. (e) Gate-dependence of channel current for positive (green), zero(black) and negative (blue) source-drain bias. (f) Stability diagram of 80nm long C60 channel at 2K resembles Coulomb Shards.

Initial measurements reveal a non-monotonic gate dependence of the source-drain current. Despite being at low bias, repeating the measurement gives rise to a transformation which appears to cause an increase in the conductance and a decrease of the field effect. Unexpectedly, upon lowering the temperature, the non-monotonic field effect is recovered indicating a conditional reversibility of the previously mentioned transformation.

After the recovery of the gate modulation, the temperature was continuously lowered until 10K, at which temperature the channel current seemed to be subject to CB (see Fig. 11(d)). At this point the device was brought to a temperature of 2K where a stability diagram was measured and features resembling Coulomb Shards emerged.

Given that the devices appeared as an electrical *open circuit* prior to C60 deposition, the presence of residue conductive nanoparticles is unlikely. Moreover, even if such particles had somehow found themselves in the gap, they would have to be small enough to exhibit energy discretization and large enough to bridge the electrodes, which are separated by approximately 80nm. Semiconducting materials can exhibit energy discretization in larger volumes however C60 is not known to do so in evaporated film assemblies. Attempts to bridge the FET and SET regimes have previously been made while claiming that the quantized electronic levels of C60 are conserved even when C60 is in a cluster or a crystalline state [233] however definitive reports on this issue are lacking.

The explanation of our measurements calls for the presence of a C60-based structure with some degree of energy discretization. The existence of high-aspect-ratio C60 nanowhiskers and C60 nanotubes have been widely reported and contact resistance to metallic electrodes can be extremely high [238]. Given that the irregular gate modulation was present in the initial measurement, it is possible that the appropriate C60 structure was formed during the layers' deposition and did not result from bias-induced transformations.

The resemblance of the stability diagram to Coulomb Shards, hints towards the coexistence of multiple conduction pathways, with discretized energy and weak coupling to the electrodes. These conditions, can be accounted for by assuming the formation of parallel carbon-based quasi-one-dimensional nanowires embedded into the channel. Unfortunately, ascertaining our beliefs about the observed transport characteristics required a significant amount of additional work and the infrequent occurrence of such C60 devices largely impeded our progress. Inevitably, an in-depth examination of unusual C60 transport features was left for the future

Chapter 5:

Lateral Spin Valves

5.1 Introduction:

In this chapter we explore a basic spintronic device, known as the Lateral Spin Valve (LSV) where spin information is transported through a ferromagnetic/non-magnetic/ferromagnetic (FM/NM/FM) metal nanostructure. In spintronic devices, electrons can retain their spin information and same-spin electrons can accumulate to form spin populations. In LSVs, spin populations are injected and detected by the FMs and are transported in the NM channel. Spin-retaining carrier transport must occur before the spin information is lost which requires transport to occur over a length scale smaller than the *spin diffusion length*, λ, or equivalently, in a time scale smaller than the *spin flip scattering time*, τ_{sf} (see chapter 1). Thankfully, for many materials these scales are relatively large ($100nm < \lambda < 1\mu m$) and readily accessible by current nanotechnology.

Using LSV we explore the effects of dimensionality on diffusive spin transport. Initially a constriction is placed in the NM transport channel by electron beam lithography (EBL) and the resulting spin signals are compared to those of single-width channels. Thereafter, we proceed to electromigrate (EM) the constriction in small steps, further diminishing the width and recording the evolution of the spin signals in the process. After reviewing the fabrication and characterization techniques applied, we review the challenges encountered during this experiment and the attempts made to overcome them. Careful analysis is supported by simulations of our experiments and a novel method of spin valve characterization emerges.

5.2 Design:

Standard LSVs where adapted to include variable channel widths and to withstand multiple EM and spin transport measurements. Thankfully, our group's affinity for spintronics allowed optimized fabrication and characterization methods to be exploited. In this section we will see the fabrication process applied to create such LSVs and the implications of including a locally variable channel width in our design.

The design consisted of a FM/NM/FM structure comprising of two FM nickel-iron alloy ($Ni_{80}Fe_{20}$, or Permalloy, Py) electrodes intersected by a copper (Cu) nanowire at 90 degrees (see Fig. 1). The Py electrodes are used to inject and detect spin populations which are transported via the Cu channel.

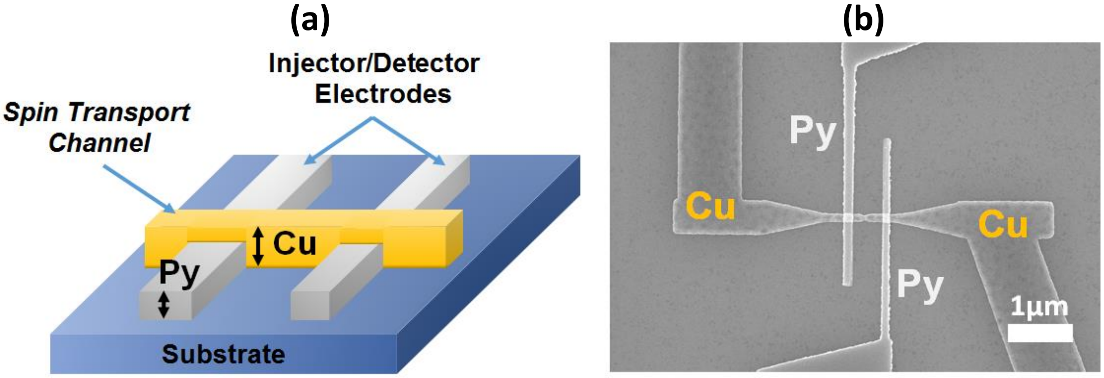

Figure 1. (a) Schematic of a Lateral Spin Valve. For our design, the thickness of Py must be substantially less than that of Cu so as to avoid discontinuity at the junction. Two-headed black arrows indicate the thickness of the electrodes (b) SEM image of actual LSV device with constricted channel

5.2.1 Channel Requirements:

To monitor small changes in the spin signal, EM has to occur in small controllable steps. To achieve such control, the channel must consist of a narrow wire, allowing for the critical current density, J_c to be reached at low voltages. Thankfully, the typical channels in LSVs consist of long narrow wires, as this shape assists the dense accumulation of spin populations and enables the transport to be modelled by one-dimensional diffusion theory (see chapter 1) [85, 108, 240-243].

Despite this convenient coincidence, the dimensionality of the Cu channel presents a trade-off. While narrow wires assist the concentration of spin populations, reducing the Cu dimensionality can lead to an increased resistivity, which will decrease the ability of electrons to retain their spin within the channel.

For our devices, the channel was chosen to have a width of 130nm and a thickness of 40nm. These values allowed for a decent control over the EM and the generation of an appreciable spin signal. The channel length (edge-to-edge FM electrode separation) was initially set to be 500nm, but then decreased to 300nm in order to increase the resulting spin signal.

The Cu and Py electrodes, were fabricated in two distinct steps. To better control the EM process, we wanted to have the Py electrodes overlapping a continuous Cu wire. Unfortunately, for reasons which remain unclear, fabrication of the Py electrodes over the Cu caused a considerable reduction of the channels' conductivity, making the EM less controllable and the spin-retention properties poorer. Therefore, the Cu channel was inevitably fabricated as the last step overlapping the Py electrodes.

5.2.2 Ferromagnet Requirements:

The need for this layout implied that the Cu channel would be faced with a discontinuity at the Cu/Py intersections, which could largely increase the probability of EM occurring at the overlap. To avoid such complications the Py thickness was required to be considerably smaller than the Cu thickness. Consequently, the FM electrodes of our LSVs were not very robust.

As seen in chapter 2, Py has a low critical current density ($J_c = 0.9 \times 10^{12}$ A/m^2) and hence cannot withstand much current. For our design, this was quite unfortunate, as the very nature of the experiment requires a large number of measurements over a long period of time. Just as with Cu, reducing the dimensions of Py allows EM to take place easier as the critical current density is reached rapidly.

Increasing the width of the Py electrode is not an option as it will cause a considerable decrease in the resulting spin signals. The Py widths have been previously optimized [13] to give the optimum combination of low switching fields and sufficiently small FM/NM interface areas (which increases the signal). The shape of a long straight line, terminated with a nucleation pad, was chosen to compel the magnetization switching to be as abrupt as possible. By choosing slightly different widths (125nm and 80nm) the Py electrodes obtained distinct coercive fields of relatively low values (typically between 100Oe and 300Oe). Having low coercive fields allows us to acquire the spin signal with less data points, making the process faster and less strenuous for the electrodes.

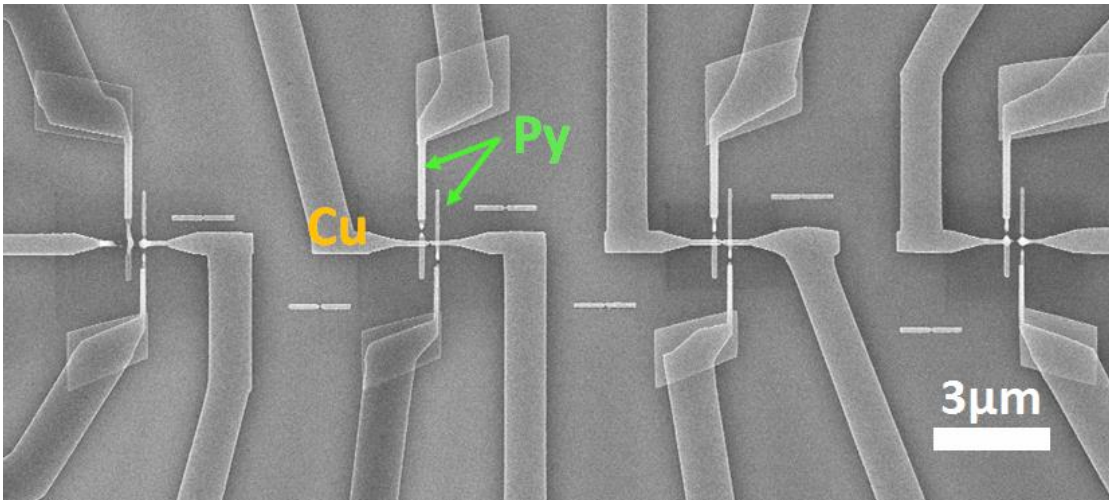

Figure 2. SEM image taken after the measurement process showing undesirable EM of the LSVs' FM electrodes.

Thinner electrodes, reduce the discontinuity of the overlapping Cu wire but also increase the current density within the Py making the FM electrodes more prone to unwanted EM effects. The Py electrodes have to outlive the Cu wire, so as to record the spin signal while Cu is elecrtomigrated. For our devices, a compromising value of 27nm was chosen for our Py electrodes. However, as seen in Fig. 2, even with the optimum thickness this was often not the case. Out of approximately 150 electromigrated LSVs only 10% survived more than two EM-NL measurement cycles and only 3% displayed NL signals after five EM steps. Of these, the longest surviving sample underwent 15 EM-NL measurement cycles.

5.3 Fabrication:

The fabrication of LSVs is performed by the lithography methods described in chapter 2. Once the substrate is cleaned, macroscopic contacts are patterned by optical lithography. Materialization entails a deposition of either titanium/gold (Ti/Au, 2nm/25nm), palladium (Pd, 30nm) or platinum (Pt, 15nm).

The LSV nanostructures were fabricated by a two-step EBL process. A double layer of PMMA resist (495A2/950A2) was used to create an undercut structure which assisted the lift-off process. The electrodes where deposited by e-beam (Py) and thermal (Cu) evaporation in an UHV system by CreaTec Gmbh with base pressure of about 10^{-9} mbar. Following the lift-off of the Py electrodes, a Cu strip was defined, overlapping the two Py electrodes.

Prior to the deposition of Cu, two argon (Ar) ion milling processes where performed, using an ion miller from *4-wave Inc.* The first milling was performed after the Py lift-off, at a grazing angle to the substrate surface. Its purpose was to remove horns, from the Py structure. A second milling process is performed after the development of the second Cu pattern. This process is performed to remove any PMMA residues and any oxide layer that may have formed on the underlying Py surface. This ensures a clean, electrically transparent contact at the Py/Cu interfaces. A summary of the fabrication process can be seen in Table 1:

Step	Procedure	Details
1	Substrate Preparation/Cleaning	As in Chapter 2
2	Definition of Macroscopic Contacts	As in Chapter 2
3	1st EBL Resist Coating	Double Layer 495A2/950A2 spun at 4000rmp for 1min and baked at 190°C for 1min.
4	1st EBL Patterning	FM electrodes and alignment marks. Accelerating Voltage = 10kV Beam Current = 20pA Dose = 150 μC/cm^2
5	1st EBL Development	Submerge into MIBK:IPA (1:3) for 1min. Then rinse in D.I. water and gently dry using N_2 gas.

6	Py Deposition	E-beam evaporation: Pressure< 1e-8mbar Beam Current = 44mA Rate = 0.8Å/s
7	Py Lift-Off	Submerge in acetone for at least 2 hours. Rinse in IPA and dry using N_2 gas.
8	1st Ar Ion Milling	Ar flow =15 sccm (standard cubic centimeters per minute) Acceleration Voltage = 50 V Beam Current = 50 mA Beam Voltage = 300 mV Time = 3min Angle = 10 degrees to substrate surface Rotation = 15rpm
9	2nd EBL Resist Coating	Double Layer 495A2/950A2 spun at 4000rmp for 1min and baked at 190°C for 1min.
10	2nd EBL Patterning	NM channel electrode. Both manual and automatic alignment procedures applied prior to exposure. Accelerating Voltage = 10kV Beam Current = 20pA Dose = 150 $\mu C/cm^2$
11	2nd Ar Ion Milling	Ar flow =15 sccm (standard cubic centimeters per minute) Acceleration Voltage = 50 V Beam Current = 50 mA Beam Voltage = 300 mV Time = 30sec Angle = 80 degrees to substrate surface Rotation = 15rpm
13	Cu Deposition	Thermal evaporation: Pressure< 1e-8mbar Crucible (Effusion Cell) Temperature = 1300K Rate = 2Å/s
14	Cu Lift-Off	Submerge in acetone for at least 20 hours. Rinse in IPA and dry using N_2 gas.

Table 1. Summary of fabrication procedure for lateral spin valves

5.4 Measurement Set-Up:

Lateral spin valves are a good platform for probing spin transport. Multiple electrodes can be used in several configurations to characterize charge and spin transport properties. Nevertheless, quantifying spin accumulation is not an easy task. Moreover, the low dimensionality of our devices limits their reproducibility and forbids the use of large currents. For this reason, characterization must be performed very carefully. Characterization of LSV was performed using the following measurements:

- 2-point Resistance
- Interface Resistance
- 4-point Resistance (Local)
- Non-Local Resistance

Electrical measurements were carried out in a PPMS cryostat (see Chapter 3) and employ DC currents and voltages. The measuring schemes are illustrated in Fig. 3.

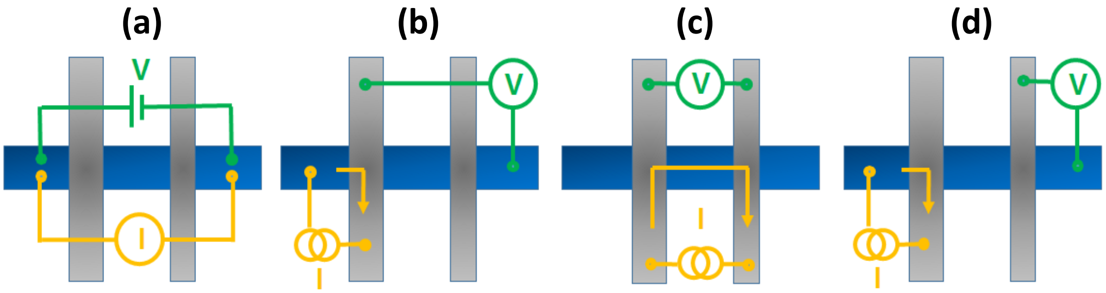

Figure 3. Measurement schemes for (a) 2-Point Resistance (b) Interface Resistance (c) 4-Point Resistance (Local) and (d) Non-Local Resistance

The 2-Point Resistance (2PR) measures the series resistance of the Cu channel and the macroscopic leads. This measurement applies a voltage and measures a current using two terminals (Fig. 3(a)). It is used during the EM process, where the FM electrodes should remain uninvolved. During this measurement the FM terminals are left at a floating voltage, meaning that they will not be connected to anything and will simply function as open circuits.

The interface resistance is a measure of the quality of the FM/NM interface. Two electrodes are used to inject current through an interface while another two electrodes are used to probe the voltage drop across it (Fig. 3(b)). By using four electrodes, the resistances and voltage drops across the electrodes are excluded from the measurement.

For 4PR/Local measurements we inject a current and measure the resulting voltage across the section of the Cu channel between the FM electrodes (Fig. 3(c)). The 4-Point Resistance (4PR) uses 4 terminals and measures the resistance of the Cu transport channel. This measurement is used to characterize the state of the spin valve channel and is particularly useful during the EM process. In addition using the relationship *R = ρL/A* (R is resistance, ρ is resistivity, L is Length and A is cross-sectional area), this measurement can be used to calculate the resistivity of the channel.

With the same configuration, an externally applied magnetic field can be used to switch the magnetization of the FM electrodes. Changing the FMs magnetization between a parallel and antiparallel magnetization gives rise to two distinct resistance states. This measurement represents the device's Local magnetoresistance (MR) which is defined as MR = $R_{AP} – R_P / R_P$.

Finally, Fig. 3(d) depicts the Non-Local (NL) configuration. Here, we use 4 terminals and inject current through one FM/NM junction while measuring the voltage across the other. The current flow between a material with a balanced spin DOS (NM) and a material with an imbalanced spin DOS (FM) gives rise to a temporary spin imbalance in the NM. Hence, this current leads to the temporary accumulation of excess same-spin electrons in the NM. The excess electrons diffuse equilaterally throughout the NM channel, following a spin concentration gradient. Given that the second FM is placed a distance L < λ away from the injection point, the presence of excess spins at the second interface can be detected as a small voltage across the second FM/NM interface (see Chapter 1). By sweeping a magnetic field, we can change the orientation of the detector electrode to be parallel or antiparallel to the injection electrode. Each case will give rise to an interfacial voltage of same magnitude but opposite sign. The voltage measured at the second interface divided by the current injected through the first interface is known as the NL resistance, $R_{NL} = \frac{V_2}{I_1}$. The difference in NL resistance between the parallel and antiparallel states is known as the NL signal, $\Delta R_{NL} = R_{NL}(\uparrow\uparrow) - R_{NL}(\uparrow\downarrow)$. An example of a NL measurement can be seen in Fig. 4.

5.5 Characterization:

5.5.1 Basic Spin Valve Characterization

The first step in characterization is to establish a standard of expected physical properties. The fabrication process is repeated several times and the resulting devices are compared. To have identical spin signals, we require that the following key parameters are replicated:

- Electrode Resistivity
- Interface Area
- Interface Resistance
- Channel Length

To compare the spin signal of our devices we use the NL measurements. Local measurements may also be used, but are not as reliable. Although local measurements give approximately twice the signal of NL measurements they are susceptible to spurious effects which can mimic spin accumulation [16] discrediting comparison between devices. Such effects arise mainly from differences in the angle between the externally applied magnetic field and the electrodes of the device (AMR and Hall effects).

For this work, the majority of spin transport measurements were performed using the NL configuration. Hence, unless noted, acquired spin signals will refer to those obtained in this way. The NL measurement is depicted as a plot of NL resistance against applied magnetic field. A typical NL measurement can be seen in Fig. 4.

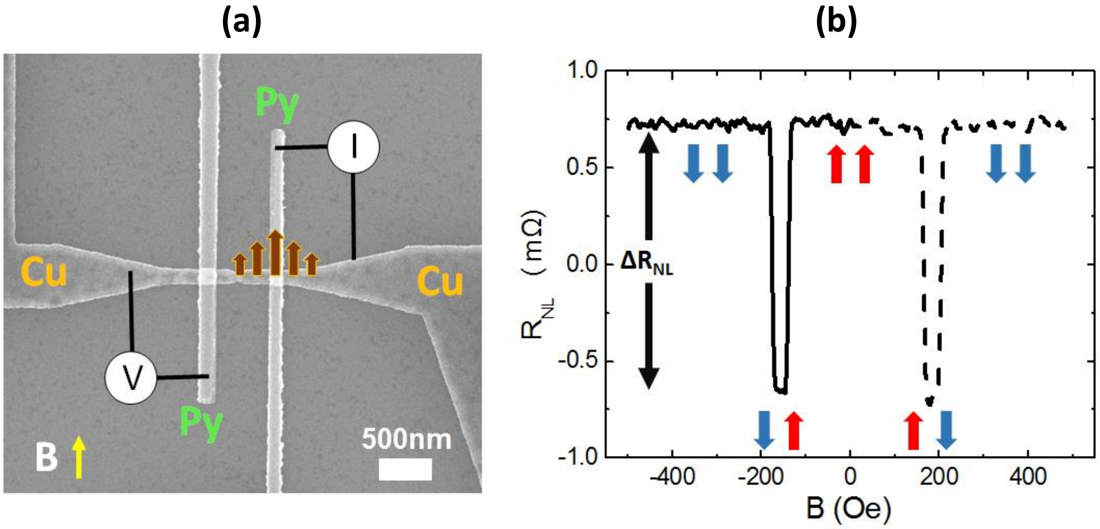

Figure 4. (a) SEM micrograph of LSV and illustration of NL configuration (b) NL measurement

In Cu (and most metals) the principle spin relaxation mechanism is Elliott-Yafet (EY) whereby the dephasing of spins is promoted by scattering events [102]. As a result the resistivity and the spin signal are inversely proportional. Hence, in our LSV devices, a decrease in the resistivity, whether from a decrease of the channels temperature or an increase in its crystallinity will result in longer spin lifetimes (large λ and τ_{sf}) within the system.

Fig. 5(a) displays the NL signal of a LSV at five distinct temperatures. As we lower the temperature ΔR_{NL} gets progressively larger. The temperature also produces changes in the FM coercivity and in the baseline of R_{NL} but these are irrelevant to our work. For this particular sample, the ΔR_{NL} was recorded to increase from 0.6mΩ at 300K to 1.76mΩ at 10K. Given that the conductivity saturates at 10K, further lowering of the temperature does not affect the NL signal. The decrease of the channel resistance (and resistivity) due to a decrease in temperature in shown in Fig. 5(b).

The increase in the spin signal at low temperatures and similarly the decrease of the spin signal at low dimensionality which we see later are both due to changes in the resistivity of the Cu channel. A reduction in temperature decreases the lattice vibrations and reduces the presence of phonons leading to less scattering within the metal [32, 244-246]. The characteristic temperature during our measurements was chosen to be 10K. Note that (fortunately) low temperatures provide a suitable environment for EM which is an essential aspect of our work.

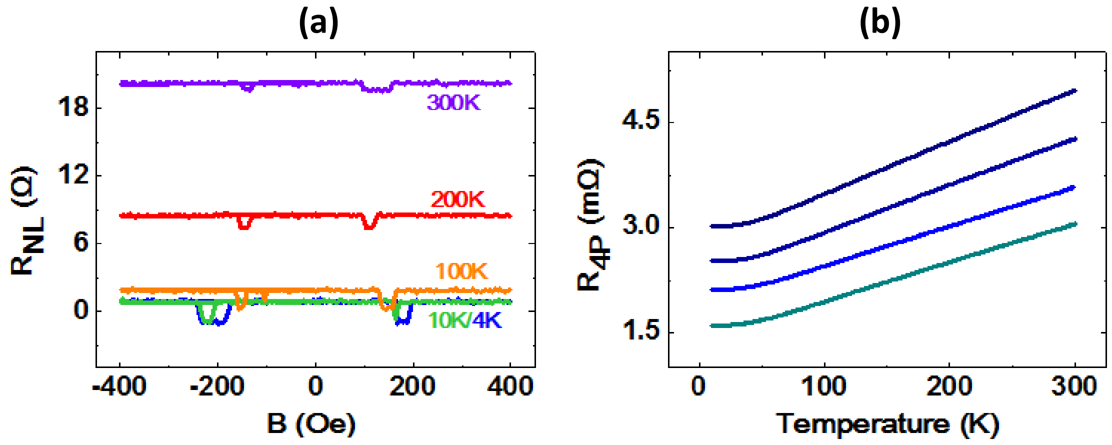

Figure 5. (a) NL signal at different temperatures. The ΔR_{NL} values are 0.6mΩ (300K), 1.08mΩ (200K), 1.55mΩ (100K) and 1.76mΩ (10K/4K) showing a clear increase of spin signals at low temperatures. (b) Channel resistance (4-point) between 10K and 300K for four distinct samples. The Cu resistivity decreases with temperature and saturates around 10K.

The simple correlation of spin conductance to resistivity can be taken a step further by introducing the concept of spin resistance, $\mathcal{R}_S = \frac{\rho\,\lambda}{A}$, where R_S is spin resistance, ρ is the resistivity, λ is the spin diffusion length and A is the cross-sectional area. Similar to the concept of electrical resistance, the spin resistance represents the resistance to the collective motion of spin populations. This relationship, highlights the effects of the geometry of the channel on the spin transport within it.

Before EM we characterized four distinct groups of devices. The average characteristic values are displayed in Table 1. As can be seen, the effect of the constriction is to increase the spin resistance of the channel. We see that increasing the channel length and introducing a constriction both decreased the resulting spin signals.

	Un-constricted		**Constricted**	
Channel Length (nm)	500	300	500	300
ΔR_{NL} (mΩ)	0,83	1,41	0,68	1,02
R_{4P} (Ω)	2,71	1,92	4,95	2,41

Table 2. Average characteristic spin signals of distinct groups of LSV

The dependence of the spin signal on the channel length and the constriction are expected [16, 247, 19, 248]. A large distance between the injection and detection points implies that the spin population generated will have more time over which to decay before reaching the detector.

The effect of the constriction is however different. A reduction of dimensionality can have two effects. One is to make scattering from the channels surfaces more prominent which leads to an increase of the resistivity [32]. Another is to decrease the cross sectional area. The second case incurs an increase in spin resistance which will inhibit the diffusion of the spin population towards the detector without increasing the scattering (represented by ρ and λ) within the channel. Although both effects may be present in such systems careful analysis can help weigh these two effects and shed light on the origin of the decreasing spin signal.

5.5.2 Competing Spin Transport Paths:

When spins are injected into the NM, they have three possible diffusion paths. One towards the detector, one away from the detector and one back into the FM. As in the case of electrical resistance, the mobile spins will choose to diffuse through the less (spin) resistive path. Similarly by tuning the relative spin resistance of each path or blocking access to the path, the excess spin population can be incited to prefer one path over the other.

A typical example of this effect is that of inserting tunnel junctions at the FM/NM interface. The outcome is the suppression of spin relaxation (i.e. increased spin signal) which is attributed to blocking the path of injected spins back into the FM [249-252].

In the same spirit, the diffusive nature of accumulated spins and the importance of the spin resistance, has also inspired some authors [20] to confine the entire channel between the injector and detector, so that the injected spins no longer have the option to diffuse away from the detector. Again, as spins are faced with no alternative path, they will all diffuse towards the detector causing a significant increase in the spin signal.

In an attempt to increase the spin signal obtained from our devices, and to explore the effect of shifting the relative spin resistance of each diffusion path, samples with confined channels and samples with tunneling interfaces where fabricated and measured.

For tunnel junctions, a 1.5nm Aluminum (Al) film was deposited after the second (interface cleaning) ion milling process. In order for the entire layer to be converted into oxide, the layer must be kept extremely thin [77, 253, 254]. Then, exposure of the sample to air (class 10000 cleanroom) for 30min, causes a natural oxidation of the Al layer and transforms it into aluminum oxide Al_xO_Y. Note that in this case the Cu channel is then grown on an Al_xO_Y surface instead of a SiO_2 surface which can result in the deposited film to obtain a different grain structure and ultimately a different resistivity. Indeed, in this case, Cu channels grown on Al_xO_Y show a slightly higher resistance.

Despite the expectation of a more resistive channel giving rise to a smaller spin signal, the inclusion of the tunnel junction blocks the backflow into the injector electrode causing a significant increase in the detected signal. Unfortunately, producing an ultra-thin (1.5nm) uniform oxide layer is very challenging and the reproducibility of LSV with tunnel junctions is significantly lower. For this reason, the method was not pursued any further.

Confined channels also complicate fabrication. In this case instead of a long wire overlapping two Py electrodes, the Cu channel must be patterned to end exactly at the edges of the FMs. This design, leaves no space for misalignment of the two (Py and Cu) patterns. To ensure the successful fabrication of these samples, the Cu channel is designed to exceed the edges by 30nm on each side and the alignment is done with extreme care. The exposed pattern is concentrated to a small area in the center of the samples and after the manual set up is complete, we perform a series of automatic alignment processes (layer 61, layer 63) available in the RAITH software package. The automatic layer scans a location close to where we wish to pattern and detects alignment structures which have been exposed during the Py patterning. These are then used as a reference for the placement of the overlaying Cu pattern.

In confined channels, NL measurements cannot be performed, so Local measurements are used instead. Typically, the local signal is expected to be twice that of the NL ($\Delta R_{Local} = 2 \times \Delta R_{NL}$) and although discrepancies from this relationship are often observed they are usually negligible [255, 14, 243]. The obtained results can be seen in Table 2.

Measurement Type	**Measured Spin Signal (mΩ)**	**Channel Resistance (Ω)**
Non-Local	1.41	1.92
Local Confined	4.80	2.27
Non-Local (Tunnel Junction)	7.73	3.18

Table 3. Spin signals for standard samples, confined samples and tunnel junction samples

In accordance with previous findings [255, 20, 256, 241], the confinement of the channel produces approximately a factor of two increase from the local signal (factor of 4 from the NL). The inclusion of tunnel junctions yields the largest signal by far, despite the slight increase in the channel resistance. Unfortunately, due to the decreased reproducibility introduced by the extra fabrication steps the confined channels and the tunnel junction interfaces were deemed unfit for our work and not pursued any further. Instead, to further explore the relationship between dimensionality and spin transport we proceed to EM devices with constricted channels and follow the evolution of the spin signals during the (localized) variation of our channel width.

5.6 Electromigration of Constricted Lateral Spin Valves

5.6.1. Characterization:

As we have seen, in our Cu channel, spin transport occurs diffusively and spin relaxation is promoted by scattering events in accordance to the EY mechanism. We have seen that augmented spin resistance impedes spin diffusion in a given direction and that augmented resistivity accelerates spin de-coherence within a NM. To further explore this relationship, we perform EM in the Cu channel and monitor the spin signal of the device, as the channel is transformed. To ensure that the transformation takes place in the center of the channel, we use devices which have been constricted (not confined) by EBL. The constriction will result in an augmented current density, making it the most likely position for EM to take place.

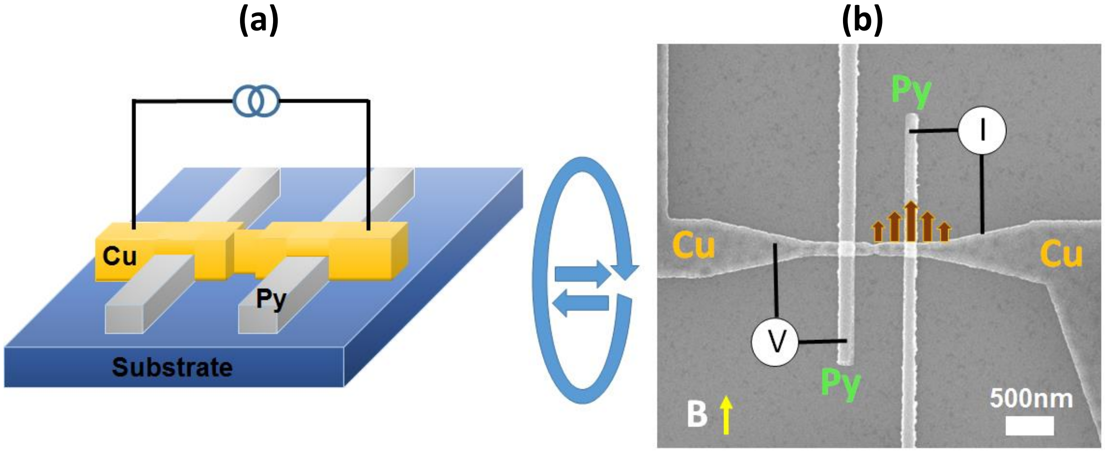

Figure 6. (a) Configuration for EM. (b) NL measurement configuration. After each EM step the NL measurement probes the spin transport across the electromigrated channel. The process is continually repeated, until spin accumulation can no longer be detected.

During EM, a steadily increasing voltage is applied across the Cu nanowire while the 2-point resistance (R_{2P}) is continuously measured. An abrupt increase in resistance (end of voltage ramps in Fig. 7(a)), indicates a transformation of the Cu channel. This transformation results in a reduction in the wire's cross sectional area at the point of EM [257]. An active feedback condition allowed us to constrict the Cu channel in small, gradual steps so as to observe the evolution of the spin signal due to slight changes occurring at the constriction. After each EM step, the Cu channels' resistance R_{4P} and the NL signal measurements were repeated. As expected, each EM step caused an increase in the channel resistance accompanied by a decrease in ΔR_{NL}. By repeating this process, we were able to follow the decay of the NL signal until it disappeared.

By carefully monitoring the device after each EM step, we noticed that during the process some samples underwent slight changes of the interface resistance. Despite the occurrence of such changes being rare, we inferred that such changes appeared in devices which had high interface resistance to begin with, and whose constriction was closer to either of the interfaces. The noted changes occurred independently in each interface implying that the cleanliness of the interface and the effective junction area might be related to the change. The resulting changes where both increasing and decreasing and where always significantly more subtle than the changes occurring in the constriction. Samples with large changes in the interface resistance were excluded from further analysis.

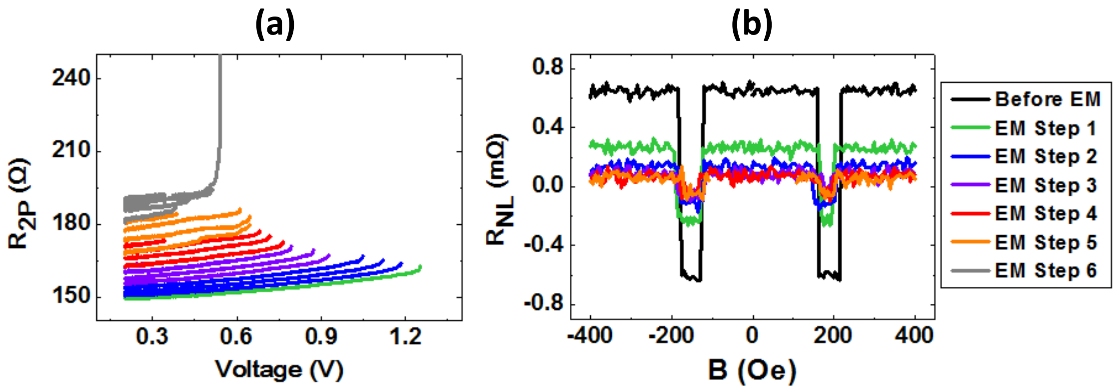

Figure 7. (a) EM of LSV Cu channel in small controllable steps. When an abrupt change in resistance is detected the voltage ramp is ended via a feedback mechanism and a new voltage ramp begins. (b) NL Signal of LSV with L=300nm at various stages of the EM process.

Although the main result of EM is the reduction of the size of the constriction, the large current density required is often associated with an appreciable amount of Joule heating. While the reduced dimensionality increases the channels resistivity, the increased heating can cause it to decrease. If sufficient heating is generated to cause structural transformations of the wire, a current annealing can take place. In some studies, heating is associated to increases of the grain size, which consequently reduces the amount of grain boundaries, grain boundary scattering and resistivity in the wire [152, 258, 27]. Unfortunately, although changes in resistance are observed and changes in resistivity are expected, a distinction between these two effects cannot be made.

As can be seen in Fig. 7, each EM step resulted in a slightly lower NL signal. For our samples the spin signal disappeared after a resistance change of only about 40Ω and therefore the necessity for highly controlled EM was crucial. Although the process is generally known to decrease the size of a constriction, it is possible for a particular EM process to increase the width of the constriction or even revert the wire to its original state [257, 259]. One of the most striking features of this experiment was the observation of such reversibility. In the (very) few cases that this was observed the NL signal reverted to a value corresponding to the resistive state and the lost spin signal was recovered.

Using careful EM of LSVs, we can obtain access to distinct spin transport regimes within a single device. So far, our experiment confirms the relationship between the channel resistance and the detected spin accumulation. Taking this a step further we decided to fit the decay of ΔR_{NL} to that of the one-dimensional (1D) spin diffusion model and see if we can extract information about the spin transport properties (α_F, λ, τ_{sf}) of the device.

Given that our wire is narrow and long and the interface resistance R_i is negligible ($R_i << R_F$, R_N, where R_F and R_N are the resistances of the FM and the NM respectively), the spin transport was modelled by the 1D spin diffusion model for transparent contacts. In this framework, the NL signal can be expressed as [14, 15]:

$$\Delta R_{NL} = \frac{4R_N\left[\alpha_F \frac{R_{SF}}{R_{SN}}\right]^2 e^{-\frac{L}{\lambda_N}}}{\left[1+\frac{2R_{SF}}{R_{SN}}\right]^2 - e^{-\frac{2L}{\lambda_N}}} \tag{1}$$

where L is the edge-to-edge distance between the FM electrodes, α_F is the spin polarization of the FM, $R_{SN} = \lambda_N\rho_N/t_Nw_N$ and $R_{SF} = \lambda_F\rho_F/w_Nw_F(1-\alpha_F^2)$ are the spin resistances, t_N is the thickness of the NM, and $\lambda_{N,F}$, $w_{N,F}$ and $\rho_{N,F}$ are the spin diffusion lengths, the widths, and the resistivities of the NM and the FM, respectively.

While the majority of work on modelling spin valves has been done by fitting for a variety of different channel lengths [16-20], we adapt the above equation to our geometry and remodeled it so as to fit for various channel resistances. Substituting ρ_{Cu} by $A_{Cu}R_{Cu}/L_{Cu}$ and using the expanded spin resistance expressions we arrive at [260, 18]:

$$\Delta R_{NL} = \frac{4\,\alpha_F{}^2\,\lambda_{Cu}\frac{Rcu}{L}}{\left(2+\lambda_{Cu}\,R_{Cu}\frac{w_{Py}\,w_{Cu}(1-\alpha_F{}^2)}{\lambda_{Py}\,L\,\rho_{Py}}\right)^2 e^{\frac{L}{\lambda_{Cu}}} - \left(\lambda_{Cu}\,R_{Cu}\,\frac{w_{Py}w_{Cu}\,(1-\alpha_F{}^2)}{\lambda_{Py}\,L\,\rho_{Py}}\right)^2 e^{-\frac{L}{\lambda_{Cu}}}} \tag{2}$$

where R_{Cu} represents the 4-point resistance of the Cu channel. Note how the resistivity of the Cu channel is replaced by the resistance for the Cu channel (ρ = RA/L). Given the changing geometry of the constriction it is hard to estimate the resistivity of the wire after each EM step. However, with the equation in this form, the resistance includes any changes in resistivity allowing a fitting to be carried out. The device dimensions were obtained from scanning electron microscopy (SEM) images. In Fig. 8(a) we see the data gathered during the EM-NL measurement cycle of a sample with L=500nm. In Fig. 8(b) we have plotted the recorded ΔR_{NL} against the channel resistance and the fitting of the acquired data to Equation (2). While keeping all other parameters fixed, we simultaneously fit the spin polarization, α_F and the spin diffusion length λ. The obtained values are sensible and the fit of good quality (R>0.998). Assuming λ_{Py} = 5 nm [261, 262], we find α_{Py} = 41% ± 2.3% and λ_{Cu}=451 nm ± 167 nm.

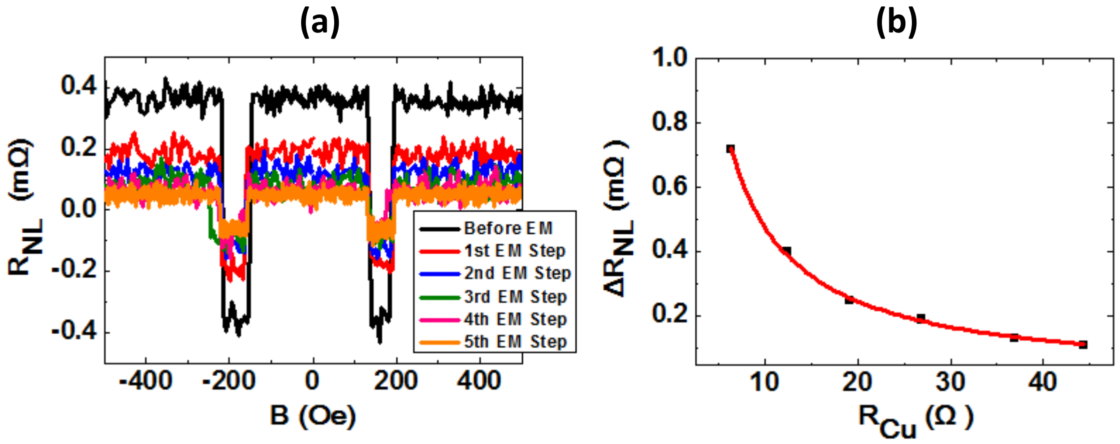

Figure 8. (a) Non-local resistance, measured at 10 K, as a function of the magnetic field after each EM step of the Cu channel. (b) Spin signal, obtained from the measurements in (a), as a function of the resulting 4-point Cu channel resistance after each EM step. Red line is a fit to the one-dimensional spin diffusion equation

Instead of using a series of devices with varying L, in the current approach, the relevant parameters can be extracted from a single device. Hanle measurements, can also be used to this end [15], but are very sensitive to device details and their liability has been put into question [263-265]. Using EM on a single device provides an advantage as sample-to-sample variations do not play a role. Furthermore, as we will see in the next section, careful analysis of our results can give us additional information about the spin dynamics within the Cu channel.

5.6.2. Analysis:

From fitting our data, we find that the device can be described by a single spin diffusion length. However, given that our channel comprises of regions with distinct and dynamic resistances, one might expect a distribution of spin flip scattering regions to appear within the channel. To further understand the spin transport in our device we proceed to carefully parametrize our device and simulate the spin accumulation within the channel. This work was performed using the SpinFlow3D software in collaboration with Goran Mihajlovic, an external member of our team. For the simulations the channel is considered to comprise of 3 sections: two being the edges of the Cu channel and having the same resistivity (resistance), and one being the constricted section, which has a distinct and variable resistivity (resistance). The 4-point channel resistance is then considered to comprise of the series resistance of these three sections. Measurements on independent samples reveal that for a Cu nanowire with the dimensions of the edge section the resistivity is 2.2μΩcm [17]. The resistivity of the constriction is estimated in a slightly more elaborate manner.

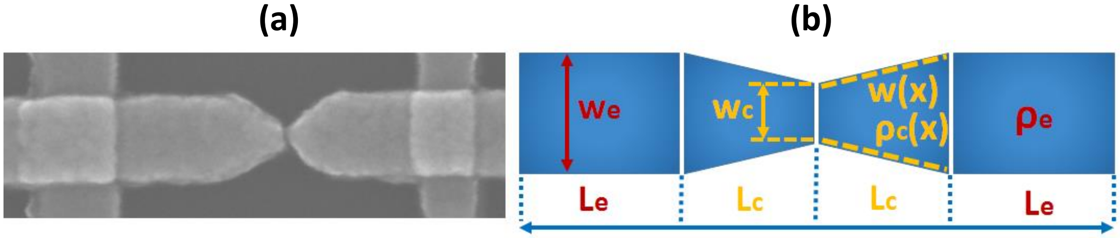

Figure 9. (a) SEM image of 500nm long constricted channel. Image was taken after measurements and constriction has already been electromigrated. (b) Model of channel segmentation for analysis

Along the axis of the Cu channel, we assume the channel width to vary linearly from the width at the edges to the width of the constriction. Hence the variable width of the channel can be written as a function of the position in the channel:

$$w(x) = w_e + \frac{w_c - w_e}{L_C} x \tag{3}$$

The resistance is now taken to be the series resistance of the individual resistance of each section illustrated in Fig. 9(b). Hence we can write the total (4-point) channel resistance as:

$$R_{tot} = 2R_e + 2R_c = 2\frac{\rho_e L_e}{t w_e} + 2\int_0^{L_c} \frac{\rho_c(x)}{t w(x)} dx \tag{4}$$

where ρ is the resistivity, L is the length, t is the thickness, w is the width and the subscripts e and c represent the edge and constricted sections respectively. The premise here, is that the resistivity varies linearly as a function of the channel width. Size-dependent resistivity has been clearly demonstrated in Cu nanowires and as we will see agrees perfectly with our results [266, 30, 32]. The width-dependent resistivity throughout the channel can be expressed as ρ(x) = A + B/w(x), where A and B are constants. Using the boundary conditions ρ(0) = 2.2μΩcm and R_{tot} = 6.4Ω (from our measurements), we are able to solve for A and B and with this a complete parametrization of the device can be implemented. The above equations allow the channel resistance measured after each EM step to be related to a specific size of constriction.

EM Stage	Measure R_{4P} (Ω)	Calculated Constriction Size (nm)
Before EM	6.4	70

EM Step 1	12.4	43.4
EM Step 2	19.1	31.1
EM Step 3	26.9	23.7
EM Step 4	36.9	18.3
EM Step 5	44.3	15.8

Table 4. Measured Channel Resistance and Corresponding constrictions sizes during the EM-NL measurement cycle

Using SpinFlow3D, we can now simulate a NL measurement configuration and extract the spin accumulation at every point along the Cu channel. Using the spin diffusion length found and the variable resistivity model the simulations agree well with our results.

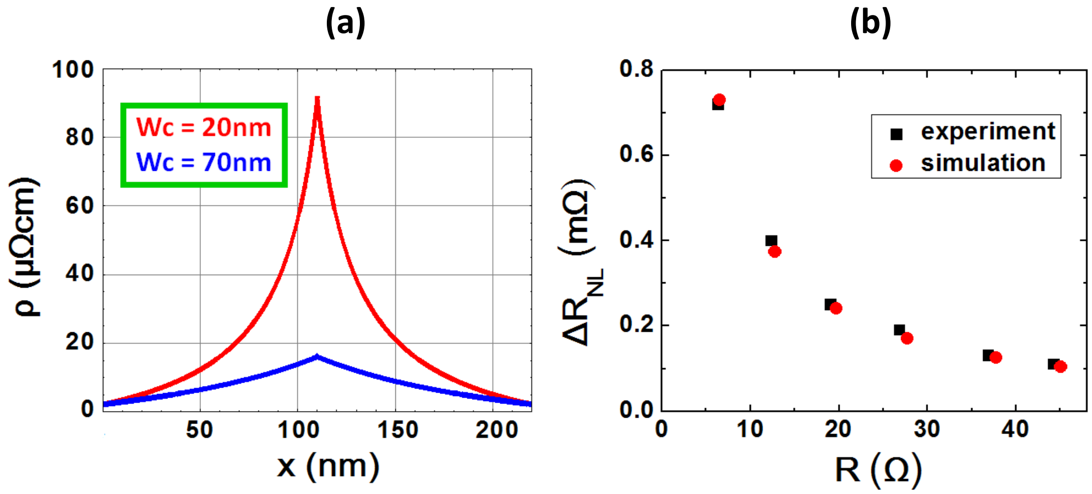

Figure 10. (a) Variation of resistivity in constricted region for 20nm constriction (red) and 70nm constriction (blue). Locally the ρ of the constriction can reach several tens of μΩcms. (b) Experimental data and simulated NL signal using λ=451nm and the variable ρ model described above. Agreement is very good.

We see that despite the local variation in resistivity of our device, the transport can indeed be described using a single λ. Previous work in our group has shown that for un-constricted Cu channels in similar devices, λ is approximately 500nm [17]. Given that λ should be inversely proportional to ρ, and that locally the resistivity can increase by a factor of 40 (Fig. 10(a)), one could expect to find a significantly lower λ from the fittings. To understand this phenomenon, we consider the two main effects of the constriction. Primarily, to increase the resistivity and secondly to create a bottleneck which blocks the injected spins from getting to the detector side. Note how the first effect is related to scattering within the wire while the second is simply blocking the path of spin diffusion. With this in mind, a large λ implies that the main effect of the constriction is the second one, and a significant increase in scattering does not take place. Hence even though fewer electrons cross the constriction, the number of scattering events within the wire does not increase dramatically. In Fig. 11 we see the simulated spin dependent chemical potential V_S, arising from a current I_{Inj} injected at FM1/Cu interface when the FM electrodes are in a parallel magnetic orientation. This simulation allows the visualization of the resulting spin accumulation at each point throughout the channel. On the left side of the injection point (FM1) we see that the accumulated spins decay exponentially as expected of an un-constricted channel. On the right side, we see the effect of the constriction which results in a different distribution of the spin population.

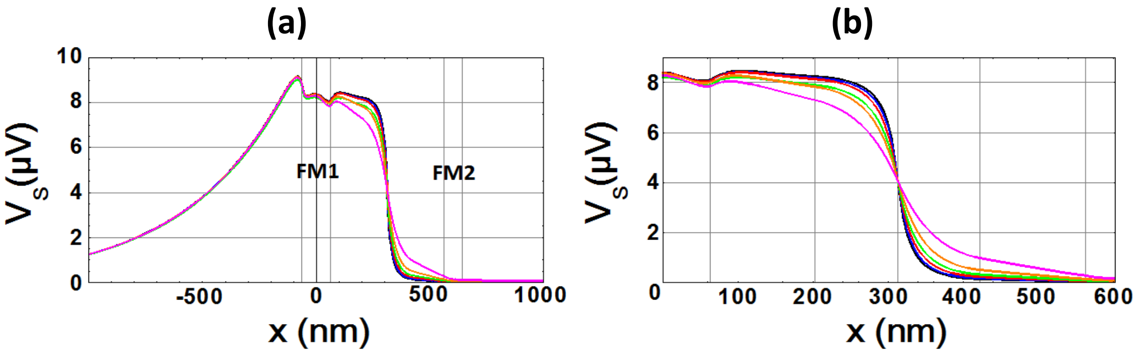

Figure 11. (a) Spin accumulation voltage due to current injection at FM1 (x=0) for different constriction sizes: 70nm (pink), 43.3nm (orange), 31.1 (green), 23.7nm (red), 18.3nm (blue) and 15.6nm(black). (b) Zoom of (a) at point of constriction.

On the constricted side, the spin accumulation is maintained fairly level until the point of the constriction which results in an increased spin accumulation compared to its un-constricted counterpart. In addition, this effect is inversely proportional to the size of the constriction. The effect of the constriction is clearly to block the accumulated spins and contain them on one side of the constriction. Given the dominance of the EY mechanism in Cu, the augmented signal implies that there is no additional spin flip scattering in this region.

Note that the decrease in the signal at the constriction signifies the absence of a spin population in that region. However, there is no evidence of this absence being due to spin flip evets. Given the high spin diffusion length obtained, the most reasonable explanation appears to be that the constriction causes a backflow of the spin population rather than an inversion of the electron's spin type.

Further analysis allows the estimation of the spin flip probability within the channel, which is defined as the ratio of the momentum scattering time, τ_e, divided by the spin flip scattering time, τ_{sf}. For this calculation we will use the following two expressions [267, 109]:

$$\tau_{sf} = \frac{{\lambda_{Cu}}^2}{D} \tag{5}$$

$$\tau_e = \frac{3D}{v_F^2} \tag{6}$$

where $D = \frac{1}{N(E_F\,)e^2 \rho_{Cu}}$ is the diffusion constant, N(E_F)=1.8×10^{28} states/eVm^3 is the density of states of Cu at the Fermi level [243], v_F is the Fermi velocity (1.57×10^6 m/s for Cu) [243, 268] and *e* is the charge of the electron. Using the edge resistivity, we find τ_e=19.2fs and τ_{sf}=12.9ps which results in a spin flip probability of a_{sf}=14.9×10^{-4}. This value is comparable to those expected for Cu [17, 243] implying that the edge section is largely responsible for the spin coherence properties within the channel, and the constriction is in this respect irrelevant.

We have seen that despite the localized increase in resistivity, the spin properties of our device seem to be more closely related to those of the un-constricted channel. Nevertheless, the effect of the constriction is clearly visible both in the measured NL signal and in the simulations of spin dependent chemical potential. Hence using our method and probing the reaction of diffusing spin populations to channel protrusions, we can characterize the spin transport properties using a single device.

Chapter 6:

Conclusions & Outlook

6.1 Introduction:

The trend of continuous miniaturization has augmented the importance of quantum mechanical effects in electronic devices and has left the industry faced with a need for conceptually new devices. The premise of our work has been to explore fabrication methods and device structures which can contribute to the problems of device miniaturization. In this light, we fabricate lateral nanoscale devices which allow us to study the charge and spin transport in sub-10nm conductive structures. Furthermore we look at charge transport through assemblies of molecules and spin transport in spatially constricted metallic channels. In this chapter we discuss the key findings of each chapter and present perspectives for a continuation of our work.

6.2 Conclusions:

After presenting a theoretical background, we focus on nanofabrication. We look at lithography as a general purpose fabrication technique and see how each of the steps involved can have a crucial effect on the final resolution. Lithography consists of two major phases, which are the patterning phase and the materialization phase. During patterning the process suffers from the proximity effect, which makes our fabrication geometry dependent. The materialization phase defines the layers roughness and structural integrity which implies that the outcome of the resulting structures will depend on the material used. As our device features approach those of the material’s grain size and the resist profile’s slope, this limit is often related to the geometry and the materials used for our devices.

Extending our focus to these limits, we concentrate on three methods employed to create nanogap devices. While tunnel junctions are successfully created, control over sub-10nm features remains elusive. Using EBL, and repeating the fabrication process, the design is optimized so as to increase the number of tunnel junctions resulting. EM is applied using a feedback loop which allows a level of control according to certain conditions. While transformations in the low resistance regime can occur quite smoothly, the complete transformation of a wire into two distinct electrodes, requires transformations at a high resistance whose explosive nature impedes the level of control. Finally, we examine the Overhang method. This method requires a highly selective etching process and is subject to a trade-off between the ease of lift-off and the size of the obtained nanogap. While EBL is the simplest in terms of fabrication, EM allows us to observe distinct conductance mechanisms within a single wire and the Overhang method allows for large-aspect ratio gaps. However, while each method is better suited for distinct applications, all three methods are strongly related to the materials and geometries applied.

Once we have created our nanogap devices, we shift our attention towards their electrical transport properties. Characterization of tunnel junctions is typically performed by fitting measurements to theory and extracting the relevant barrier parameters. The theoretical description of this mechanism ignores several important aspects of tunneling in real devices, such as the distribution of barrier height and electrode separation which arise due to electrode edge roughness. In addition, the fitting of multiple parameters is susceptible to multiple minima, which demands the process be carried out with care. Using the Simmons model, we measure our devices over a range of temperatures and demonstrate how the parametrization of the fit can alter our understanding of the tunneling behavior. Given the absence of the temperature dependence in tunneling theory, we propose a transformation of the barrier due to thermal expansion effects.

Later on, we look at the presence of nanoparticles in our nanogap devices. These nanoparticles arise naturally as residues from the fabrication process and have been observed using all three of the fabrication methods. Although we have no control over their presence, it allows for the study of single electron phenomena and gives testimony to the ability of EBL, EM and the Overhang method to create SET devices. Stability diagrams of such devices allow us to understand the nature of these particles and their coupling to the electrodes. In this way we see that the trapping of single but also multiple particles can arise and that particles can be sufficiently small and exhibit sufficiently large charging energy to achieve room temperature operation.

Finally our nanogap devices are used to study charge transport through carbon-based molecular semiconductors. We see that transport in such devices can take many forms and that changes between dominant transport mechanisms can be incited by variations of temperature and applied bias. The application of a gate voltage allows us to observe the semiconducting nature of such molecules which give rise to the n-type behavior of C60 and the p-type behavior of Pc. We demonstrate that n-type behavior in C60 is maintained even when using Pt electrodes which in a rigid band approximation are placed 0.1eV from the HOMO and 2.1eV from the LUMO. Although the rigid band energy levels are approximate, this implies that large interface dipoles can arise in such devices.

Further, we see that molecular devices are susceptible to partially reversible changes which can alter their transport characteristics. These transformations can be onset by simple measurements and are associated to changes in conductivity, bias symmetry and the device’s response to the gate voltage. In addition, we present the unexpected observation of non-monotonic gate modulation in a C60 device with large electrode separation. This effect inspired us to measure transport at low temperatures which revealed transport characteristics reminiscent of Coulomb Blockade.

In the final part of this thesis, we look at lateral spin valves, which are used to transfer spin-polarized charge currents and pure spin currents and give additional functionality to electronic devices. In LSV the nanoscale dimensionality is a crucial requirement and both the fabrication and the measurement must be done with extreme care. Signals of spin accumulation appear at the FM/NM detector interface as a potential difference of a few nV (10^{-9}V) making the maximization of the signal-to-noise ratio crucial.

We present the effects of temperature and distinct spin resistances on the detected spin accumulation in these devices. Then, using EM, we are able to progressively constrict the spin transport channel and cause a modulation of the non-local signal. By fitting our results to the one-dimensional spin diffusion model, we extract and analyze the spin transport properties. In this way we present a novel method of spin valve characterization, which can be applied using a single device.

Despite a local increase in resistivity, the extracted spin diffusion length, λ, of progressively constricted channels is comparable to that of non-constricted channels. Careful parametrization of our device, allows us to extract the size of the constriction after each EM step and using this information we can simulate the spin accumulation in our devices. The simulations are in perfect agreement with our measurements and confirm that the constriction of the channel causes a blocking of spin diffusion rather than an increase of scattering events.

6.3 Outlook:

Our work on fabrication helps us identify some crucial aspects which could be addressed to increase the control over sub-10nm features. At these dimensions the optimization of each method must be specific to given geometries and materials. Future research could focus on creating straight large-aspect ratio resist profiles, controlling the structural properties of deposited materials and eradicating roughness from resulting structures. To this end, EBL could be attempted with increased accelerating voltages and distinct resists. Furthermore, by carefully studying the deposition of materials, one could explore the correlation between grain size, roughness and strain produced using common materials. These properties could then be related to lift-off parameters and possibly associated to the resulting edge roughness arising in metallic structures. With this knowledge the Overhang and the EM methods could be optimized as well. To extend the controllable EM regime, we require to decrease the breaking voltage for wires exhibiting high resistance. An interesting study to this end, would be to examine the relationship between grain size, thermal conductivity and critical current density.

Decreasing the electrode edge roughness of lateral tunnel junctions would make the characterization of these devices by fitting to the Simmons model more appropriate. However, using our analysis, characterization could also benefit from the understanding and precise monitoring of thermal expansion effects. Simulations of thermal expansion effects could be carried out with software such as COMSOL allowing an understanding of the geometrical changes taking place during a variation of temperature. If the variation of the electrode separation could be known without fitting, a more accurate study of the resulting barrier height and tunneling area could ensue.

The study of single electron phenomena could be extended by purposefully depositing nanoparticles. While this is often done chemically, an easier method to attempt would be to evaporate a sub-1nm film onto the surface which for several metals results in the formation of isolated metallic nanoclusters. With a larger yield of SET devices we could focus our work on increasing the reproducibility of such devices.

Further into the thesis, we use our nanogap devices to study transport through assemblies of molecules and find that transformations of the molecular layer incite changes of conductance resembling Coulomb Blockade. To explain this observation we propose the formation of conductive carbon-based quasi-one-dimensional wires arising within the C60 layer. To better understand this observatino, experiments could attempt to replicate this phenomenon in distinct devices with varying channel geometries. Furthermore, techniques such as transmission electron microscopy (TEM) imaging could be employed to identify and better understand structural changes within the layer.

Finally we fabricate, characterize and elecromigrate lateral spin valves. Here, the difficulty of the experimental procedure inhibited further progress. Future work could attempt to optimize the devices and even employ alternative designs. Acquiring a significantly larger signal and using more robust devices, would allow a larger variation of the spin signal in a longer and more isolated channel. Alternative designs, could employ multiple constrictions and constrictions outside of the spin transport channel. Alternative materials could have Al replacing Cu and $Co_{60}Fe_{40}$ replacing Py. Al has previously been used for EM, has a large spin diffusion length and grows a natural oxide coating which can be used as a tunneling interface [267, 269, 270]. $C_{60}Fe_{40}$ has a much larger spin polarization and has recently been demonstrated to result in significantly larger spin signals [271].

Throughout our work we have explored the fabrication and characterization of nanoscale devices. While reliability and reproducibility are crucial to commercialization we have seen that a better understanding of the field can be pursued, even in their absence. Studying such devices opens new possibilities for device structures and promises additional functionality to standard electronics.

References

[1] D. Natelson, "Towards the Ultimate Transistor," IOP Publishing Ltd , 2009.

[2] M. Urdampilleta, S. Klyatskaya, J.-P. Cleuziou, M. Ruben and W. Wernsdorfer, *Nat. Mater.,* vol. 10, pp. 502-506, 2011.

[3] A. Aviram and M. A. Ratner, *Chem. Phys. Lett.,* vol. 29, p. 277–283, 1974.

[4] S.-H. Lee, H. Lee, T. Jin, S. Park, B. J. Yoon, G. Y. Sung, K.-B. Kim and S. J. Kim, *Nanoscale,* vol. 7, p. 936, 2015.

[5] M. Fuechsle, J. A. Miwa, S. Mahapat, H. Ryu, S. Lee, O. Warschkow, L. C. L. Hollenberg, G. Klimeck and M. Y. Simmons, *Nature Nanotechnology,* vol. 7, pp. 242-246, 2012.

[6] V. V. Zhirnov , R. K. Cavin, J. A. Hutchby and G. I. Bourianoff, *Proc. IEEE,* vol. 91, p. 1934, 2003.

[7] J. D. Meindl, Q. Chen and J. A. Davis, *Science,* vol. 293, p. 2044, 2001.

[8] J. D. Meindl, *Proc. IEEE,* vol. 83, p. 619, 1995.

[9] L. Bogani and W. Wernsdorfer, *Nature,* vol. 7, pp. 179-186, 2008.

[10] J. G. Simmons, *J. Appl. Phys.,* vol. 34, no. 6, p. 1793, 1963.

[11] J. M. Beebee, B. Kim, J. W. Gadzuk, C. D. Frisbie and J. G. Kushmerick, *Phys. Rev. Lett.,* vol. 97, p. 026801, 2006.

[12] J. H. Worne, J. E. Anthony and D. Natelson, *Appl. Phys. Lett.,* vol. 96, p. 053308, 2010.

[13] E. Villamor, "Phd Thesis, "Injection, transport and manipulation of pure spin currents in metallic lateral spin valves"," NanoGUNE, San Sebastian, 2014.

[14] A. Fert and S.-F. Lee, *PRB 53,* vol. Vol 10, no. 6554, 1996.

[15] S. Maekawa and S. Takahashi, *Phys. Rev. B,* vol. 67, p. 052409, 2003.

[16] F. J. Jedema, A. T. Filip and B. J. van Wees, *Nature,* vol. Vol.10, pp. 345-348, 2001.

[17] E. Villamor , M. Isasa, L. Hueso and F. Casanova, *Phys. Rev. B,* vol. 87, no. 094417, 2013.

[18] T. Kimura, J. Hamrle and Y. Otani, *Phys. Rev. B,* vol. 72, no. 014461, 2005.

[19] H. Idzuchi, S. Karube, Y. Fukuma, T. Aoki and Y. Otani, *Appl. Phys. Lett.,* vol. 103, p. 162403, 2013.

[20] P. Laczkowki, L. Vila, V.-D. Nguyen, A. Marty, J.-P. Attane, H. Jaffres, J.-M. George and A. Fert, *Phys. Rev. B,* vol. 85, no. 220404, 2012.

[21] "http://www.nobelprize.org/nobel_prizes/physics/laureates/1956/".

[22] G. E. Moore, *Electronics,* p. 114–117, 1965.

[23] R. H. Dennard, F. H. Gaensslen, H.-N. Yu, V. L. Rideout, E. Bassous and A. R. LeBlanc, *IEEE JSSC,* vol. 9, no. 5, pp. 256-268, 1974.

[24] "http://www.computerhistory.org/semiconductor/timeline/1947-invention.html".

[25] R. Courtland, *IEEE Spectrum,* vol. 50, p. 26, 2013.

[26] I. Stone, *Phys. Rev.,* vol. 6, no. 1, 1898.

[27] A. F. Mayadas and M. Shatzkes, *Phys. Rev. B,* vol. 1, no. 4, pp. 1382-1389, 1970.

[28] C. W. J. Beenaker and H. van Houten, *Solid State Physics,* vol. 44, pp. 1-228, 1991.

[29] K. Fuchs, *Proc. Cambridge Philos. Soc. ,* vol. 34, pp. 100-108, 1938.

[30] W. Steinhogl, G. Schindler, G. Steinlesberger and M. Engelhardt, *Phys. Rev. B,* vol. 66, p. 075414, 2002.

[31] A. B. Pippard, Magnetoresistance in Metals, Cambridge: Cambridge University Press, 1989.

[32] D. Josell, S. H. Brongersma and Z. Tokei, *Annu. Rev. Mater. Res.,* vol. 39, p. 231–54, 2009.

[33] C. Durkan , M. A. Schneider and M. E. Welland , *J. Appl. Phys.,* vol. 86, no. 3, p. 1280–6, 1999.

[34] B. J. van Wess, H. van Houten, C. W. J. Beenakker, J. G. Williamson, L. P. Kouwenhoven, D. van der Marel and C. T. Foxon, *Phys. Rev. Lett.,* vol. 60, no. 9, pp. 848-850, 1988.

[35] M. Baldo, "Introduction to Nanoelectronics, Part4:Two Terminal Quantum Wire Devices,," MIT Open Course Ware.

[36] R. Landauer, *IBM J. Res. Dev.,* vol. 1, pp. 223-231, 1957.

[37] R. Landauer, *Phys. Lett.,* vol. 85A, p. 91, 1981.

[38] N. Zabala, "Introduccion a la Physica de Systemas Mesoscopicos," EHU, San Sebastian, 2007-2008.

[39] M. Razavy, Quantum Theory of Tunneling, Singapore: World Scientific Publishing Co. Pte. Ltd, 2003.

[40] S. M. Sze and K. K. Ng, Physics of Semiconductor Devices, New Jersey: John Wiley & Sons, Inc., 2007.

[41] R. H. Fowler and L. Nordheim , *Proceedings of the Royal Society A,* vol. 119, p. 173, 1928.

[42] J. G. Simmons, *J. Appl. Phys.,* vol. 34, no. 9, pp. 2581-2590, 1963.

[43] W. Wang, T. Lee and M. A. Reed, *Phys. Rev. B,* vol. 68, p. 035416, 2003.

[44] F. So, Organic Electronics, Boca Raton: CRC Press, Taylor & Francis Group, 2010.

[45] C. W. Tang and S. A. Van Slyke, *Appl. Phys. Lett.,* vol. 51, p. 913, 1987.

[46] G. Horowitz, *Adv. Mater.,* vol. 10, p. 365, 1998.

[47] http://orgworld.de/.

[48] P. Stallinga, Electrical Characterization of Organic Electronic Materials and Devices, West Sussex: John Wiley & Sons Ltd., 2009.

[49] W. Brutting, Physics of Organic Semiconductors, Weinheim: Wiley-VCH Verlag Gmbh & Co., 2005.

[50] R. Waser, "Technology and Analysis," in *Nanoelectronics and Information Tehcnology, Advanced Electronics Materials and Novel Devices*, Weinheim, Wiley VCH Verlag & Co. KGaA, 3rd edition, 2012, p. 202.

[51] S. C. Tse, C. H. Cheung and S. K. So, "Charge Transport and Injection in Amorphous Organic Semiconductors," in *Organic Electronics*, Boca Raton, Taylor & Francis Group, 2010, p. 65.

[52] A. Kahn, N. Koch and W. Gao, *J. Polym. Sci. B: Polym. Phys. 41 (2003),* vol. 41, no. 21, pp. 2529–2548,, 2003.

[53] M. Gobbi, F. Golmar, R. Llopis, F. Casanova and L. E. Hueso, *Adv. Mat.,* vol. 23, pp. 1609-1613, 2011.

[54] J.-H. Lee, J. Lee , Y. H. Kim, C. Yun, B. Lüssem and K. Leo, *Organic Electronics,* vol. 15, p. 16–21, 2014.

[55] T. Menke, "PhD Thesis, Molecular Doping of Organic Semiconductors: A Conductivity and Seebeck Study," TU Dresden, Dresden, 2013.

[56] A. Hamed, Y. Y. Sun, Y. K. Tao, R. L. Meng and P. H. Hor, *Phys. Rev. B,* vol. 47, no. 16, p. 10873, 1993.

[57] S. Fujimori, K. Hoshimono, S. Fujita and S. Fujita, *Solid State Communications,* vol. 89, p. 437, 1994.

[58] G.-H. Kim, L. Shao, K. Zhang and K. P. Pipe, *Nature Mater.,* vol. 12, p. 719–723, 2013.

[59] M. Pfeiffer, K. Leo, X. Zhou, J. S. Huang, M. Hofmann, A. Werner and J. Blochwitz-Nimoth, *Organic Electronics,* vol. 4, pp. 89-103, 2003.

[60] A. Mityashin, Y. Olivier, T. Van Regemorter, C. Rolin, S. Verlaak, N. G. Martinelli, D. Beljonne, J. Cornil, J. Genoe and P. Heremans, *Adv. Mater.,* vol. 24, p. 1535–1539, 2012.

[61] S. Takebayashi, S. Abe, K. Saiki and K. Ueno, *Appl. Phys. Lett.,* vol. 94, p. 083305, 2009.

[62] D. Guo, S. Ikeda, K. Saiki, H. Miyazo and K. Terashima, *J. Appl. Phys.,* vol. 99, p. 094502, 2006.

[63] H. Ishii, N. Hayashi, E. Ito, Y. Washizu, K. Sugi, Y. Kimura, M. Niwano, O. Ouchi and K. Seki, "Kelvin Probe Study of Band Bending at Organic Semiconductor/Metal Interfaces: Examination of Fermi Level Alignment," in *Physics of Organic Semicondutors*, Weinheim, WILEY-VCH Verlag GMBH & Co., 2005, p. 71.

[64] A. P. Schulz, "PhD Thesis, "Interface Dipole Formation in Organic Surface Functionalizations: Tailoring Metal Contacts for Organic Optoelectronic Devices"," RWTH Aachen University, Aachen, 2012.

[65] H. Ishii, K. Sugiyama, E. Ito and K. Seki, *Adv. Mater. ,* vol. 11, no. 8, p. 605, 1999.

[66] Y. Gao, *Acc. Chem. Res.,* vol. 32, p. 247, 1999.

[67] S. T. Lee, Y. M. Wang, X. Y. Hou and C. W. Tang, *Appl. Phys. Lett.,* vol. 74, p. 670, 1999.

[68] C. S. Lee, J. X. Tang, Y. C. Zhou and S. T. Lee, *Appl. Phys. Lett.,* vol. 94, p. 113304, 2009.

[69] M. Knupfer and H. Peisert, *Phys. Stat. Sol. (a),* vol. 201, pp. 1055-1074, 2004.

[70] H. Vazquez, W. Gao, F. Flores and A. Kahn, *Phys. Rev. B,* vol. 71, p. 041306(R), 2005.

[71] N. F. Mott, *Proc. Cambridge. Philos. Soc. ,* vol. 34, p. 568, 1938.

[72] W. Schottky, *Phys. Z,* vol. 41, p. 570, 1940.

[73] L. P. Kouwenhove and P. L. McEuen, "Chapter 13: Single Electron Transport Through a Quantum Dot," in *Nanotechnology*, New York, Springer New York, 1999, pp. 471-535.

[74] D. V. Averin and K. K. Likharev, *J. Low Temp. Phys.,* vol. 62, no. 3-4, pp. 345-373, 1986.

[75] T. A. Fulton and G. J. Dolan, *Phys. Rev. Lett.,* vol. 59, no. 1, p. 109, 1987.

[76] L. L. Sohn, L. P. Kouwenhoven and G. Schoen, "Electron transport in quantum dots," in *Mesoscopic Electron Transport*, New York and London, Plenum , 1997.

[77] C. Fery, W. E. Bailey, K. Yamada and S. X. Wang, *Mat. Res. Soc. Symp. Proc.,* vol. 569, p. 185, 1999.

[78] E. A. Osorio, T. Bjornholm, J.-M. Lehn, M. Ruben and H. S. J. van der Zant, *J. Phys.:Condens. Matter,* vol. 20, p. 374121, 2008.

[79] A. Hirohata and K. Takanashi, *J. Phys. D: Appl. Phys.,* vol. 47, p. 193001, 2014.

[80] R. P. Feynman, R. B. Leighton and M. Sands, "Vol. 3," in *The Feynman Lectures on Physics*, Reading, MA, Addison-Wesley, 1965, pp. 3-4.

[81] S. Bandyopadhyay and M. Cahay, Introduction to Spintronics, Boca Raton, FL: CRC Press, Taylor and Francis Group, 2008.

[82] C. Cohen-Tannoudji, B. Diu and F. Lalo"e, "vols. 1 and 2," in *Quantum Mechanics*, John Wiley & Sons, 2006.

[83] S. Blundell, Magnetism in Condensed Matter, New York: Oxford University Press, 2001.

[84] E. C. Stoner, *Proc. Roy. Soc. London A,* vol. 165, no. 922, p. 372, 1938.

[85] S. Takahashi and S. Maekawa, *J. Phys. Soc. Jpn.,* vol. 77, no. 3, 2008.

[86] N. F. Mott, *Proc. Phys. Soc, Series A,* vol. 153, no. 880, pp. 699-717, 1936.

[87] M. N. Baibich , J. M. Broto , A. Fert , F. N. Van Dau , F. Petroff, P. Etienne, G. Creuzet, A. Friederich and J. Chazelas , *Phys. Rev. Lett.,* vol. 61, no. 2472, 1988.

[88] G. Binash, Grunberg P, F. Saurenbach and W. Zinn, *Phys.Rev.B,* no. 394828,, 1989.

[89] W. Thomson, *Proc. R. Soc. Lond. 1856-1857 ,* vol. 8, pp. 546-550, 1856.

[90] N. J., "Magnetoresistance Overview," Hewlett-Packard Company, 1995.

[91] S. Teruya and Y. Hidefumi, *J. Phys. Soc. Jpn.,* vol. 959, pp. 3061-3064, 1990.

[92] J. Moodera, L. R. Kinder, T. M. Wong and R. Meservey, *Phys. Rev. Lett.,* vol. 74, pp. 3273-3276, 1995.

[93] T. Miyazaki and N. Tezuka , *J. Magn. Mater.,* vol. 139, pp. L231-L234, 1995.

[94] J. Akerman, *Science,* vol. 308, p. 508, 2005.

[95] W. H. Butler, X.-G. Zhang, T. C. Schulthess and J. M. MacLaren, *Phys. Rev. B: Cond. Matter Mat. Phys.,* vol. 63, p. 054416, 2001.

[96] S. Ikeda, J. Hayakawa, Y. Ashizawa, Y. M. Lee, K. Miura, H. Hasegawa, M. Tsunoda, F. Matsukura and H. Ohno, *Appl. Phs. Lett. ,* vol. 93, p. 082508, 2008.

[97] M. Johnson and R. H. Silsbee, *Phys. Rev. Lett.,* vol. 55, no. 17, pp. 1790-1793, 1985.

[98] D. Sun, E. Ehrenfreund and Z. V. Vardeny, *Chem. Commun. ,* vol. 50, p. 1781, 201.

[99] M. Erekhinsky, F. Casanova, I. K. Schuller and A. Sharoni, *Appl. Phys. Lett.,* vol. 100, p. 212401, 2012.

[100] I. Appelbaum, B. Huang and D. J. Monsma, *Nature,* vol. 44, pp. 295-298, 2007.

[101] S. O. Valenzuela, *Int. J. Mod. Phys. B, 23, 2413 (2009),* vol. 23, no. 11, pp. 2413-2438, 2009.

[102] I. Zutic, J. Fabian and S. Das Sarma, *Rev. Mod. Phys.,* vol. 76, no. 2, pp. 323-410, 2004.

[103] Y. Yafet, *Phys. Rev. ,* vol. 85, p. 478, 1952.

[104] R. J. Elliot, *Phys. Rev. ,* vol. 96, p. 266, 1954.

[105] E. Y. Tsymbal and I. Zutic, Handbook of Spin Transport and Mangetism, Boca Raton: CRC Press, Taylor & Francis Group, 2012.

[106] J. Fabian and S. Das Sarma, *J. Vac. Sci. Technol. B,* vol. 17, p. 1708, 1999.

[107] T. Sasaki, Y. Ando, M. Kameno, T. Tahara, H. Koike, T. Oikawa, T. Suzuki and M. Shiraishi, *Phys. Rev. Applied,* vol. 2, p. 034005, 2014.

[108] Y. Ji, A. Hoffmann, J. S. Jiang, J. E. Pearson and S. D. Bader, *J. Phys. D: Appl. Phys.,* vol. 40, pp. 1280-1284, 2007.

[109] T. Valet and A. Fert, *Phys. Rev. B,* vol. 48, p. 7099, 1993.

[110] I. Rashba, *Phys. Rev. B,* vol. 62, p. 267, 2000.

[111] Y. Cao, M. L. Steigerwald, C. Nuckolls and X. Guo, *Adv. Mater.,* vol. 22, pp. 20-32, 2010.

[112] M. Rothschild, M. W. Horn, C. L. Keast, R. Kunz, L. Vladimir, S. C. Palmateer, S. P. Doran, A. R. Forte, R. B. Goodman, J. H. Sedlacek, R. S. Uttaro, D. Corliss and A. Grenville, *The Lincoln Laboratory Journal,* vol. 10, no. 1, 1997.

[113] E. L. Wolf, Nanophysics and Nanotechnology, An Introduction to Modern Concepts in Nanoscience, Weinheim: Wiley VCH Verlag GmbH & Co. KGaA, 2004.

[114] V. Bakshi, EUV Sources for Lithography, Washington: SPIE Press, Bellingham, 2006.

[115] A. K. Raub, A. Frauenglass, S. R. J. Brueck, W. Conley, R. Dammel, A. Romano, M. Sato and W. Hinsberg, *J.Vac.Sci.Technol. B,* vol. 22, p. 3459, 2004.

[116] M. A. Mohammad, M. Muhammad, S. K. Dew and M. Stepanova, "Chapter 2: Fundamentals of Electron Beam Exposure and Dvelopment," in *Nanofabrication*, Springer Vienna, 2012, pp. 11-41.

[117] N. Arjmandi, L. Lagae and G. Borg, *J. Vac. Sci. Technol. B,* vol. 27, p. 1915, 2009.

[118] S. Yasin, D. G. Hasko and H. Ahmeda, *Appl. Phys. Lett.,* vol. 78, no. 18, pp. 2760-2762, 2001.

[119] P. Rai-Choudhury, Handbook of microlithography, micromachining and microfabrication, volume 1: microlithography, Society of Photo-Optical Instrumentation Engineers, 1997.

[120] "http://www.cnf.cornell.edu/cnf_spie3.htm".

[121] B. Cord, J. Yang, H. Duan, D. C. Joy, J. Klingfus and K. K. Berggren, *J. Vac. Sci. Technol. B,* vol. 27, no. 6, Nov/Dec 2009.

[122] D. F. Kyser and N. S. Viswanathan, *J. Vac. Sci. Technol.,* vol. 12, no. 6, pp. 1305-1308, 1975.

[123] M. J. Rooks, E. Kratschmer, R. Viswanathan, J. Katine, R. E. Fontana, Jr. and S. A. MacDonald, *J. Vac. Sci. Technol. B,* vol. 20,,, no. 6, pp. 2937-2941, 2002.

[124] M. S. a. S. Dew, "Chapter 2," in *Nanofabrication, Techniques and Principles*, NewYork, SpringerWienNewYork, p. 13.

[125] S. Alborghetti, P. Stamenov, G. Fois and J. M. D. Coey, *ISRN Nanotechnology,* vol. 2012, no. 253246, 2012.

[126] L. Ren and B. Chen, "Proximity effect in electron beam lithography," in *Solid-State and Integrated Circuits Technology*, 2004.

[127] T. H. P. Chang, *Journal of Vacuum Science & Technology,* vol. 12, p. 1271, 1975.

[128] M. Parikh, *J. Vac. Sci. Technol.,* vol. 15, no. 3, pp. 931-933, 1978.

[129] H. Eisenmann, T. Waas and H. Hartmann, *J. Vac. Sci. Technol. B,* vol. 11, no. 6, pp. 2741-2745, 1993.

[130] K. Cummings, R. Frye and E. Rietman, *Appl. Phys. Lett.,* vol. 57, pp. 1431-1433, 1990.

[131] G. Owen and P. Rissman, *J. Appl. Phys.,* vol. 54, no. 6, pp. 3573-3581, 1983.

[132] M. C. Rosamond, J. T. Batley, G. Burnell, B. J. Hickey and E. H. Linfield, *Microelecton. Eng.,* vol. 143, p. 5, 2015.

[133] http://nanolithography.gatech.edu/proximity.htm.

[134] W. Hu, "PhD Thesis, "Ultrahigh Resolution Electron Beam Lithography"," Hu, W., Notre Dame, Indiana, 2004.

[135] R. G. Mortimer, "Some Additional Theories of Nonequilibrium Processes," in *Physical Chemistry*, Academic Press, 2nd edition, 2000, p. 956.

[136] M. Yan, S. Choi, K. R. V. Subramanian and I. Ades, *J. Vac. Sci. Technol. B,* vol. 26, no. 6, pp. 2306-2310, 2008.

[137] J.-S. Wi, H.-S. Lee and K.-B. Kim, *Electronic Materials Letters,* vol. 3, no. 1, pp. 1-5, 2007.

[138] nanolithography.gatech.edu/proximity.htm.

[139] Q. Hang, D. A. Hill and G. H. Bernstein, *J. Vac. Sci. Technol. B,* vol. 21, pp. 91-97, 2003.

[140] A. N. Broers, *IBM J. Res. Develop.,* vol. 32, no. 4, pp. 502-513, 1988.

[141] Y. Sun , X. Chen and N. Dai, *Journal of Semiconductors,* vol. 29, no. 9, pp. 1666-1669, 2008.

[142] L. Arzubiaga, F. Golmar, R. Llopis, F. Casanova and L. E. Hueso, *Appl. Phys. Lett.,* vol. 102, p. 193103, 2013.

[143] J. Park, A. N. Pasupathy, J. I. Goldsmith, C. Chang, Y. Yaish, J. R. Petta, M. Rinkoski, J. P. Sethna, H. D. Abrunas, P. L. McEuen and D. C. Ralph, *Nature,* vol. 47, pp. 722-725, 2002.

[144] A. S. Zyazin, J. W. G. van den Berg, E. A. Osorio, H. S. J. van der Zant, N. P. Konstandinidis, M. Leijnse, M. R. Wegewijs, F. May, W. Hofstetter, C. Danieli and A. Cornia, *Nano Lett.,* vol. 10, pp. 3307-3311, 2010.

[145] K. Yoshida, I. Hamada, S. Sakata, A. Umeno, M. Tsukada and K. Hirakawa, *Nano Lett.,* vol. 13, pp. 481-485, 2013.

[146] J. J. Henderson, C. M. Ramsey, E. del Barco, A. Mishra and G. Christou, *J. Appl. Phys.,* vol. 101, p. 09E102.

[147] L. Arzubiaga, F. Golmar, R. Llopis, F. Casanova and L. E. Hueso, *AIP Advances,* vol. 4, no. 117126, 2014.

[148] K. I. Bolotin, F. Kuemmeth, A. N. Pasupathy and D. C. Ralph, *Nano Lett.,* vol. 6 (1), p. 123–127, 2006.

[149] D. Young and A. Christou, *IEEE Transactions on Reliability,* vol. 43, no. NO. 2, pp. 186-192, 1994.

[150] J. R. Black, *Proceedings of the IEEE,* vol. 57, no. NO. 9, 1969.

[151] J. R. Black, *IEEE Transactions on Electronic Devices,* Vols. ED-16, no. 4, pp. 338-347, 1969.

[152] Q. Huang, C. M. Lilley and R. Divan, *Nanotechnology,* vol. 20, no. 075706, 2009.

[153] wsadd.

[154] M. L. Trouwborst, S. J. van der Molen and B. J. van Wees, *J. Appl. Phys.,* vol. 99, p. 114316, 2006.

[155] C. Pennetta, E. Alfinito, L. Reggiani, F. Fantini, I. DeMunari and A. Scorzoni, *Phys. Rev. B,* vol. 70, no. 174305, 19 November 2004.

[156] K. Iniewski, Nanoelectronics, Nanowires, Molecular Electronics and Nanodevices, McGraw-Hill, 2011.

[157] H. Park, A. K. L. Lim, A. P. Alivisatos, J. Park and P. L. McEuena, "Appl. Phys. Lett.," vol. 75, no. 2, pp. 301-303, 1999.

[158] J. Park, "PhD Thesis: Electron Transport in Single Molecule Transistors," University of California, Berkeley, 2003.

[159] A. N. Pasupathy, "Electron Transport in Molecular Transistors," Cornell University , Berkeley, California, 2004.

[160] K. O'Neill, E. A. Osorio and H. S. J. van der Zant, *Appl. Phys. Lett.,* vol. 90, no. 133109, 2007.

[161] A. S. Stepanov, E. S. Soldatov and O. V. Snigirev, *J. Supercond. Nov. Magn.,* vol. 24, p. 1087–1093, 2011.

[162] J. C. Doan, S. Lee, S. H. Lee, P. A. Flinn, J. C. Bravman and T. N. Marieb, *J. Appl. Phys.,* vol. 89, no. 12, pp. 7797-7808, 2001.

[163] N. Agrait, A. L. Yeyati and J. M. van Ruitenbeek, *Physics Reports,* vol. 377, pp. 81-279, 2003.

[164] C. R. Wolf, "PhD Thesis: Contacting Quantum Dots with nano-electrodes," Ulm University, Ulm, Germany, 2010.

[165] J. Tang, Y. Wang, C. Nuckolls and S. J. Wind, *J. Vac. Sci. Tenchol. B,* vol. 24, no. 6, pp. 3227-3229, 2006.

[166] A. Fursina, S. Lee, R. G. S. Sofin, I. V. Shvets and D. Natelson, *Appl. Phys. Lett.,* vol. 92, p. 113102, 2008.

[167] J. Tang, E. P. De Poortere, J. E. Klare, C. Nuckolls and S. J. Wind, *Microelectronic Engineering ,* vol. 83, pp. 1706-1709, 2006.

[168] J. Tang, Y. Wang, J. E. Klare, G. S. Tulevski, S. J. Wind and C. Nuckolls, *Angew. Chem. Int. Ed.,* vol. 46, pp. 892-3895, 2007.

[169] F. Prins, M. Monrabal-Capilla, E. A. Osorio, E. Coronado and H. S. J. van der Zant, *Adv. Mater,* vol. 23, no. 13, pp. 1545-1549, 2011.

[170] D. J. Young and M. Cohen, *J. Electrochem. Soc.,* vol. 124, p. 769, 1977.

[171] A. Bachtold, P. Hadley, T. Nakanishi and C. Dekker, *SCIENCE ,* vol. 294, pp. 1317-1320, 2011.

[172] T. Campell, R. K. Kalia, A. Nakano, P. Vashishta, S. Ogata and S. Rodgers, *Phys. Rev. Lett.,* vol. 82, no. 24, pp. 4866-4869, 1999.

[173] B. Feng, J. Weng, B. C. Yang, J. Y. Cheng, J. Z. Zhao, L. He, S. K. Qi and X. D. Zhang, *Materials Characterization ,* vol. 49, p. 129–137, 2003.

[174] D. O. Albina, "PhD Thesis, "Theory and Experience on Corrosion of Waterwall and Superheated Tubes of Waste-to-Energy Facilities"," Columbia University, New York, 2005.

[175] A. E. Vladár and M. T. Postek, *Microscopy and Microanalysis,* vol. 11, p. 764, 2005.

[176] S. Kayashima, K. Takahashi , M. Motoyama and J. Shirakashi, *Jpn. J. Appl. Phys.,* vol. 46, no. 37, p. L907–L909, 2007.

[177] C. W. Miller and D. D. Belyea, *J. Appl. Phys.,* vol. 105, p. 094505, 2009.

[178] C. W. Miller, Z. Li, J. Akerman and I. Schuller, *Appl. Phys. Lett.,* vol. 90, p. 043513, 2007.

[179] C. W. Miller, Z. Li, I. Schuller, R. W. Dave, J. M. Slaughter and J. Akerman, *Phys. Rev. B,* vol. 74, p. 212404, 2006.

[180] M. Gobbi, "PhD Thesis, "Spintronic devices based on fullerence C60"," Universidad del Pais Vasco, San Sebastian, 2013.

[181] K. Instruments, "Section 3," in *Low Level Measurements Handbook*, KEITHLEY, 6th Edition.

[182] R. Manual and R. B. June, Model 6220 DC Current Source Model 6221 AC and DC Current Source User's Manual, Cleveland, Ohio: Keithly Instruments, Inc., 2005.

[183] A. Sommerfeld and H. Bethe, in *Handbuch der Physik*, Berlin, Julius Springer-Verlag, 1933, p. 450.

[184] R. Holm, *J. Appl. Phys.,* vol. 22, no. 5, p. 569, 1951.

[185] J. Bardeen, *Phys. Rev. Lett. ,* vol. 6, p. 57, 1961.

[186] W. Harrison, *Phys. Rev.,* vol. 123, p. 85, 1961.

[187] R. Stratton, *J. Phys. Chem. Solids,* vol. 23, p. 1177, 1962.

[188] W. F. Brinkman, R. C. Dynes and J. M. Rowell, *J. Appl. Phys.,* vol. 41, p. 1915, 1970.

[189] P. Steinmann and J. M. R. Weaver, *Appl. Phys. Lett.,* vol. 86, p. 063104, 2005.

[190] V. R. Manfrinato, L. Zhang, D. Su, H. Duan, R. G. Hobbs, E. A. Stach and K. K. Berggren, *Nano Lett.,* vol. 13, pp. 1555-1558, 2013.

[191] M. S. Saifullah, T. Ondarcuhu, D. K. Koltsov, C. Joachim and M. E. Welland, *Nanotechnology 13,* vol. 13, pp. 659-662, 2002.

[192] T. Li, W. Hu and D. Zhu, *Adv. Mater.,* vol. 22, pp. 286-030, 2010.

[193] P. R. Bevington and D. K. Robinson, Data Reduction and Error Analysis for the Physical Sciences, New York: McGraw-Hill, 2003.

[194] J. J. Akerman, J. M. Slaughter, R. W. Dave and I. K. Schuller, *Appl. Phys. Lett.,* vol. 79, p. 3104, 2001.

[195] W. Langheinrich and H. Ahmed, *Jpn. J. Appl. Phys.,* vol. 34, pp. 6956-6960, 1995.

[196] U. Rudiger, R. Calarco, U. May, K. Samm, J. Hauch, H. Kittur and G. Guntherodt, *J. Appl. Phys.,* vol. 89, no. 11, p. 7573, 2001.

[197] J. M. Rowell, in *Tunneling Phenomena in Solids*, E. Burnstein and S. Lundqvuist, Eds., New York, Plenum Press, 1969, pp. 385-404.

[198] J. J. Akerman, R. Escudero, C. Leighton, S. Kim, D. A. Rabson, R. W. Dave, J. M. Slaughter and I. K. Schuller, *J. Magn. Magn. Mater.,* vol. 240, p. 86, 2002.

[199] T. Nazwa, U. Hashim and T. S. Dhahi, *IFMBE Proceedings,* vol. 35, pp. 388-392, 2011.

[200] F. Cverna, Thermal Properties of Metals, Materials Park, Ohio: ASM International, 2002.

[201] Z. A. K. Durrani, Single-Eletron Devices and Circuits in Silicon, London: Imperial College Press, 2010.

[202] D. V. Averin and A. N. Korotkov, *J. Low Temp. Phys.,* vol. 80, p. 173, 1990.

[203] J. von Delft and D. C. Ralph , *Physics Reports,* vol. 345, pp. 61-173, 2001.

[204] L. Arzubiaga, "PhD Thesis, Nanostructuring of Devices for Nanoscience Applications," Universidad del Pais Vasco, San Sebastian, 2015.

[205] F. Kuemmeth, K. I. Bolotin, S. Shi and D. C. Ralph, *Nano Lett.,* vol. 8, no. 12, pp. 4506-4512, 2008.

[206] D. L. Klein, R. Roth, A. P. Alivisatos and P. L. McEuena, *Nature,* vol. 389, p. 699, 1997.

[207] D. K. Ferry, S. M. Goodnick and J. Bird, in *Transport in Nanostructures*, New York, Cambridge University Press, 2009.

[208] Y. V. Nazarov and Y. M. Blanter, Quantum Transport: Introduction to Nanoscience, Cambridge University Press, 2009, p. 228.

[209] L. P. Kouwenhoven, L. L. Sohn, L. P. Kouwenhoven and G. Schoen, "Transport Electron transport in quantum dots," in *Mesoscopic Electron*, New York and London, Plenum, 1997, pp. 105-214.

[210] Y. Takahashi, M. Naease, H. Namatsu, K. Kurihara, K. Iwdate, Y. Nakajima, S. Horiguchi, K. Murase and M. Yabe, *Electronic Letters,* vol. 31, no. 2, p. 136, 1995.

[211] S. J. Shin, J. J. Lee, H. J. Kang, J. B. Choi, S.-R. E. Yang, Y. Takahashi and D. G. Hasko, *Nano Lett. ,* vol. 11, pp. 1591-1597, 2011.

[212] D. R. Ward, G. D. Scott, Z. K. Keane, N. J. Halas and D. Natelson, *J. Phys.: Condens. Matter,* vol. 20, p. 374118, 2008.

[213] S. J. Kim, C. K. Lee, J. U. Lee, S. J. Choi, J. H. Hwang, S. E. Lee, J. B. Choi, K. S. Park, W. H. Lee, I. B. Paik and J. S. Kang, *J. Semicond. Technol. Science,* vol. 6, no. 1, p. 52, 2006.

[214] S. S. Datta, D. R. Strachan and A. T. C. Johnson, *Phys. Rev. B,* vol. 79, p. 205404, 2009.

[215] B. Gao, E. A. Osorio, K. Babaei Gaven and H. S. J. van de Zant, *Nanotechnology,* vol. 20, p. 415207, 2009.

[216] H. B. Heersche, Z. de Groot, J. A. Folk, L. P. Kouwenhoven, H. S. J. van der Zant, A. A. Houck, J. Labaziewicz and I. L. Chuang, *Phys. Rev. Lett.,* vol. 96, p. 017205, 2006.

[217] M. E. Gershenson, V. Podzorov and A. F. Morpungo, *Rev. Mod. Phys.,* vol. 78, p. 973, 2006.

[218] B. A. Mattis, Y. Pei and V. Subramanian, *Appl. Phys. Lett.,* vol. 86, p. 033133, 2005.

[219] H. S. Majumdar, J. K. Baral, R. Osterbacka, O. Ikkala and H. Stubb, *Organic Electronics,* vol. 6, pp. 188-192, 2005.

[220] T. Tsai, J. Chang, C. Wang, M. Lin, T. Guo, T. Wen, J. Chang and C. Wu, *Organic Electronics,* vol. 15, no. 8, p. 1759–1766, 2014.

[221] K. Horiuchi, S. Uchino, S. Hashii, A. Hashimoto, T. Kato, T. Sasaki, N. Aoki and Y. Ochiai, *Appl. Phys. Lett.,* vol. 85, no. 11, pp. 1987-1989, 2004.

[222] V. Nádaždy, R. Durný, J. Puigdollers, C. Voz, S. Cheylan and K. Gmucová, *Appl. Phys. Lett. ,* vol. 90, p. 092112, 2007.

[223] Y. Yamashita, J. Tsurumi, F. Hinkel, Y. Okada, J. Soeda, W. Zajaczkowski, M. Baumgarten, W. Pisula, H. Matsui, K. Mullen and J. Takeya, *Adv. Mater.,* vol. 26, no. 48, p. 8169–8173, 2014.

[224] X. Sun, M. Gobbi, A. Bedoya-Pinto, O. Txoperena, F. Golmar, R. Llopis, A. Chuvilin, F. Casanova and L. E. Hueso, *Nat. Comm.,* vol. 4, p. 2794, 2013.

[225] F. Golmar, M. Gobbi, R. Llopis, P. Stoliar, F. Casanova and L. E. Hueso, *Organic Electronics ,* vol. 13, pp. 2301-2306, 2012.

[226] D. R. Lide , CRC Handbook of Chemistry and Physics, Internet Version 2005, Boca Raton, FL: CRC Press, 2005.

[227] J. Hwang, A. Wan and A. Khan, *Materials Science and Engineering R 64,* vol. 64, pp. 1-31, 2009.

[228] G. N. Derry and Z. Ji-Zhong, *Phys. Rev. B,* vol. 39, no. 3, p. 1940, 1989.

[229] N. E. Singh-Miller and N. Marzari, *Phys. Rev. B,* vol. 80, p. 235407, 2009.

[230] M. Kitamura and Y. Arakawa, *J. Phys.: Condens. Matter,* vol. 20, p. 184011, 2008.

[231] S. Kobayashi, T. Takenobu, S. Mori, A. Fujiwara and Y. Iwasa, *Appl. Phys. Lett.,* vol. 82, no. 25, pp. 4581-4583, 2003.

[232] G.-C. Liang and W. Ghosh, *Phys. Rev. Lett.,* vol. 95, p. 076403, 2005.

[233] Y. Matsuoka, N. Inami, E. Shikoh and A. Fujiwara, *Sci. Technol. Adv. Mater.,* vol. 6, pp. 427-430, 2005.

[234] "Personal Communication with Dr. Nestor Ghenzi," 2015.

[235] R. Xie, G. W. Bryant, J. Zhao, V. H. Smith, A. Di Carlo and A. Pecchia, *Phys. Rev. Lett.,* vol. 90, no. 20, p. 206602, 2003.

[236] X. Zheng, W. Lu, T. A. Abtew, V. Meunier and J. Bernholc, *ACSNANO,* vol. 4, no. 12, pp. 7205-7210, 2010.

[237] A. Nigam, G. Schwabegger, M. Ullah, R. Ahmed and I. I. Fishchuk, *Appl. Phys. Lett. ,* vol. 101, p. 083305, 2012.

[238] C. Li, B. Wang, Y. Yao, G. Piao, L. Gu, Y. Wang, X. Duan and R. Yu, *Nanoscale,* vol. 6, p. 6585, 2014.

[239] K. Asaka, R. Kato, Y. Maezono, R. Yoshizaki, K. Miyazawa and T. Kizuka, *Appl. Phys. Lett.,* vol. 88, p. 051914, 2006.

[240] R. M. Abdullah, A. J. Vick, B. A. Murphy and H. Atsufumi, *J. Phys. D: Appl. Phys.,* vol. 47, p. 482001, 2014.

[241] T. Kimura, J. Hamrle, Y. Otani, K. Tsukagoshi and Y. Aoyagi, *Appl Phys. Lett.,* vol. 85, no. 22, p. 5382, 2004.

[242] F. A. Zwanenburg, D. W. van der Mast, H. B. Heersche, L. P. Kouwenhoven and E. P. A. M. Bakkers, *Nano Lett.,* vol. 9, no. 7, pp. 2704-2709, 2009.

[243] F. J. Jedema, M. S. Nijboer, A. T. Filip and B. J. van Wees, *Phys. Rev. B,* vol. 67, p. 085319, 2003.

[244] A. Bid, A. Bora and A. K. Raychaudhuri, *Phys. Rev. B,* vol. 74, p. 035426, 2006.

[245] A. E. White, M. Tinkham, W. J. Skocpol and D. C. Flanders, *Phys. Rev. Lett.,* vol. 48, no. 25, pp. 1752-1754, 1982.

[246] J. M. Ziman, Electrons and Phonons, Clarendon, Oxford: Oxford University Press, 1960.

[247] M. Isasa, E. Villamor, L. Fallarino, A. Suszka, C. Tollan, A. Berger, L. E. Hueso and F. Casanova, *J. Phys. D: Appl. Phys.,* vol. 48, p. 215003, 2015.

[248] L. O'Brien, M. J. Erickson, D. Spivak, H. Ambaye, R. J. Goyette, V. Lauter, P. A. Crowell and C. Leighton, *Nat. Comm.,* vol. 5, p. 3927, 2013.

[249] Y. Ji, A. Hoffman, J. E. Pearson and S. D. Bader, *Appl. Phys. Lett.,* vol. 88, p. 052509, 2006.

[250] T. Wakamura, K. Ohnishi, Y. Niimi and Y. Otani, *App. Phys. Express,* vol. 4, p. 063002, 2011.

[251] Y. Fukuma, L. Wang, H. Idzuchi, S. Takahashi, S. Maekawa and Y. Otani, *Nat. Mater.,* vol. 10, p. 527, 2011.

[252] Y. Fukuma, L. Wang, H. Idzuchi and Y. Otani, *Appl. Phys. Lett,* vol. 97, p. 012507, 2010.

[253] L. Gan, R. D. Gomez, A. Castillo, P. J. Chen, C. J. Powell and W. F. Egelhoff, *Thin Solid Films ,* vol. 415, pp. 219-223, 2009.

[254] H. Boeve, J. De Boeck and G. Borghs, *J. Appl. Phys.,* vol. 89, p. 482, 2001.

[255] T. Yang, T. Kimura and Y. Otani, *Nature ,* vol. 4, pp. 851-854, 2008.

[256] P. Laczkowski, L. Vila, S. Ferry, A. Marty, J.-M. George, H. Jaffres, A. Fert, T. Kimura, T. Yang, Y. Otani and J.-P. Attane, *Appl. Phys. Express ,* vol. 4, no. 6, p. 063007, 2011.

[257] H. B. Heersche, G. Lientschnig, K. O'Neill, H. S. J. van der Zan and H. W. Zandbergen, *Appl. Phys. Lett.,* vol. 91, p. 072107 , 2007.

[258] P. J. de Pablo, A. Asenjo, J. Colchero, P. A. Serena, J. Gomez-Herrero and A. M. Baro, *Surf. Interface Anal.,* vol. 30, pp. 278-282, 2000.

[259] G. A. Sullivan, *J. Phys. Chem. Solids Pergamon Press ,* vol. 28, pp. 347-350, 1967.

[260] F. Casanova, A. Sharoni, M. Erekhinsky and I. K. Schuller, *PRB,* vol. 79, no. 184415, 2009.

[261] S. Steenwyk , S. Hsu, . R. Loloee, . J. Bass and W. P. Pratt, *Journal of Magnetism and Magnetic Materials,* vol. 170, no. L1 L6, 1997.

[262] S. Dubois , L. Piraux, J. M. George, K. Ounadjela, J. L. Duvail and A. Fert, *PHYSICAL REVIEW B,* vol. 60, no. 1, p. 477, 1999.

[263] T. Maasen, I. J. Vera-Marun, M. H. D. Guimarães and B. J. van Wees, *Phys. Rev. B ,* vol. 86, p. 235408, 2012.

[264] H. Idzuchi, Y. Fukuma, S. Takahashi, S. Maekawa and Y. Otani, *Phys. Rev. B ,* vol. 89, p. 081308(R), 2014.

[265] M. Wojtaszek, I. J. Vera-Marun and B. J. van Wees, *Phys. Rev. B ,* vol. 89, p. 245427 , 2014.

[266] W. Zhang, S. H. Brongersma, Z. Li, D. Li, O. Richard and K. Maex, *J. Appl. Phys.,* vol. 101, p. 063703, 2007.

[267] J. Bass and W. P. Pratt Jr, *J. Phys.: Condens. Matter,* vol. 19, p. 183201, 2007.

[268] N. W. Ashcroft and N. D. Mermin, Solid State Physics, Orlando, FL: Saunders, 1976.

[269] D. J. Monsma and S. S. Parkin, *Appl. Phys. Lett. ,* vol. 77, no. 5, pp. 720-722, 2000.

[270] D. Beckmann, H. B. Weber and H. von Lohneysen, *Phys. Rev. Lett.,* vol. 93, p. 197003, 2004.

[271] G. Zahnd, L. Vila, T. V. Pham, A. Marty, P. Laczkowski, W. Savero Torres, C. Vergnaud, M. Jamet, J.-P. Attané, C. Vergnaud, M. Jamet and J.-P. Attané, *arXiv:1507.00858,* 2015.

Acknowledgements:

First off, I would like to thank my supervisor Luis Hueso, and my fellow group members. I believe my time in the nanodevices group has enabled me to gain a broad perspective on what is truly needed to do research and for that, I am really grateful. Experimental research is quite expensive and often requires excessive amounts of working hours. For this reason I would like to express my gratitude to the Marie Curie Actions for funding the work in a way I believe makes research a more attractive career.

Experimental research is a multifaceted process, which requires a team effort. In this respect I would like to thank all the people who helped by discussing problems, and proposing experiments to assist this work. Felix, Pablo, Xiangnan, Fede and others offered very valuable advice in times of need and have had an inspiring attitude towards research which I believed has influenced my own stance.

Invaluable support was also offered by the technical team both for fabrication and measurements. Roger Llopis, Ralph Gay and Gorka Pazos, without you this work would be truly impossible.

I would like to thank Libe for sharing both the frustration and excitement of our endeavor into nanotechnology. I feel that working with Libe was a privilege and I am sad that our time as colleagues has ended.

Similarly, I would like to thank Luca for sharing almost everything the past four years were about for me. From dealing with being in a new country, to pondering about philosophy and trying to understand physics, Luca has made my four years here better, and I am really happy that we shared this experience.

Last but not least, given the recurrent stress dealt with as a PhD candidate, I would like to thank my friends and family who kept me sane during the process. My parents, my sister and my friends were always supportive and often helped me forget about the frustration brought on by research. Thales, Anastasia, Estitxu, Angelique, the Italians (there’s so many of you :D), Amilcar, Marco, the lilianos, Jon, Oihana, Isa, the Zinemalderos, the basket-pote ballers, the (friki) board gamers, the weird band we had going for some time and many others have enriched my life in many ways and although we will probably end up living in different countries I will cherish our time together.

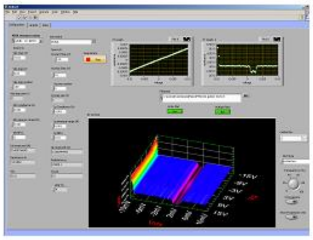
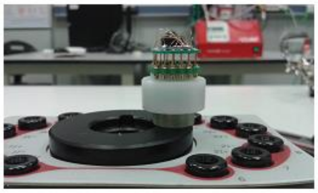


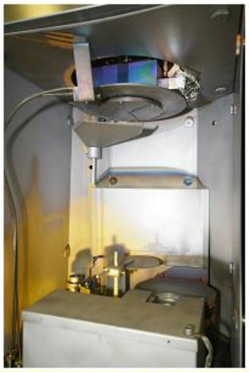


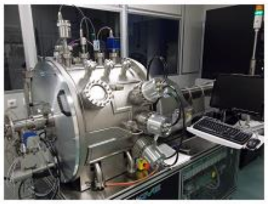

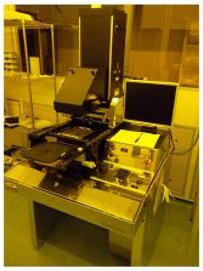


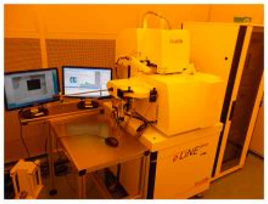

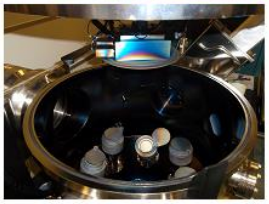


USER BRIDGE

UNIVEX